A SANS Study of the Interfacial Curvatures and the Phase Behavior in Bicontinuous Microemulsions

by

Sung-Min Choi

M.S. in Nuclear Engineering, M.I.T., 1996
M.S. in Nuclear Engineering, Seoul National University, 1990
B.S. in Nuclear Engineering, Seoul National University, 1988

Submitted to the Department of Nuclear Engineering
in partial fulfilment of the requirements for the degree of

Doctor of Philosophy in Applied Radiation Physics

at the

MASSACHUSETTS INSTITUTE OF TECHNOLOGY

September 1998

Author ....
Department of Nucelar Engineering
August 17, 1998

Certified by .. ..
Sow-Hsin Chen
Professor
Thesis Supervisor

Certified by ....
Xiao-Lin Zhou
Assistant Professor
Thesis Reader

Accepted by ....
Lawrence M. Lidsky
Chairman, Department Committee on Graduate Students

A SANS Study of the Interfacial Curvatures and the Phase Behavior in Bicontinuous Microemulsions

by

Sung-Min Choi

Submitted to the Department of Nuclear Engineering
on August 17, 1998, in partial fulfillment of the
requirements for the degree of
Doctor of Philosophy in Applied Radiation Physics

Abstract

A microemulsion is a three-component system in which oil and water are solubilized via an interfacial surfactant monolayer. Depending on the composition and various external conditions, it exhibits a wide variety of phases with corresponding mesoscopic scale interfacial structures. For scientific as well as industrial purposes, knowledge of the relation between the interfacial structure and the phase behavior is crucial but its quantitative measure is lacking. To identify the relation in a quantitative way, the natural parameters to be measured are the interfacial curvatures : Gaussian, mean, and square mean curvatures. A new small-angle neutron scattering (SANS) data analysis method to extract the interfacial curvatures was developed and applied to various microemulsions. The method involves the use of a clipped random wave model with an inverse 8th order polynomial spectral function. The spectral density function contains three basic length scales : the inter-domain distance, the coherence length, and the surface roughness parameter. These three length scales are essential to describe mesoscopic scale interfaces. A series of SANS experiments were performed at various phase points of isometric and non-isometric microemulsions. Using the developed model, the three interfacial curvatures at each phase point were determined for the first time in a practical way. In isometric bicontinuous microemulsions, the Gaussian curvature is negative and has a parabolic dependence on the surfactant volume fraction. In non-isometric systems, based on the measured interfacial curvatures, a characteristic structural transformation was identified. As the water and oil volume ratio moves away from unity, the bicontinuous structure transforms to a spherical structure through an intermediate cylindrical structure.

Thesis Supervisor: Sow-Hsin Chen
Title: Professor

Acknowledgments

All my years at MIT until today have benefited from many people. I would like to first thank Sow-Hsin Chen for supervising my research. Without his fatherly guidance and warm encouragement, any part of this thesis would have not been possible. I also am grateful to David G. Cory for his support in many aspects of my research. First three years of my research with him at MIT was very enjoyable and stimulating. I also wish to thank Sidney Yip for his thoughtful advice when I most needed it and to Xiao-Lin Zhou for reading through the rough draft of this thesis. I also thank Richard Lanza, Gordon L. Brownell, and Mujid S. Kazimi for participating in my thesis defense committee.

I also wish to thank Charles J. Glinka, John Barker and Steve Kleine at NIST Pappannan Thiyagarajan, Jamie Ku, and Denis G. Wozniak at ANL, J. S. Lin and George Wignall at ORNL, and Dieter K. Schneider and Vito Graziano at BNL, for allowing me to use their beam lines and their assistance during my experiments.

I have been fortunate to meet many friends at MIT. The time I have spent with Namsung Ahn, Sangman Kwak, Changhee Jang, Richard Choi, John Chun, Changwoo Kang, Jonggoo Kim, Sewon Park, Caroline Shin, Yongkyoon In, Peter Sprenger, Yuan Cheng, Wurong Zhang, Ciya Liao, Daniel Lee and Yingchun Liu, have made my life at MIT enjoyable and will never be forgotten. I would like to thank Dawen Choy for his help during the final correction of this thesis.

I am very grateful to my fiance Myoyong for her love and support which have made my last year at MIT full of joy and happiness.

I am deeply grateful to my mother, my sister, Sunghee, and my brothers, Sungsoo and Sungyoo. Without their unconditional love, encouragement, and patience, I would have not been able to accomplish any of my work. Finally, I would like to express my deep gratitude to my father who had never hesitated to provide any necessities for my studies. I hope he can see my humble achievement even in heaven.

My study at MIT was supported by a Korean Oversea Study Scholarship and by a grant from Materials Science Division of US Department of Energy.

Contents

List of Figures

List of Tables

Chapter 1

Introduction

For thousands of years, humans have benefited from the unique surface activity of amphiphilic molecules called surfactants. In addition to traditional applications, recently surfactants have been playing prominent roles in emerging new technologies such as nano-fabrication, microelectronics, and pharmaceutical agents. Due to the extraordinary physics they exhibit as well as their expanding number of applications, surfactants have attracted the attention of a broad spectrum of the scientific community.

The achievements made during the last few decades have been remarkable [1, 2, 3, 4, 5, 6]. Full understanding of the beauty of the underlying physics, however, still requires extensive investigation. One particularly interesting aspect of physics is the relation between the structure and the phase behavior of three component surfactant systems called microemulsions[7]. To identify the relation in a quantitative way, we developed a new method of SANS data analysis and applied it in the study of various microemulsions. In this introduction, the basic concepts of surfactants physics are reviewed.

1.1 Amphiphilic Nature of Surfactants

Surfactants are substances with molecular structures consisting of a hydrophilic part which is soluble in water and a hydrophobic part which is soluble in oil. The hydrophobic part is normally a hydrocarbon chain, whereas the hydrophilic part consists of either an ionic or strongly polar group. The simple *amphiphilic nature* of surfactants towards water and oil leads to phenomena which mixtures of simple solute molecules, water, and oil do not exhibit[8]. At the phase boundaries, an orientating alignment of the surfactant molecules occurs, placing their hydrophilic part in water and the hydrophobic part in oil. This results in a change of system properties such as a dramatic decrease in interfacial tension between water and the adjacent phases, a change of wetting properties, as well as the formation of electrical double layers at the interfaces. The self-associated aggregates can exist in a variety of topological structures.

Since surfactants are primarily applied in aqueous solutions, they are classified into two categories, ionic and non-ionic, by the type of hydrophilic group present. Ionic surfactants have hydrophilic groups which, in aqueous solution, dissociate into a negatively charged ion (anion) and a positively charged ion (cation). When the surface active properties is carried by anion, the surfactant is called an anionic surfactant and when by cation, it is called a cationic surfactant. On the other hand, non-ionic surfactants do not dissociate into ions and instead its head group makes a hydrogen bond with water. The solubility of non-ionic surfactants in water is provided by polar groups such as polyglycol ether groups or polyol groups. Figure 1-1 shows an ionic surfactant, bis (2-ethylhexyl) sulfosuccinate sodium salt, called AOT, and a non-ionic surfactant, tetraethylene glycol monodecyl ether, called $C_{10}E_4$. In a schematic convention, it is customary to call the hydrophilic part the head group and the hydrophobic part the tail group.

The amphipilicity of surfactants can be tuned by various external conditions such as temperature, salinity, and pressure[8, 1]. Depending on the relative strength of affinity toward water and oil, as well as composition, surfactants spontaneously aggregate into various topologically different structures. Figure 1-2 shows the representative structures of microemulsions for different relative hydrophilic and hydrophobic strength of surfactants. For simplicity, the ratio of the hydrophilic strength to the hydrophobic strength, R, is defined in a qualitative sense.

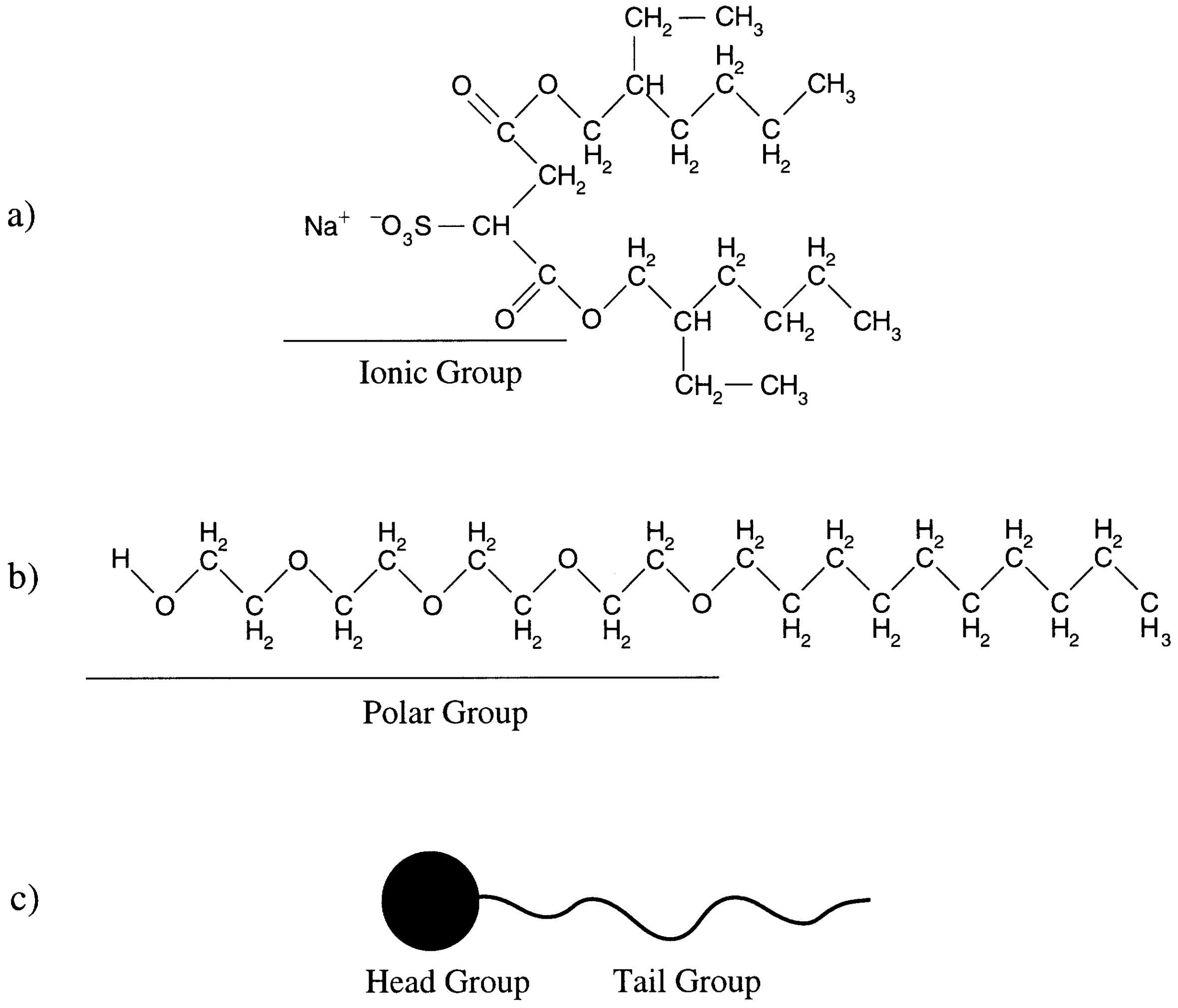

Figure 1-1: Surfactant molecules. a) ionic surfactant AOT, b) non-ionic surfactant $C_{10}E_4$ and c) schematic diagram of a surfactant molecule

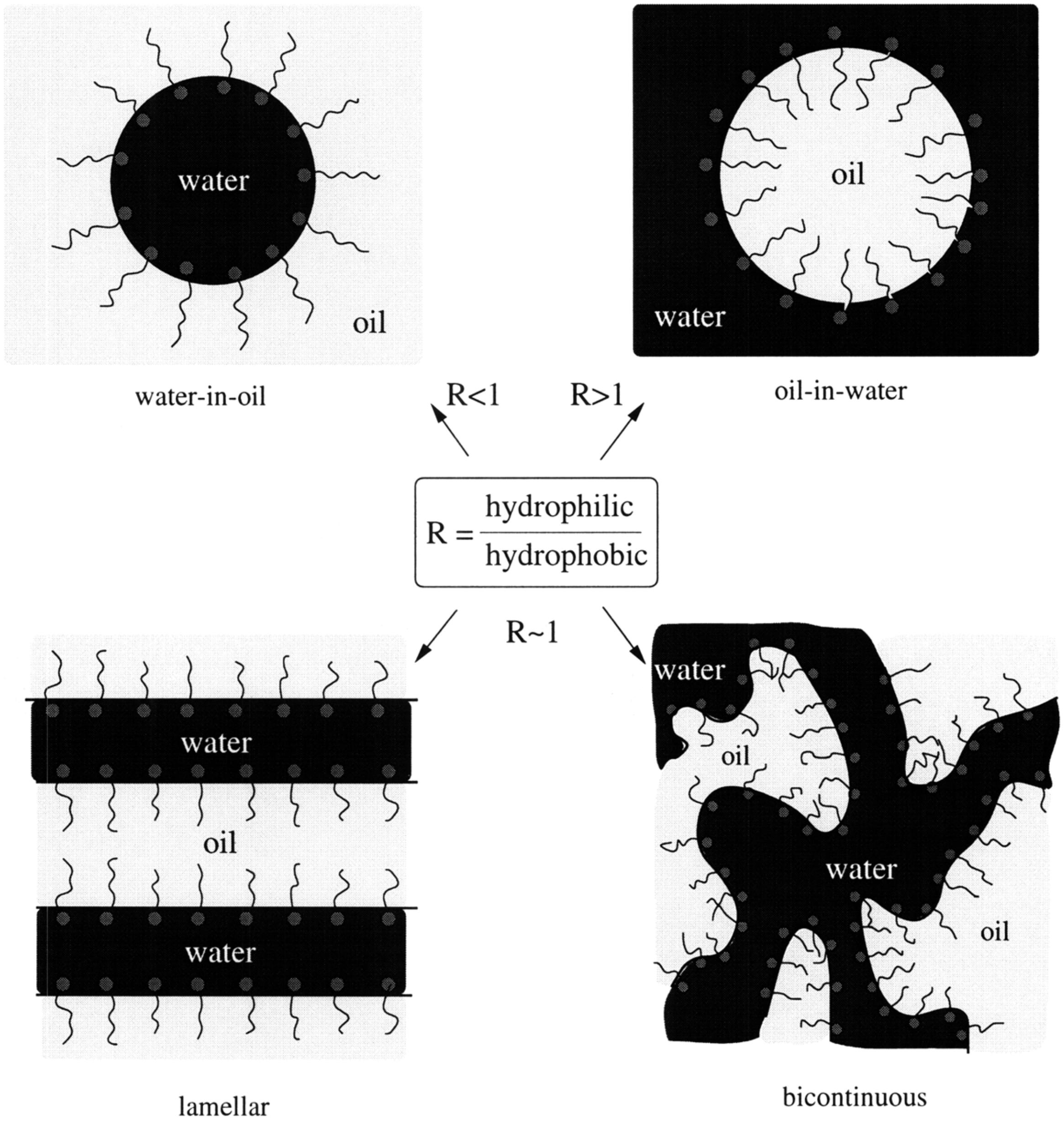

Figure 1-2: Relation between the hydrophilicity/hydrophobicity and microemulsion structure

When R is less than one, surfactants are more soluble in oil and place themselves in such a way that the surfactant-oil interface has maximum area. The interfacial membrane, therefore bends toward water, resulting in water-in-oil microemulsions or reverse micelles. When R is larger than one, the situation is reversed and the amphiphilic region bends toward oil, giving oil-in-water microemulsions or direct micelles.[9] According to Winsor[10], however, R is not a fixed value for a given system but undergoes fluctuations due to the thermal motion of the molecules. Therefore, the micellar structure fluctuates between the direct and reverse form and the predominant form depends on the mean value of R. Thus, when R is balanced near unity at a given temperature, it may be tipped in either direction by small changes in temperature or composition.

When $R = 1$, the hydrophile and lipophile tendencies of the surfactant are equilibrated. This case corresponds especially to systems where equal volumes of oil and water are solubilized. For such a system, two main types of structures can be considered : lamellar and bicontinuous. The lamellar structure is formed by more or less regular arrangement of the surfactant molecules in the form of parallel leaflets allowing alternate solubilization of oil and water. These lamellar structures are somewhat rigid and often result in liquid crystals or gels. On the other hand, the bicontinuous structure, which was first proposed by Scriven[11, 12], exhibits more complex disordered surfactant interfaces. In this structure, water and oil domains are interpenetrating through each other. Furthermore the water is connected as a single domain and the same applies oil. If one follows the interface, at some point the surfactant membrane closes up to encapsulate the water, and at another point it closes up to encapsulate the oil.

1.2 Phase Behavior of Microemulsions

The phase behavior of a ternary system of H_2O-oil-surfactant is determined by the interplay of the miscibility gaps of the binary systems, water-oil : water-surfactant, and oil-surfactant [13, 14, 15]. To understand the phase behavior of the ternary system, it is thus necessary to consider the phase diagram of the three binary systems which represent the sides of the Gibbs phase prism. Figure 1-3 shows the unfolded phase triangle with schematic diagrams of the three binary phases. The phase diagram of each binary system is presented with the Gibbs triangle as base and temperature as ordinate. The base represents the composition of each binary system. The hatched area represents the 2 phase region where the mixture is immiscible, and the rest is the 1 phase region where a solution is formed.

Since water and oil are almost insoluble in each other, their miscibility gap in the water-oil phase diagram extends into the Gibbs triangle. The critical point of the miscibility gap lies well above the boiling point of the mixture. The phase diagram of an oil-surfactant system shows similar behavior to the water-oil system, but with a much lower critical point which lies close to the melting point of the mixture. Its critical temperature depends on the chemical nature of both the oil and the surfactant.

The phase diagram of the water-surfactant system, however, shows a rather complicated feature. It consists of two separate miscibility gaps. The lower miscibility gap lies, in general, below the melting point of the mixture. The existence of the upper miscibility gap can be explained as follows. Hydrogen bond formation between water and surfactant molecules leads to complete miscibility between these two components at ambient temperatures. As the temperature increases, however, these hydrogen bonds break due to thermal fluctuations and the miscibility gap appears again. For thermodynamic reasons, the upper miscibility gap shows a closed loop[16].

The lower part of Figure 1-3 shows a schematic Gibbs triangle which represents the phase behavior of a water-oil-surfactant system at an ambient temperature. As the concentration of surfactant increases, the mutual solubility of water and oil increases and therefore the miscibility gap shrinks until the two phases merge at the isothermal critical point, called a plait point. The compositions within the 2 phase region are connected by tie lines, the slopes of which are determined by the distribution coefficient of the surfactant between water and oil. The positive slope corresponds to higher solubility of surfactant in oil than in water, and vice versa.

The Gibbs phase triangle can be determined as a function of temperature. Fig-

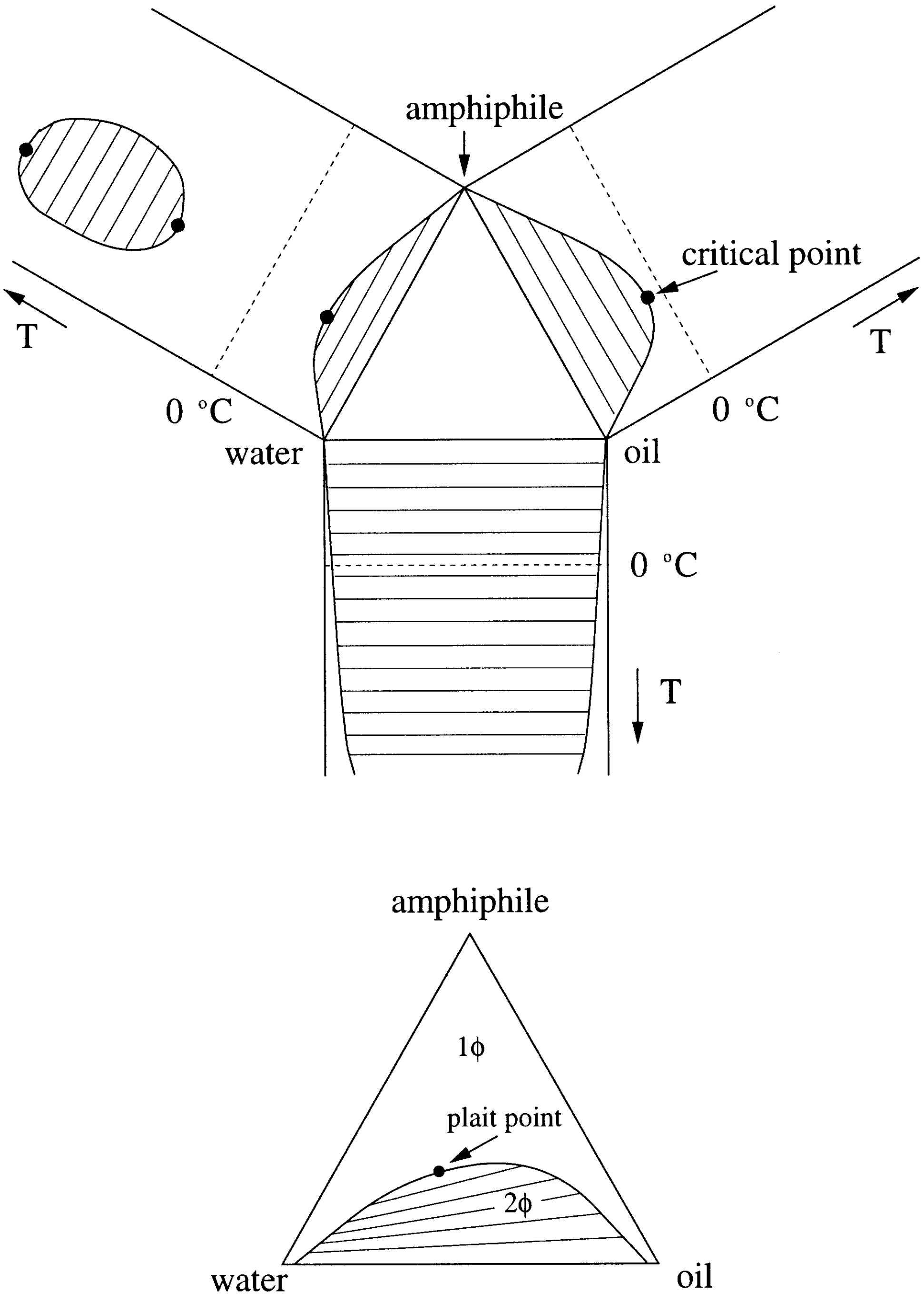

Figure 1-3: Phase diagrams of the three binary systems and the Gibbs phase triangle

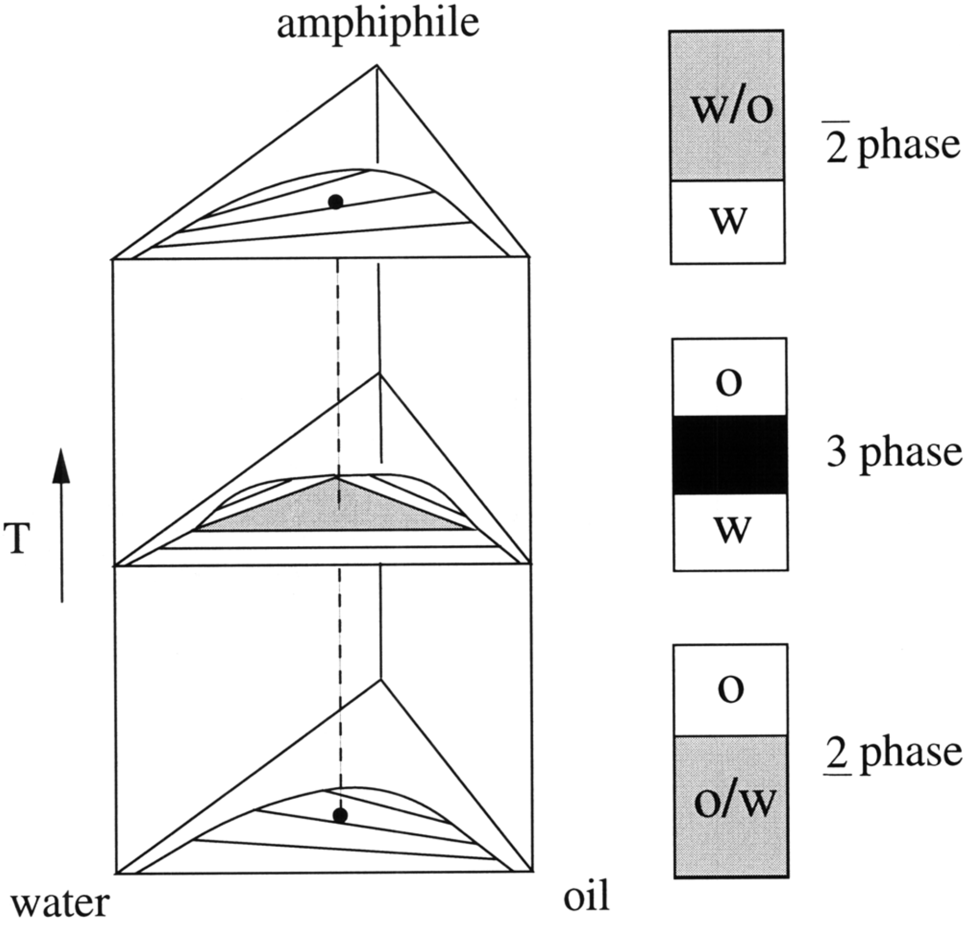

Figure 1-4: Gibbs phase prism of a ternary system

ure 1-4 shows a Gibbs phase prism of a water-oil-nonionic surfactant system. As the temperature rises, the surfactant is transfered from the water-rich to the oil-rich phase. At low temperatures, the hydrophilic strength of the head group is stronger than the hydrophobic strength of the tail group. Therefore, the surfactant is dissolved mainly in the water-rich phase, resulting in a two phase equilibrium between a lower microemulsion phase and an excess upper oil phase. The lower microemulsion phase can be described as a oil-in-water microemulsion in which oil droplets surrounded by surfactants are dispersed within the major water medium.

As the temperature increases, the imbalance between the hydrophilic and hydrophobic strengths of the surfactant is reduced. When the HLB (hydrophilic and lipophilic balanced) temperature is reached, the hydrophilic and hydrophobic strengths of the surfactant becomes equal and a 3 phase area, the shaded area in the center, shows up in the Gibbs triangle. The solution will separate into three phases : an excess oil layer on top, an excess water layer on the bottom and a microemulsion layer in the middle, called a middle phase microemulsion. The 3 phase triangle exists within a limited temperature range only. It will appear at a temperature close to the lower critical temperature of the binary miscibility gap between water and surfactant, and will disappear at a temperature close to the upper critical temperature of the binary miscibility gap between oil and surfactant. Within this temperature range it will change its position as well as its shape, depending on the effect of temperature on the shapes of the three miscibility gaps in the binary systems. Therefore, the 3 phase body is characterized by its position on the temperature scale as well as by its extension within the phase diagram.

The middle phase microemulsions, called *bicontinuous microemulsions* [11], have sponge-like structures, in which the oil and water micro-domains are multiply interconnected. Since they have a minimum interfacial tension of about 10^{-4}mN/m and minimum solubilization power, bicontinuous microemulsions are frequently discussed in the literature[17, 18, 19, 20, 21]. Minimum interfacial tension is always observed when the bicontinuous microemulsion takes up equal volume fractions of water and oil. In contrast to the micellar or well-ordered phases, the geometry of bicontinuous microemulsions cannot be described in simple geometrical terms. The main focus of this research is to identify its structure in a quantitative way.

When the temperature is higher than the HLB point, the hydrophilic strength of the head group becomes weaker than the hydrophobic strength of the tail group due to thermal fluctuation which breaks the hydrogen bonding. Compared to the low temperature case, the situation is reversed and surfactant is dissolved mainly in the oil-rich phase, resulting in a two phase equilibrium between an upper water-in-oil microemulsion phase and a lower excess water phase.

Representing the phase behavior in a multi-dimensional diagram is often complicated, especially when the number of components or the tuning parameters are large. Therefore it is convenient to project the phase diagram onto a certain plane, keeping other parameters constant. A useful and widely adopted phase plane is given in Figure 1-5, which shows a vertical cut through the phase prism erected on the center line of the base, that is, on the line in the Gibbs triangle where the water-oil ratio is unity. Since the volumes of water and oil is equal on this plane, microemulsions represented by this plane are called *isometric* . If looked at from the oil edge of the prism, one can see the profile of the phase boundaries as having the shape of a fish. This phase diagram also reveals the upper and lower boundary temperatures of the 3 phase body. The head of the fish represents the minimum surfactant concentration needed to form aggregate structures and the fish tail, where all the phase boundaries collapse into a single point, reveals the minimum surfactant concentration needed to prepare a homogeneous solution (1 phase) of equal volume of water and oil.

Figure 1-6 shows another commonly used phase plane. In this plane, while the surfactant concentration is kept constant, the water to oil volume ratio is varied. Therefore, microemulsions whose phase behaviors are represented on this plane are called *non-isometric.*

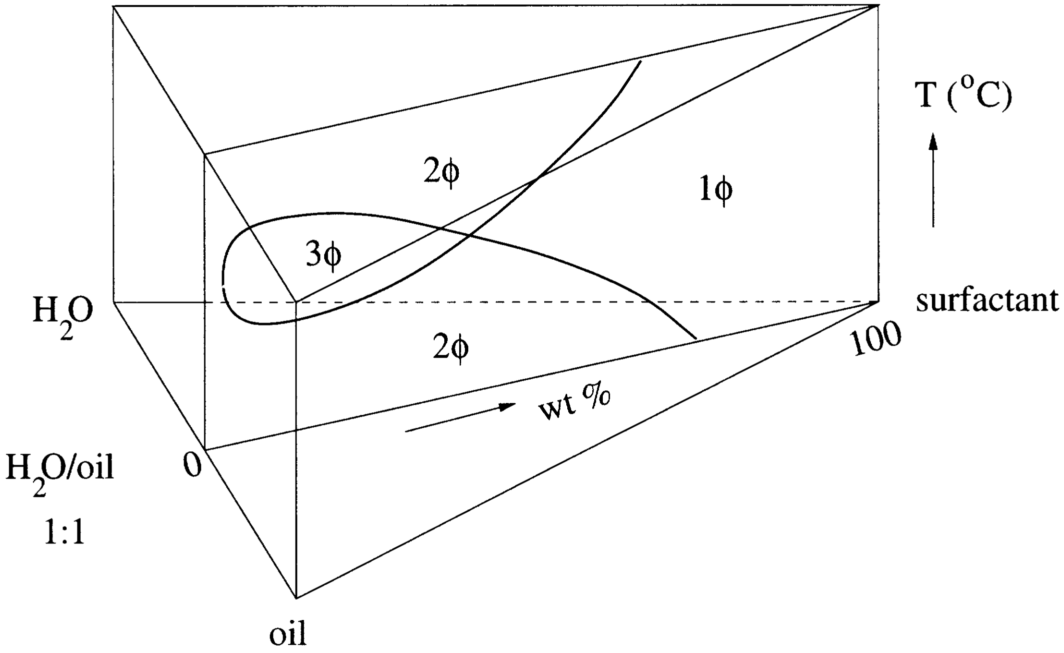

Figure 1-5: Phase diagram of isometric H_2O/oil/surfactant : a vertical section through the Gibbs phase prism at H_2O/oil =1/1

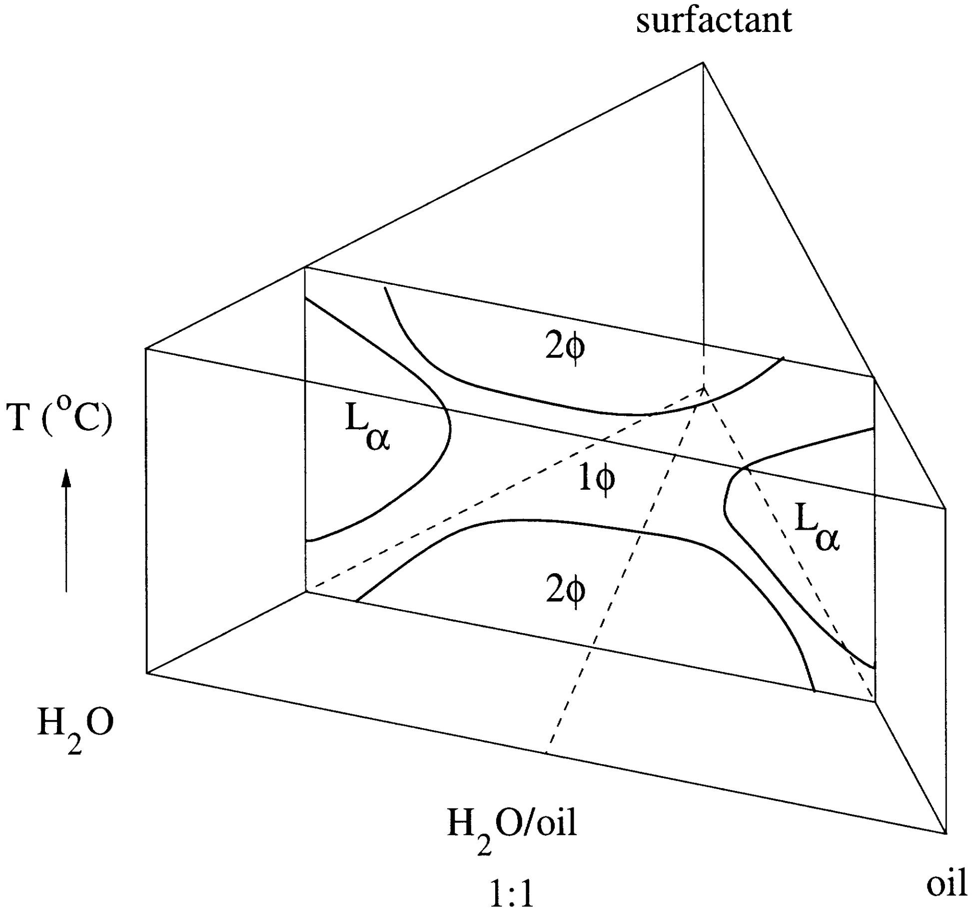

Figure 1-6: Phase diagram of non-isometric H_2O/oil/surfactant : a vertical section through the Gibbs phase prism at a constant surfactant concentration.

Chapter 2

Small-Angle Neutron Scattering

A physical description of surfactant solutions requires knowledge of the structures of surfactant aggregates and the forces which act on them. Structural information can be obtained only from experiments which measure distances on a scale comparable with the dimensions of the aggregates. Today, the most promising way to measure distance in liquids is to use radiation that can penetrate the sample and study its interference patterns[22, 23, 24, 25, 26, 27]. Neutron and X-rays have been the primary sources for these scattering experiments. Since the characteristic lengths in surfactant solutions lie in the mesoscopic scale range (on the order of 100 Å) and the wavelength of cold neutrons used is a few Å, useful structural information is contained in the small angle region of neutron or x-ray scattering. Therefore, in this study, we used small-angle neutron scattering techniques.

The neutron was discovered by Chadwick in 1932. It has zero charge, a mass of 1.0087 atomic mass unit, a spin of 1/2 and a magnetic moment of -1.9132 nuclear magnetons[28]. It has a half life of 894 seconds and decays into a proton, an electron and an anti-neutrino. Due to its useful characteristic wavelength, strong penetration power, and weak interactions with medium of interest, the neutron has been used extensively as a probe in condensed matter physics. The theory of neutron scattering is well known[28, 29]. In this section, the basic principles of neutron scattering and its application to the study of microemulsion systems are briefly reviewed.

2.1 Coherent and Incoherent Scattering

We first consider scattering by a single atom. A schematic diagram of the neutron scattering experiment is shown in Figure 2-1. A neutron with wave vector $\vec{k}_{in}$ is directed to the target and scattered into a state with wave vector $\vec{k}_{out}$. The momentum transfer to the target sample is $\hbar\vec{Q}$ where the momentum transfer vector $\vec{Q}$ is defined as

$$\vec{Q} = \vec{k}_{in} - \vec{k}_{out}. \tag{2.1}$$

The basic quantity that is measured is the partial differential cross-section which gives the fraction of neutrons of incident energy E scattered into an element of solid angle $d\Omega$ with an energy between E' and $E' + dE'$. The partial differential cross-section is denoted by

$$\frac{d^2\sigma}{d\Omega dE'} \tag{2.2}$$

and has the dimensions of (area/energy). For our purpose only elastic scattering, where there is no energy change, is considered. Integrating the partial differential cross section given in Eq. 2.2 over energy yields the differential cross section, defined as

$$\frac{d\sigma}{d\Omega} = \frac{\text{No. of neutrons scattered into a solid angle } d\Omega \text{ around } \vec{\Omega} \text{ per unit time}}{\text{incident neutron flux}}. \tag{2.3}$$

In elastic scattering, the scattered wave vector $\vec{k}_{out}$ has the same magnitude as the incident wave vector $\vec{k}_{in}$,

$$k = |\vec{k}_{in}| = |\vec{k}_{out}| = \frac{2\pi}{\lambda} \tag{2.4}$$

where λ is the wavelength of the neutron. Correspondingly, the magnitude of the momentum transfer vector $\vec{Q}$ given in Eq. 2.1 depends only upon the scattering angle θ,

$$|\vec{Q}| = 2k \sin\frac{\theta}{2}. \tag{2.5}$$

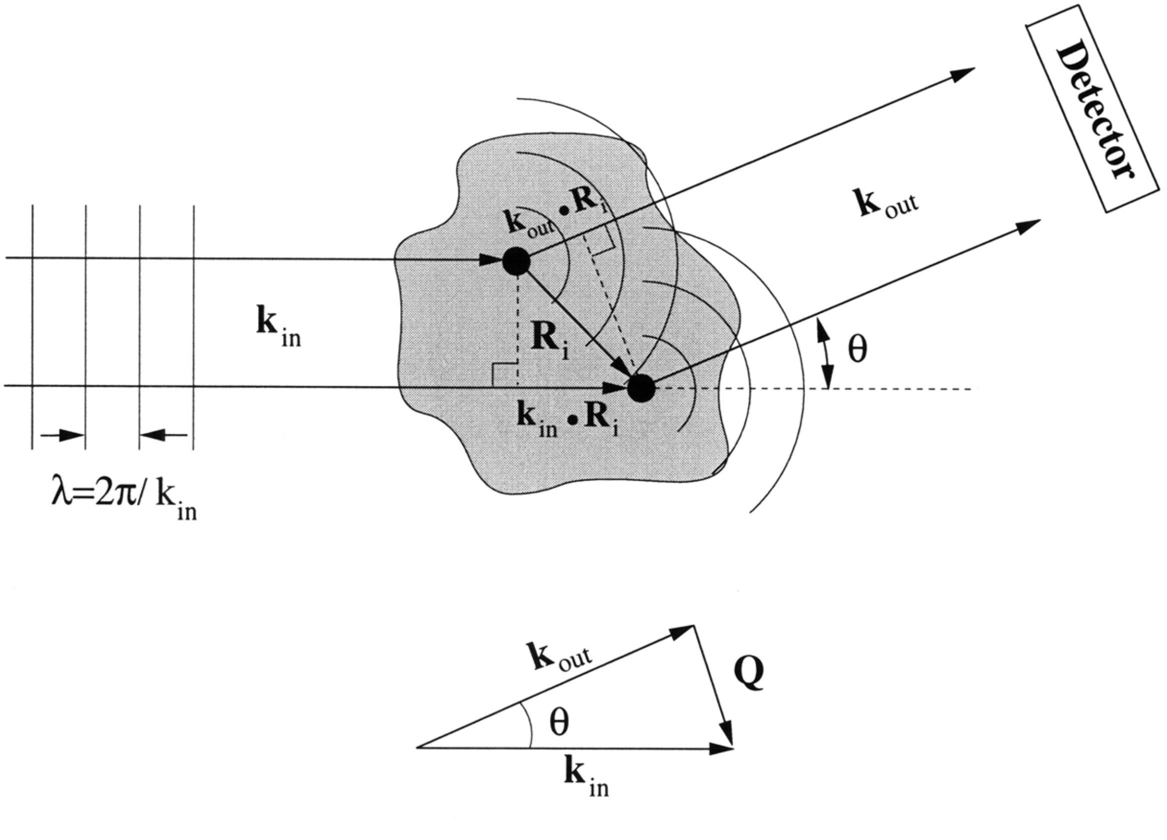

Figure 2-1: Schematic representation of a scattering experiment

The incident neutron beam can be described by a plane wave traveling in the $+\hat{z}$ direction,

$$\psi_{in}(\vec{r}) = e^{i(k_{in}z-\omega t)} \tag{2.6}$$

where $\vec{k}_{in} = k_{in}\hat{z}$ is the wave vector with magnitude given by $E = \hbar^2 k_{in}^2/2\mu = \hbar\omega$. When this wave hits an atom at the origin, a fraction of it will be scattered and the scattered wave radiates spherically around the scattering center,

$$\psi_{sc}^{0}(\vec{r}) = -\frac{b}{r}e^{i(kr-\omega t)} \tag{2.7}$$

where b is the scattering length of the atom which measures its strength of the interaction with neutrons. In general, the scattering length b depends not only on each atom type but also on each isotope and its spin. If the atom is not at the origin but at a position $\vec{R}_i$, the wave scattered in the direction $\vec{k}_{out}$ will be phase shifted with respect to the wave scattered in the same direction from the origin. This is well explained in Figure 2-1. The path difference results in a phase difference equal to $\vec{Q}\cdot\vec{R}_i$. Accordingly, the wave scattered by the atom at $\vec{R}_l$ is

$$\psi_{sc}^{l}(\vec{r}) = -b_l e^{i\vec{Q}\cdot\vec{R}_l}\frac{e^{i(kr-\omega t)}}{r}. \tag{2.8}$$

Summing up the relative phase contributions from all the atoms in the sample, the total scattered wave is calculated as

$$\psi_{sc}(\vec{r}) = f\left(\vec{Q}\right)\frac{e^{i(kr-\omega t)}}{r} \tag{2.9}$$

where the scattering amplitude $f\left(\vec{Q}\right)$ is defined as

$$f\left(\vec{Q}\right) = -\sum_l b_l e^{i\vec{Q}\cdot\vec{R}_l}. \tag{2.10}$$

Since radiation detectors are not sensitive to the phase of the incoming radiation, they measure the power flux instead of the amplitude. According to the definition given in Eq. 2.3, the differential cross section can be calculated as the square of the magnitude of the scattering amplitude,

$$\begin{aligned}\frac{d\sigma}{d\Omega} &= \left|f\left(\vec{Q}\right)\right|^2 \\ &= \left|\sum_l b_l e^{i\vec{Q}\cdot\vec{R}_l}\right|^2 \\ &= \sum_{ll'} b_l b_{l'} e^{i\vec{Q}\cdot(\vec{R}_l-\vec{R}_{l'})}.\end{aligned} \tag{2.11}$$

Since what we measure during experiments is the ensemble average of the system, the differential cross section should be also ensemble averaged,

$$\frac{d\sigma}{d\Omega} = \left\langle \sum_{ll'} \overline{b_l b_{l'}} e^{i\vec{Q}\cdot(\vec{R}_l-\vec{R}_{l'})} \right\rangle \tag{2.12}$$

where the bar denotes both isotope and spin-orientation averages and $\langle\cdot\cdot\rangle$ is a thermal average over all the possible configurations consistent with a given temperature T.

The differential cross section can be distinguished into two types of scattering processes known as coherent and incoherent scattering. Without going into detail, it is clear that the interference pattern can be generated only from the terms where $l \neq l'$. Performing the average over isotope and spin-orientation, $\overline{b_l b_{l'}}$ can be written as,

$$\overline{b_l b_{l'}} = \left|\bar{b}\right|^2 + \delta_{l,l'}\left(\overline{|b|^2} - \left|\bar{b}\right|^2\right). \tag{2.13}$$

Substituting Eq. 2.13 into Eq. 2.12, the cross section becomes the sum of two parts,

$$\frac{d\sigma}{d\Omega} = \left(\frac{d\sigma}{d\Omega}\right)_{coh} + \left(\frac{d\sigma}{d\Omega}\right)_{incoh} \tag{2.14}$$

where the coherent cross section is

$$\left(\frac{d\sigma}{d\Omega}\right)_{coh} = \left\langle \left|\bar{b}\right|^2 \left|\sum_l e^{\left(i\vec{Q}\cdot\vec{R}_l\right)}\right|^2 \right\rangle \tag{2.15}$$

and the incoherent cross section is

$$\left(\frac{d\sigma}{d\Omega}\right)_{incoh} = N\left(\overline{|b|^2} - \left|\overline{b}\right|^2\right) \tag{2.16}$$

where N is the total number of atoms in the target. In coherent scattering there is strong interference between waves scattered from each nucleus. On the other hand, in incoherent scattering there is no interference at all, and the cross-section is completely isotropic. Since structural information is contained only in the coherent scattering cross-section, the incoherent scattering part of the scattering intensity is often removed before further analysis. For our purpose, we only consider coherent scattering and, if not specified, scattering refers to coherent elastic scattering and the subscript is dropped.

2.2 Absolute Scattering Intensity

For aggregates of small particles, macromolecules in liquid solution, the scattering pattern produced can be divided into small-angle scattering and wide-angle scattering. Wide-angle scattering corresponds to the distance $\vec{R}_l - \vec{R}_{l'}$ between neighboring atoms (1 to 5 Å). In liquids, there are very many such distances, which all fluctuate and overlap each other. Their interference pattern reduces to a superposition of overlapping diffuse rings. Therefore, in the range of scattering vectors $Q = 2\pi/d =$ 1.2 to 6 $Å^{-1}$, scattering does not yield much useful information.

Small-angle scattering is produced by mesoscopic or large length scale (10 to 1000 Å) heterogeneities in the solution[30, 31] and covers the range of scattering vector Q $\approx=$ 0.005 to 0.6 $Å^{-1}$. At this range, the solution can be treated as a continuous medium, and scattering is controlled by the density of scattering length which is defined as

$$\rho\left(\vec{R}\right) = \sum_l \overline{b}_l \delta\left(\vec{R} - \vec{R}_l\right), \tag{2.17}$$

where $\overline{b}_l$ is the coherent scattering length of the particle at $\vec{R}_l$. The scattering amplitude is then the Fourier transform of the scattering length density in the irradiated volume V,

$$f\left(\vec{Q}\right) = \int \rho\left(\vec{R}\right) e^{-\vec{Q}\cdot\vec{R}} d\vec{R}. \tag{2.18}$$

Inserting Eq. 2.18 into Eq. 2.12 and taking the thermal average, the scattering cross-section per unit volume, $I(\vec{Q})$, can be written as

$$I\left(\vec{Q}\right) = \frac{1}{V}\left\langle\left|\int \rho\left(\vec{R}\right) e^{-\vec{Q}\cdot\vec{R}} d\vec{R}\right|^2\right\rangle. \tag{2.19}$$

$I(\vec{Q})$ is also called the absolute scattering intensity. Considering the translational invariance of the system, the absolute intensity can be reduced to a Fourier transform of a correlation function for the scattering length density at the origin and $\vec{r}$,

$$I\left(\vec{Q}\right) = \int \Gamma\left(\vec{r}\right) e^{-\vec{Q}\cdot\vec{r}} d\vec{r} \tag{2.20}$$

where the correlation function $\Gamma\left(\vec{r}\right)$ is defined as

$$\Gamma\left(\vec{r}\right) = \left\langle \rho^*\left(0\right) \rho\left(\vec{r}\right)\right\rangle. \tag{2.21}$$

If the sample is isotropic, the correlation function and the absolute intensity do not depend on the orientation of $\vec{r}$ or $\vec{Q}$ and therefore, the angular variables can be integrated out. In this case, they are related by the one-dimensional Fourier transform,

$$I\left(Q\right) = \int_0^\infty \Gamma\left(r\right) \frac{\sin\left(Qr\right)}{Qr} 4\pi r^2 dr. \tag{2.22}$$

It can be shown that the average scattering length density contributes only to the delta function at $Q = 0$, and the interference patterns are produced only by the fluctuation of scattering length density. Therefore, it is appropriate to define a quantity in which the average scattering density is subtracted. A local fluctuation $\eta\left(r\right)$ is defined as

$$\eta\left(r\right) = \rho\left(r\right) - \overline{\rho} \tag{2.23}$$

where $\overline{\rho}$ is the scattering length density averaged over the whole sample. Using the definition given in Eq. 2.23 and the apparent condition $\langle \eta(r) \rangle = 0$, the absolute intensity $I(Q)$, except at $Q = 0$, can be written as follows

$$I(Q) = \left\langle \eta^2 \right\rangle \int_0^\infty \Gamma_D(r) \frac{\sin(Qr)}{Qr} 4\pi r^2 dr \tag{2.24}$$

where $\Gamma_D(r)$ is defined as

$$\Gamma_D(r) = \frac{\langle \eta(0) \eta(r) \rangle}{\langle \eta^2 \rangle}. \tag{2.25}$$

In the study of porous materials, the function $\Gamma_D(r)$ is commonly called the Debye correlation function[32]. There are two physical boundary conditions which the Debye correlation must satisfy : it is normalized to unity at the origin and should converge to zero at infinity. The mean square fluctuation of local scattering length density $\langle \eta^2 \rangle$ is called *the invariant.* For two component porous systems, it is given as

$$\left\langle \eta^2 \right\rangle = \phi_1 \phi_2 (\rho_1 - \rho_2)^2 \tag{2.26}$$

where ϕ_1 and ϕ_2 refer to the volume fractions of component 1 and 2, and ρ_1 and ρ_2 are the corresponding scattering length densities. Using the normalization condition of the Debye correlation function, the invariant can also be written as

$$\left\langle \eta^2 \right\rangle = \frac{1}{2\pi^2} \int_0^\infty Q^2 I(Q) \, dQ, \tag{2.27}$$

which is a practical way to calculate this quantity. In SANS experiments, the measured intensities $I(Q)$ always contain a certain amount of error caused by the uncertainty in the absolute intensity calibration. However, when the scattering intensity is measured over a sufficiently large Q range, the error can be canceled out by dividing the measured intensity by the invariant calculated according to Eq. 2.27.

2.3 Experimental Setup for SANS

The schematic diagram of the experimental setup for SANS experiments is shown in Figure 2-2. There are two types of neutron sources for SANS facilities : contin-

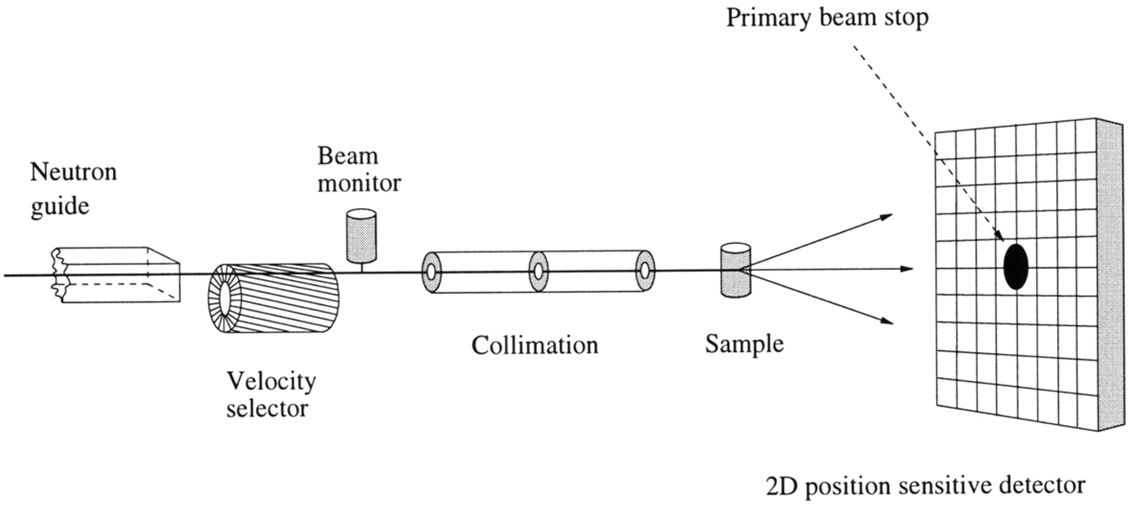

Figure 2-2: Principle of a small-angle neutron scattering facility

uous sources from nuclear research reactors and pulsed spallation sources based on accelerators. While SANS facilities based on the pulsed spallation sources utilize a white neutron beam (which contains neutrons of a certain range of wavelength) by time-of-flight measurements, those based on continuous sources use single wavelength neutrons. Except for this difference, the underlying principles are the same for both. Figure 2-2 demonstrates the principle of a SANS facility based on a continuous neutron source. A beam of neutrons with a broad spectrum of wavelengths is guided into a velocity selector where a mono-energetic neutron beam is prepared. To maintain its cross sectional size, the mono-energetic neutron beam is collimated through a series of pin holes before it hits the sample. The scattered neutrons are detected by a two-dimensional position sensitive detector. At the center of the detector, there is a beam stop to block the direct neutrons which passed through the sample without scattering. The scattering angle is determined by the detected position at the detector and the sample to detector distance. To cover a wider range of scattering angle, the detector can be moved back and forth parallel to the direction of neutron beam. For a very small scattering angle, the sample to detector distance can be made as long as 30 m. All the detected neutron counts are normalized by the beam monitor counts before data reduction.

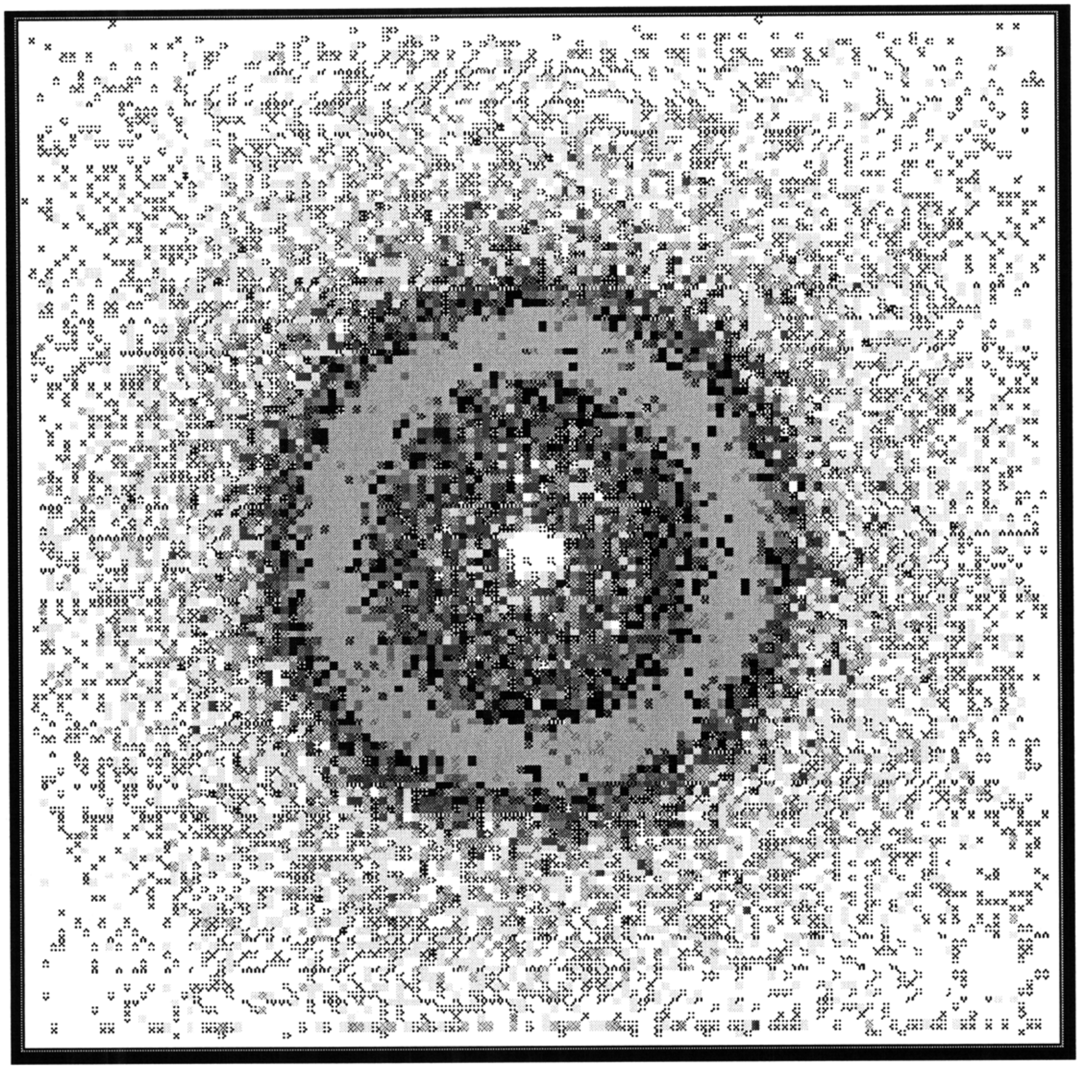

Figure 2-3: 2-dimensional small-angle neutron scattering pattern from a bicontinuous microemulsion

Figure 2-3 shows a representative two-dimensional scattering pattern of a bicontinuous microemulsion. The uniform ring pattern produced by Bragg scattering tells us that the bicontinuous microemulsion is an isotropic system. Therefore, the two-dimensional scattering pattern can be reduced into a meaningful one-dimensional scattering intensity by circular averaging. Figure 2-4 shows the corresponding absolute intensity $I(Q)$. The peak corresponds to the ring pattern in two-dimensional intensity. The information contained in this scattering intensity will be fully discussed in the following chapters.

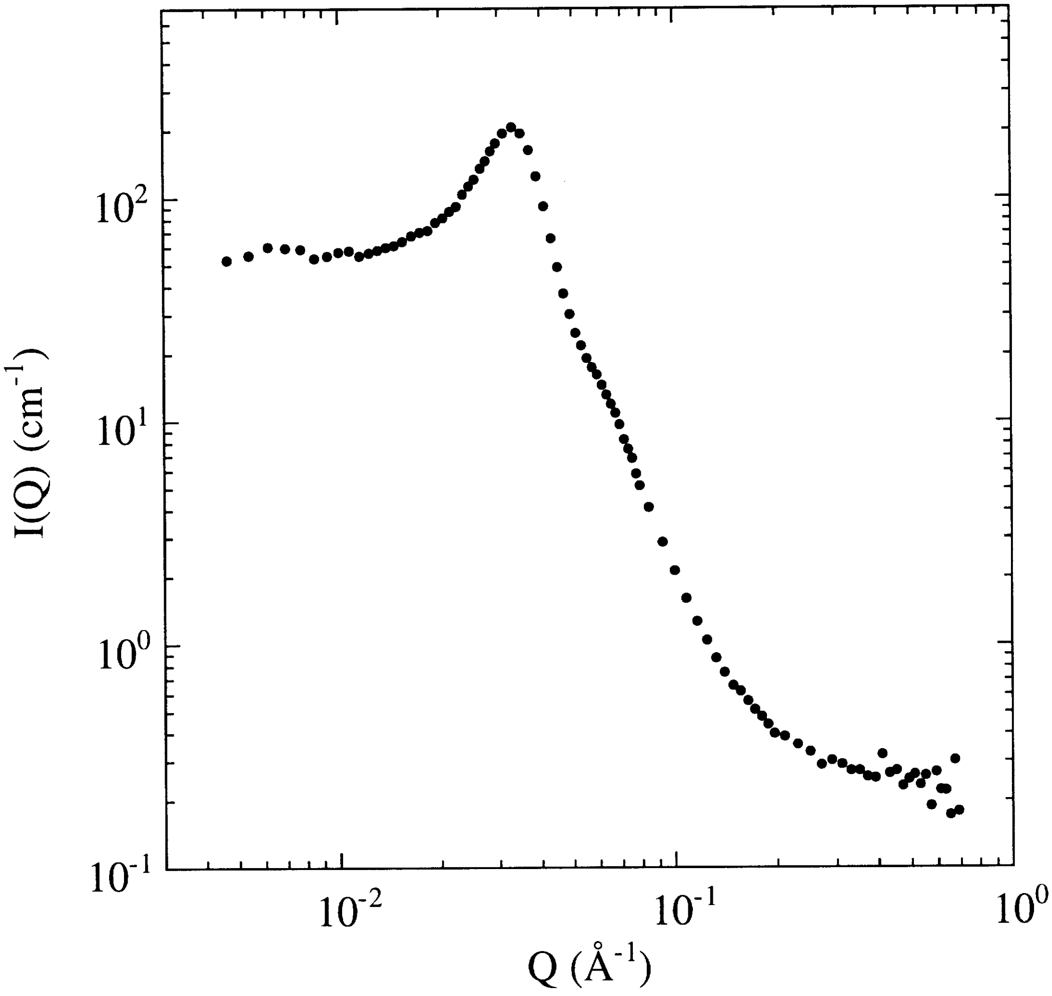

Figure 2-4: 1-dimensional small-angle neutron scattering pattern from a bicontinuous microemulsion

2.4 Contrast Variation

Neutrons are scattered by the nuclei of the sample and the coherent scattering length of nuclei depends on the number of particles in a nucleus, in particular on its total spin. The difference between isotopes of the same element are as large as those between different elements[33, 34]. This allows the use of isotopic labeling. In particular, the difference between hydrogen and deuteron is one of the largest that can be obtained : $b_H = -0.3742 \times 10^{-12}$ cm and $b_D = 0.6671 \times 10^{-12}$ cm[35].

For small-angle scattering, the quantities of interest are the scattering length densities $\rho = N_A b/v$, where N_A is Avogadro's number and V is the molar volume. Figure 2-5 shows the scattering length densities of water, oil, and surfactant. The deutrated and protonated compounds are very different in the scattering length density. By properly mixing the two, we can achieve any value of the scattering length density in a certain range bounded by the values of the pure protonated and the pure deutrated compounds, thereby allowing us to generate contrast variation within the sample. Figure 2-6 shows how the scattering length densities of components can be matched to manifest the different interfaces within the sample. When the scattering length density of water (or oil) is matched with that of the surfactant, from the neutron's point of view the three component system becomes a pseudo two component system with interfaces facing oil (or water) and surfactant. This type of scattering length density matching is called a bulk contrast. On the other hand, if we matched water and oil, neutrons see only the thin films made of surfactant molecules, a situation which is called a film contrast. Other than these three extreme cases, we can produce any intermediate contrast if necessary. This is very powerful technique to differentiate some regions of the sample from the rest. SANS experiments were performed for a bicontinuous microemulsion with the three different contrasts and Figure 2-7 shows the corresponding absolute intensities in which we can clearly see the variation of $I(Q)$ depending on the contrast.

While the substitution of hydrogen by deuteron produces a good contrast between water and hydrocarbon or between two hydrocarbons, there are artifacts associated

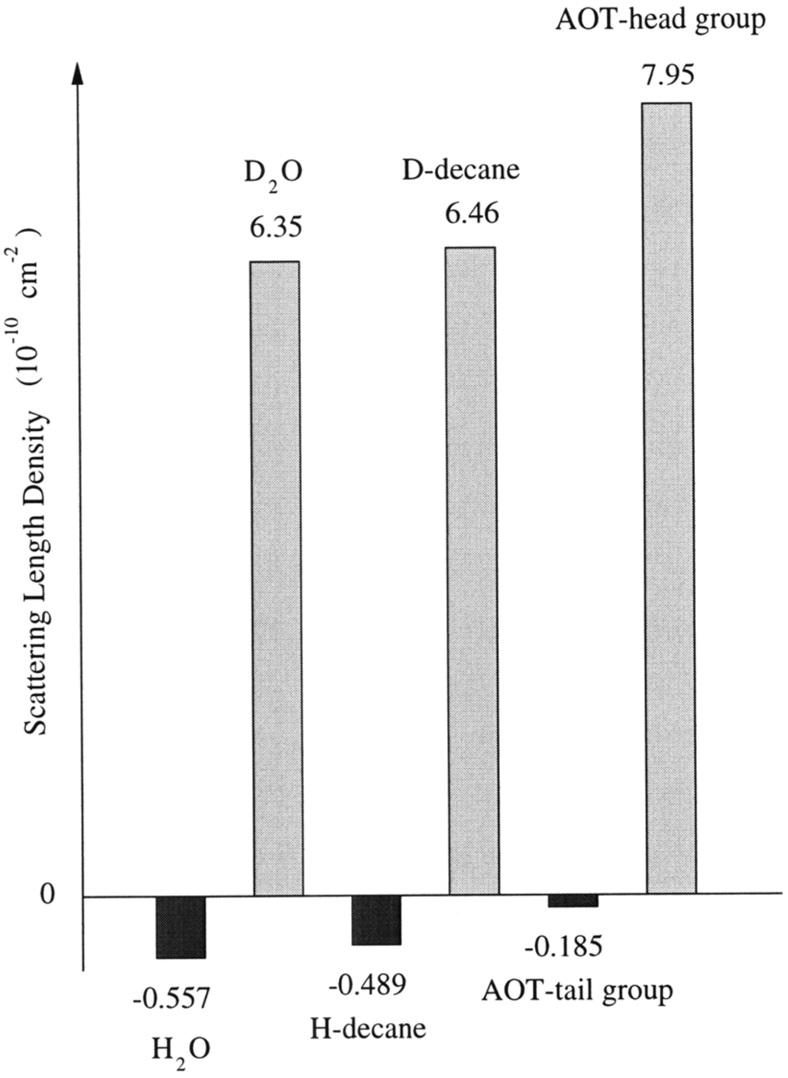

Figure 2-5: Scattering length densities of water, oil and surfactant.

with the method[36, 37, 38]. The physical chemistry of deutrated liquids is not identical to that of protonated ones : the strengths of hydrogen bonds and that of hydrophobic attractions are slightly changed. For example, a 1 to 2 °C shift in the temperatures of the phase boundaries is often observed[37]. However, these effects can be minimized by properly adjusting the experimental conditions such as temperature or salinity for each sample.

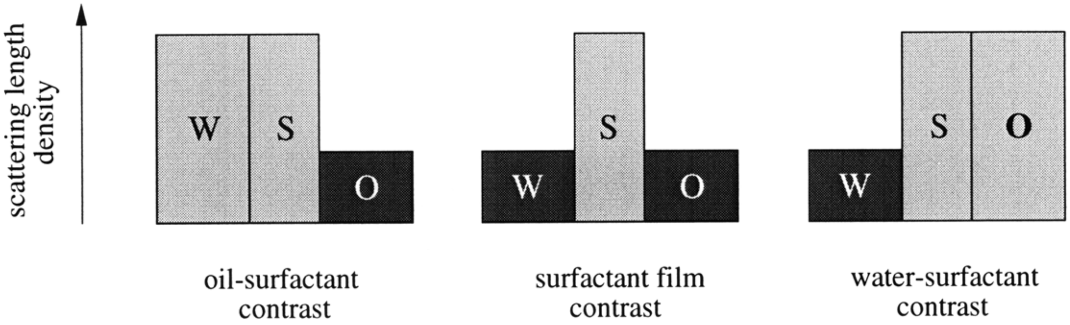

Figure 2-6: Contrast variation to differentiate the various interfaces.

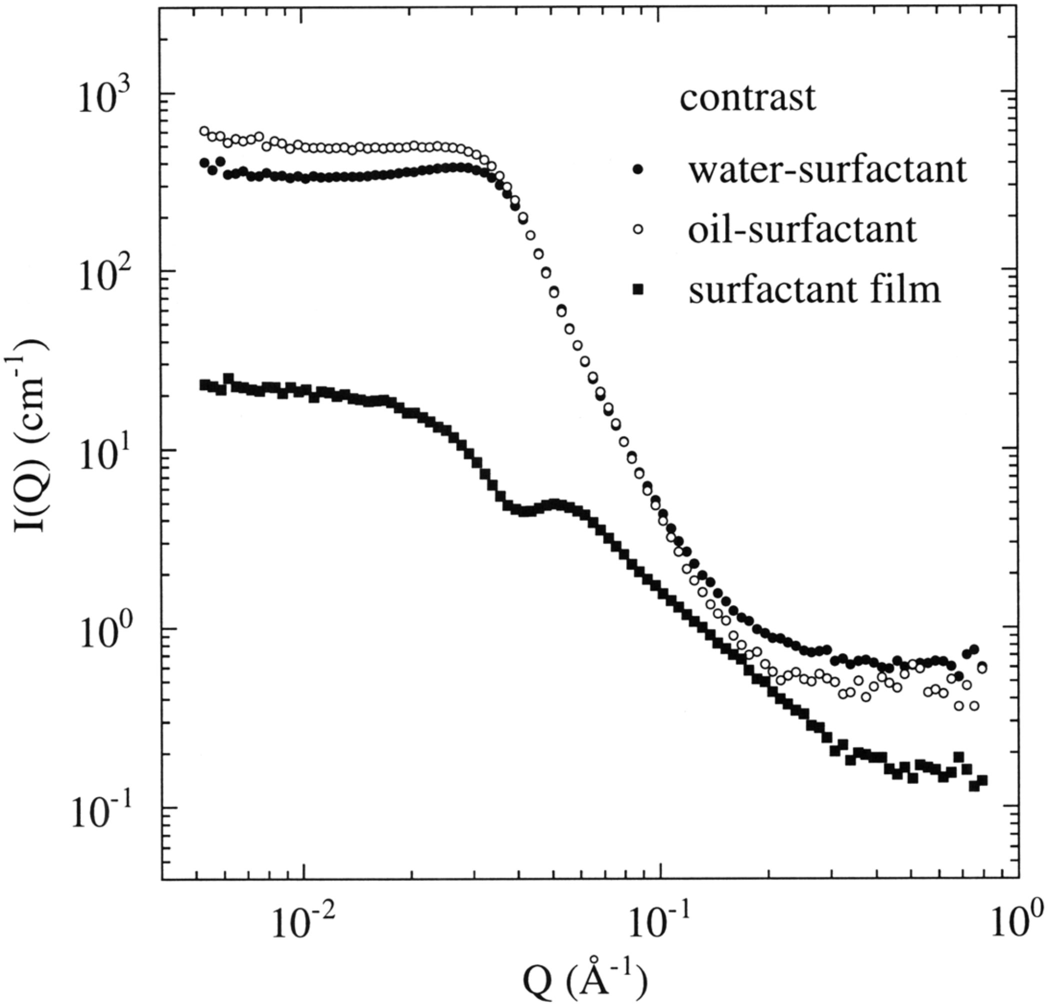

Figure 2-7: Reduced SANS intensities from a microemulsion with contrast variations

Chapter 3

Clipped Random Wave Model

The information provided by scattering techniques does not yield an image of the structures within the sample but rather an image of all its correlations. This is due to the phase information lost during the detection process. Since we do not have the full information for reconstructing the structure of the system, we need a model which is based on physically meaningful assumptions and is consistent with the measured scattering intensity. Here we introduce a new model developed for SANS intensity data analysis to extract the structural information of random porous materials in terms of interfacial curvatures. This model also can be used to reconstruct the three-dimensional structures of porous materials including microemulsions.

3.1 Scattering from Random Porous Materials

As shown in Chapter 2, the intensity distribution of SANS from an isotropic, disordered two-component porous material can be calculated generally from a one-dimensional Fourier transform of the normalized Debye correlation function $\Gamma(r)$,

$$I(Q) = \left\langle \eta^2 \right\rangle \int_0^\infty \Gamma(r) \frac{\sin(Qr)}{Qr} 4\pi r^2 dr, \tag{3.1}$$

where the subscript D is dropped for simplicity. Therefore, all the intrinsic properties of the sample system are contained in the Debye correlation function. Then the role of a physical model is to provide a proper Debye correlation function which, after Fourier transform, can be compared with the measured SANS intensities. Before going into the details of the model, we consider the general properties of the Debye correlation function.

There are two physical boundary conditions that $\Gamma(r)$ must satisfy

$$\begin{aligned} \Gamma\left(r=0\right) &= 1 \\ \Gamma\left(r=\infty\right) &= 0, \end{aligned} \tag{3.2}$$

which can be easily inferred from the definition of the Debye correlation function given in Eq. 2.25. The most important property of $\Gamma(r)$ for the bulk contrast case with a sharp boundary between two regions of different scattering length densities is that it has linear and cubic terms under small r expansion. The corresponding coefficients contain very important information,

$$\begin{aligned} \Gamma\left(r\rightarrow 0\right) &= 1 - c_1 r + c_3 r^3 + \cdots \\ &= 1 - \frac{1}{4\phi_1\phi_2}\left(\frac{S}{V}\right) r \left(1 - \frac{c_3}{c_1}\right) r^2 + \cdots. \end{aligned} \tag{3.3}$$

The coefficient of the linear term, c_1, is proportional to the specific interface, and the ratio of the coefficient of the cubic term to that of the linear term has been given by Kirste and Porod[39] in terms of curvatures as

$$\frac{c_3}{c_1} = \frac{1}{8}\left\langle H^2\right\rangle - \frac{1}{24}\left\langle K\right\rangle. \tag{3.4}$$

The appearance of the surface to volume ratio in the small r expansion of the Debye correlation function can be understood by the following. We consider a two component porous system with volume fractions of ϕ_1 and ϕ_2, and scattering densities ρ_1 and ρ_2. The Deybe correlation function at R is related to the probability that two random points in the medium separated by a distance R are either in the same phase or different phases. When R is very small, the probability that the two points are in different phases is proportional to how much densely the interfaces, which separate the two phases, are distributed. This explains the surface to volume ratio appearing in Eq. 3.3.

Since the scattering vector Q is reciprocally related to distance r, the small r expansion of the Debye correlation function is closely related to the large Q behavior of $I(Q)$. By integrating Eq. 3.1 by parts, we can obtain a large Q expansion of $I(Q)$,

$$I(Q) = -\left\langle \eta^2 \right\rangle \left(\frac{8\pi\Gamma'(0)}{Q^4} - \frac{16\pi\Gamma'''(0)}{Q^6} + O\left(Q^{-8}\right) \right). \tag{3.5}$$

Inserting the first derivative of Eq. 3.3 at $r = 0$ into Eq. 3.5, we obtain a relation,

$$\lim \left[I\left(Q\right) \right]_{Q \to \infty} = \frac{\langle \eta^2 \rangle}{\phi_1 \phi_2} 2\pi \left(\frac{S}{V} \right) Q^{-4} \tag{3.6}$$

This is called Porod's law[40] which is attributed to the existence of a well-defined internal interface[41, 32, 42, 43] and is widely used to to extract the surface to volume ratio by fitting the scattering at large Q.

3.2 Models for the Debye Correlation Function

A model which describes the structure of a certain system need to contain characteristic length scales of the system. Therefore the Debye correlation function which represents a spatial density correlation needs to contain certain characteristic length scales of the system. Here we briefly review a few representative models of the Debye correlation function.

The original Debye correlation function [32] proposed for porous materials which have a completely random pore size distribution is an exponentially decaying function,

$$\Gamma_{Debye}\left(r\right) = exp\left(-\frac{r}{\xi} \right) \tag{3.7}$$

where ξ is related to the specific interface as

$$\frac{1}{\xi} = \frac{1}{4\phi_1 \phi_2} \left(\frac{S}{V} \right). \tag{3.8}$$

Considering that most porous materials, such as bicontinuous microemulsions and Vycor glass, have been found to have a scattering peak at finite Q, the exponentially decaying form of $\Gamma_{Debye}(r)$ with no peak is not quite appropriate. The peak found experimentally is due to a domain structure which produces short range correlation. This requires the Debye correlation function to have an oscillatory factor as well as the exponential decay.

From the phenomenological Landau free energy[44] for microemulsions[45],

$$F(\psi) = \int \left[a_2\psi^2 + c_1(\nabla\psi)^2 + c_2(\Delta\psi)^2\right] d^3\psi \tag{3.9}$$

where ψ is an order parameter, Teubner and Strey [46] proposed a two-parameter Debye correlation function which yields a single broad scattering peak. In the Teubner-Strey model, the Debye correlation function is

$$\Gamma_{TS}(r) = \exp\left(-\frac{r}{\xi}\right)\left(\frac{d}{2\pi r}\right)\sin\left(\frac{2\pi r}{d}\right) \tag{3.10}$$

where d is the inter-domain distance (water-to-water or oil-to-oil) and ξ the coherence length. The corresponding structure factor is

$$S(Q) = \frac{8\pi/\xi}{a^2 - 2Q_m^2 Q^2 + Q^4} \tag{3.11}$$

where the constant a and the peak position Q_m are given as

$$a = \left(\frac{2\pi}{d}\right)^2 + \left(\frac{1}{\xi}\right)^2 \tag{3.12}$$

$$Q_m^2 = \left(\frac{2\pi}{d}\right)^2 - \left(\frac{1}{\xi}\right)^2 \tag{3.13}$$

This two-length scale Teubner-Strey model describes the scattering intensity from bicontinuous microemulsions fairly well, but shows appreciable deviation from experimental data at high Q. Furthermore, since the model does not involves any process which realizes the micro-phase separation, its application to the measurement of interfacial curvatures is not valid. The proper form of the Debye correlation function which agrees with the scattering intensity over the whole Q-range and is suitable for interfacial curvature measurement is described in the following section.

3.3 Clipped Random Wave Model

To calculate the Debye correlation function for bicontinuous microemulsions, we adopted the clipped random wave (CRW) model. The CRW model was an idea originally introduced by Cahn[47] to describe the morphology of spinodally decomposed binary alloys and was recently implemented for the case of bicontinuous microemulsions[48, 49].

Continuous interfaces can be mathematically modeled by clipping a stochastic standing wave $\Psi\left(\vec{r}\right)$ at a certain level. In the CRW model, $\Psi\left(\vec{r}\right)$ is constructed from the superposition of a large number N of cosine waves with random wave vectors, $\vec{k_i}$, and random phases ϕ_i

$$\Psi\left(r\right) = \sqrt{\frac{2}{N}}\sum_{i=1}^{N}\cos\left(k_i r + \phi_i\right), \tag{3.14}$$

where ϕ_i are uniformly distributed on $[0, 2\pi)$ and, for an isotropic morphology, the probability density $f\left(\vec{k}\right)$ of $\vec{k_i}$ is rotationally symmetric. In another words, the directions of $\vec{k_i}$ are uniformly distributed over solid angle 4π.

It can be shown that the random function $\Psi\left(\vec{r}\right)$ given by Eq. 3.14 is a Gaussian random field [50] with zero mean and spectral function $f\left(k\right)$. The Gaussian random field is a field whose probability density function $P\left(\Psi\right)$ is given by the Gaussian distribution,i.e.

$$P\left(\Psi\right) = \frac{1}{\sqrt{2\pi}}\exp\left(-\frac{\Psi^2}{2}\right) \tag{3.15}$$

The statistical properties of a Gaussian random field with zero mean is completely characterized by its two-point correlation function, defined as

$$g\left(\left|\vec{r_1} - \vec{r_2}\right|\right) = \left\langle\Psi\left(\vec{r_1}\right)\Psi\left(\vec{r_2}\right)\right\rangle \tag{3.16}$$

and which has a Fourier transform relation with the spectral function $f(k)$,

$$g(|\vec{r_1}-\vec{r_2}|)=\int_0^{\infty}4\pi k^2 j_0(k|\vec{r_1}-\vec{r_2}|)\,f(k)\,dk \tag{3.17}$$

The density function $\rho(\vec{r})$ of two-component media, each component having uniform density, can be considered as a discrete function which has either ρ_1 or ρ_2 at $\vec{r}$ depending on the phase (either component 1 or 2). To realize micro-phase separated two component media, the continuous Gaussian random field $\Psi(\vec{r})$ is clipped into a discrete random field $\zeta(\vec{r})$[48, 51, 52, 53, 54]. This clipping process can be described as

$$\zeta(\vec{r})=\Theta_\alpha(\Phi(\vec{r}))=\begin{cases}1,\text{when}\Psi(\text{r})\geq\alpha\\ 0,\text{otherwise}\end{cases} \tag{3.18}$$

where Θ_α is a step function. α, called *the clipping level*, is chosen to give the required volume fractions for the two phases and an interfaces between two material phases is defined by $\Psi(\vec{r})=\alpha$. For example, $\alpha=0$ corresponds to an isometric($\phi_1=\phi_2=0$) system. The Debye correlation function for the discrete $\zeta(\vec{r})$ is given exactly by

$$\Gamma(r)=\frac{\langle\zeta(0)\zeta(r)\rangle-\langle\zeta\rangle^2}{\langle\zeta\rangle-\langle\zeta\rangle^2} \tag{3.19}$$

where $\langle\zeta\rangle$ and $\langle\zeta\rangle^2$ are calculated as [51]

$$\begin{aligned}\langle\zeta\rangle &= \int_{-\infty}^{+\infty}P(\Psi)\,\zeta(\Psi)\,d\Psi\\ &= \frac{1}{2}-\frac{1}{\sqrt{2\pi}}\int_0^{\alpha}\exp\left(-\frac{\Psi^2}{2}\right)d\Psi\end{aligned} \tag{3.20}$$

$$\langle\zeta(0)\zeta(r)\rangle = \langle\zeta\rangle-\frac{1}{2\pi}\int_0^{cos^{-1}(g(r))}\exp\left(-\frac{\alpha}{1-cos\theta}\right)d\theta \tag{3.21}$$

The average value of the clipped Gaussian random field $\langle\zeta\rangle$ and its complement $1-\langle\zeta\rangle$ correspond to the volume fractions of the major and minor phases ϕ_1 and ϕ_2 respectively. Using Eq. 3.21 and $\langle\zeta\rangle=\phi_1$, the Debye correlation function given in

Eq. 3.19 can be rewritten as

$$\Gamma(r) = 1 - \frac{1}{2\pi\phi_1\phi_2}\int_0^{\cos^{-1}(g(r))} \exp\left(-\frac{\alpha^2}{1+\cos\theta}\right) d\theta \tag{3.22}$$

For small α, meaning a slight deviation from an isometric case, Eq. 3.22 can be approximated as

$$\Gamma(r) \cong 1 - \frac{1}{2\pi\phi_1\phi_2}\left[\cos^{-1}(g(r)) - \alpha^2 \tan\left(\frac{\cos^{-1}(g(r))}{2}\right)\right] \tag{3.23}$$

where the volume fraction ϕ_1 can be approximated as

$$\phi_1 \cong \frac{1}{2} - \frac{\alpha}{\sqrt{2\pi}}. \tag{3.24}$$

For an isometric system, i.e. $\phi_1 = \phi_2 = 0.5$ and $\alpha = 0$, Eq. 3.22 reduces to a very simple form

$$\Gamma(r) = \frac{2}{\pi}\sin^{-1}(g(r)). \tag{3.25}$$

Considering the complexity of the procedure involved in the CRW model, Eq. 3.25 is a remarkably simple expression for the Debye correlation function.

3.4 Specific Interface in the CRW Model

The specific interface is one of the most important quantities which describe the property of the porous material. As shown in section 3.1, traditionally the specific surface in a two-phase medium with a sharp interface has been determined by applying the Porod's law [40] to the large Q region of the neutron or x-ray scattering intensities.

In the CRW model, an alternative way of extracting the specific interface, which utilizes the scattering intensity over the whole Q range, is derived. The small r expansion of $g(r)$ can be obtained by expanding $j_0(kr)$ (setting $r_1 = 0$) in Taylor series,

$$g(r) \quad = \quad \int_0^\infty 4\pi k^2 \left[1 - \frac{1}{6}k^2r^2 + \frac{1}{120}k^4r^4 + \cdots\right] f(k)\, dk$$

$$= 1 - \frac{1}{6}\left\langle k^2 \right\rangle r^2 + \frac{1}{120}\left\langle k^4 \right\rangle r^4 + \cdots \tag{3.26}$$

where we used the normalization condition of the spectral function $f(k)$, and $\langle k^2 \rangle$ and $\langle k^4 \rangle$ denote the 2nd and 4th moment of $f(k)$. Note that this expansion has a quadratic term followed by a quartic term. Using the result of Eq. 3.26 in Eq. 3.22, we obtain a small r expansion of the Debye correlation function

$$\Gamma(r \to 0) = 1 - \frac{\sqrt{\langle k^2 \rangle}}{2\pi\sqrt{3}\phi_1\phi_2} exp\left(-\frac{\alpha^2}{2}\right) r \left[1 - \left(\frac{1}{40}\frac{\langle k^4 \rangle}{\langle k^2 \rangle} - \frac{1}{72}\left\langle k^2 \right\rangle \left(\alpha^2 - 1\right)\right) r^2\right] \tag{3.27}$$

Comparing this with Eq. 3.3, we obtain the specific interface in a two-phase medium in terms of the 2nd moment of the spectral function $f(k)$

$$\left(\frac{S}{V}\right) = \frac{2}{\pi\sqrt{3}}\sqrt{\langle k^2 \rangle} exp\left(-\frac{\alpha^2}{2}\right). \tag{3.28}$$

Considering that the Porod's law is limited by the availability of large Q data and its statistics, Eq. 3.28 is a very useful expression which utilizes the scattering intensity over the whole Q range and therefore there is less uncertainty of the determination of the surface to volume ratio. This relation also implies that one of the basic requirements for the physically acceptable spectral function is that the 2nd moment be finite.

3.5 Three Basic Length Scales and Spectral Density Function

The proper application of the CRW model strongly depends on the choice of a physically meaningful spectral function. A few spectral functions in conjunction with the CRW model have been suggested [48, 51, 55, 56]. While they show certain prominent features in the scattering intensity of bicontinuous microemulsions, the information contained in the spectral functions is limited or their application to the measurement of all the interfacial curvatures is not valid. In this section, a new form of $f(k)$ which satisfies the fundamental requirements for a physically meaningful spectral function is introduced.

First, a natural requirement of $f\left(k\right)$ is that when it is used in the CRW model, it would give an intensity distribution which agrees with SANS data. Second, considering that, as given in Eq. 3.28, the specific interface which has to be finite is proportional to $\sqrt{\langle k^2\rangle}$, $f\left(k\right)$ must have a finite 2nd moment. Third, as it will be shown in the next section, the average square mean curvature is related to the 4th moment of $f\left(k\right)$ and therefore $f\left(k\right)$ also has to have a finite 4th moment.

We choose an inverse 8th-order polynomial containing three parameters a, b, and c, which are the minimal set for the physical situation under study

$$f\left(k\right)=\frac{bc\left(a^2+\left(b+c\right)^2\right)^2/\left(b+c\right)\pi^2}{\left(k^2+c^2\right)^2\left(k^4+2\left(b^2-a^2\right)k^2+\left(a^2+b^2\right)^2\right)}. \tag{3.29}$$

The three parameters are related to the three basic length scales in the interfacial structures as following,

$$\begin{aligned} a &= \frac{2\pi}{d} \qquad &(3.30)\\ b &= \frac{1}{\xi} \qquad &(3.31)\\ c &= \frac{1}{\delta} \qquad &(3.32)\end{aligned}$$

where d is the inter-domain distance (water-water or oil-oil), ξ the coherence length of the local order and δ the surface roughness parameter which describes the roughness of the surface. The 2nd and the 4th moments of the spectral function $f(k)$ given in Eq. 3.29 are calculated as

$$\begin{aligned} \left\langle k^2\right\rangle &= \frac{c\left(a^2+b^2+c^2\right)}{\left(b+c\right)} \qquad &(3.33)\\ \left\langle k^4\right\rangle &= \frac{c\left(a^4+2a^2b^2+b^4+4a^2bc+4b^3c+4b^2c^2+b^3c\right)}{\left(b+c\right)}.v \qquad &(3.34)\end{aligned}$$

The form of $f(k)$ given in Eq. 3.29 was determined not only by the requirements of moment finiteness but also by physical consideration of the measured scattering intensities. As discussed in section 3.2, the two-parameter Teubner-Strey model agrees well with the scattering intensities around the peak but deviates appreciably at the large Q region. Considering that the large Q data corresponds to small length scale fluctuation, the poor agreement of the Teubner-Strey model which contains only the large length scales is natural. The small length scale fluctuations occurs naturally in surfaces with ultra low elastic bending constants such as surfactant monolayers. To be able to explain the large Q region and correspondingly the small scale fluctuations, we introduced the new length scale δ in such a way that the spectral function given in Eq. 3.29 can produce the correct scattering intensities at the large Q. While typical values of d and ξ are 100's Å, those of δ are 10's Å or less.

Figure 3-1 shows the spectral function for a few representative sets of d, ξ, and δ, which explains the physical meaning of the three basic length scales. In Figure 3-1 a), we can see that changing d while keeping the ratio ξ/d (0.5) and δ (10 Å) constant shifts the peak position of the spectral function. It is noticeable that for each distribution of $f(k)$, the overall shapes are all the same. This tells us that d is a primary length scale which defines the underlying distance scale but not the shape of the structure. This confirms our interpretation of d as the inter-domain distance.

Figure 3-1 b) shows the effect of varying the ratio ξ/d with constant δ. While d (200 Å) and δ (10Å) are kept constant, ξ/d was increased from 0.25 to 2.0. In this case, while its position in k does not change, the shape of peak becomes shaper. This means that the system described by $f(k)$ becomes more ordered. Therefore, the ratio ξ/d is called a order parameter and in this context, the interpretation of ξ as a coherence length is clear.

In Figure 3-1 c), the effects of the surface roughness parameter δ on the large Q region is clear. In this graph, d (200 Å) and ξ (100 Å) is kept constant. As the value of δ changes, only the wing of $f(k)$ at shifts up and down: the smaller δ, the higher the wing. This clearly confirms our interpretation of δ as the surface roughness parameter which describes small length scale surface fluctuations.

Inserting Eq. 3.29 into Eq. 3.16, the corresponding two-point correlation function

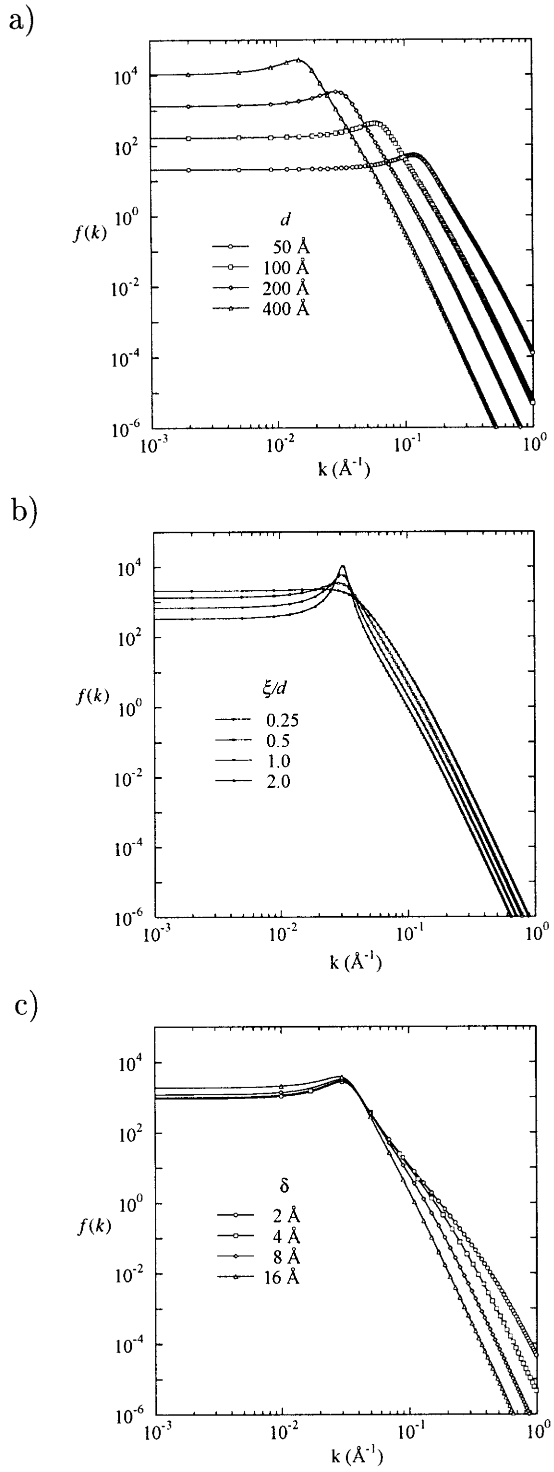

Figure 3-1: Effects of the three length scales on the spectral function. a) d, b) ξ/d and c) δ.

is obtained,

$$g(r) = \frac{4bc\left(a^2+(b+c)^2\right)^2}{(b+c)\,r}$$

$$\times\left[\exp(-cr)\left(\frac{a^2-b^2+c^2}{\left(4a^2b^2+(a^2-b^2+c^2)^2\right)^2}+\frac{r}{4c\left((a^2+b^2)^2+2(a^2-b^2)c^2+c^4\right)}\right)\right.$$

$$+\frac{\exp(-br)}{ab}\left(\frac{-8a^2b^2+(a^2+b^2)^2+2(a^2-b^2)^2+2(a^2-b^2)c^2+c^4}{4\left(4a^2b^2+(a^2-b^2+c^2)^2\right)^2}\sin(ar)\right.$$

$$\left.\left.-\frac{ab(a^2-b^2+c^2)}{\left(4a^2b^2+(a^2-b^2+c^2)^2\right)^2}\cos(ar)\right)\right] \tag{3.35}$$

Inserting Eq. 3.35 into Eq. 3.22 or Eq. 3.25, we can calculate the Debye correlation function. Once we know the Debye correlation function, we can calculate the absolute intensity $I(Q)$ by Eq. 3.1 and compare it with the measured scattering intensities.

Using the same parameters used in Figure 3-1, the Debye correlation function was calculated for isometric systems by Eq. 3.25 and Eq. 3.35. Figure 3-2 shows the results. This explains the effects of the three basic length scales on the real space function $\Gamma(r)$. The second zero crossing point of $\Gamma(r)$ corresponds to the inter-domain distance d and the first zero crossing point, which is exactly half of the inter-domain distance, is the distance between the two phases, e.g., water and oil. In Figure 3-2 a), we can see the systematic change of the zero crossings with d.

The oscillation of $\Gamma(r)$ is directly related to the local order of the system. For example, a perfect crystal will generate sinusoidal oscillation with a constant amplitude of unity. Since the system considered here has random disordered structures, the oscillation of $\Gamma(r)$ decays dramatically within a range of less than a single inter-domain distance. Figure 3-2 a) shows the decay of the oscillatory $\Gamma(r)$ as a function

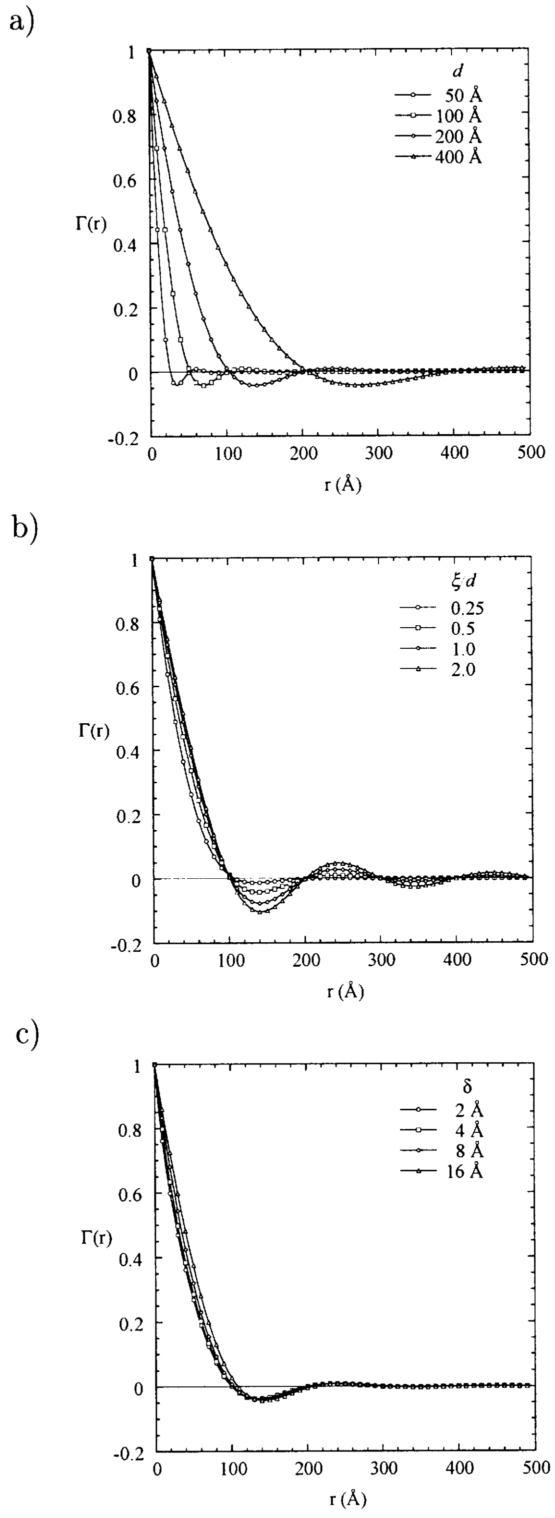

Figure 3-2: Effects of the three length scales on the Debye correlation function. a) d, b) ξ/d, and δ.

of the order parameter ξ/d : the smaller the value of ξ/d, the faster the decay of the oscillation.

Figure 3-2 c) shows the effects of δ. We can see that the change of $\Gamma(r)$ at small r depends on the value of δ : the smaller δ, the faster the decay of $\Gamma(r)$. In the section 3.1, it was shown that the slope of $\Gamma(r)$ in the small r region is directly proportional to the surface to volume ratio. Therefore, smaller δ corresponds to larger surface to volume ratio. This makes sense because in order to distribute more surfaces in a finite volume, the surfaces have to be more strongly wrinkled resulting in a smaller value of δ.

3.6 Interfacial Curvatures

In this section, we discuss the mathematical definition of an interface and show how one can calculate the curvatures of a general interface. We then relate the interfacial curvatures to the spectral density function defined in the CRW model.

We consider a surface M in a three-dimensional Euclidean space $\mathbf{E}^3$. The surface can be described by the parametric form $x = f(u,v)$, $y = g(u,v)$, and $z = h(u,v)$, or by the implicit form $F(x,y,z) = 0$. For our convenience, here we use the impilicit representaion.

It is well known that the curvature of a linear object is given by the change of the tangent as one moves along the arclength of the curve. Similarily, the curvature of a curve on the surface can be derived from the implicit form of the surface, $F(x,y,z) = 0$ by considering the change in the normal vector field as one proceeds along the surface. Realizing that on the surface, where F is a constant, the total derivative of F is zero, one can show that ∇F is orthgonal to the surface and thus, the unit normal vector field $\hat{U}$ of the surface is given by

$$\hat{U} = \frac{\nabla F}{|\nabla F|} \tag{3.36}$$

It is known that the shape of the surface M is described infinitesimally by a certain

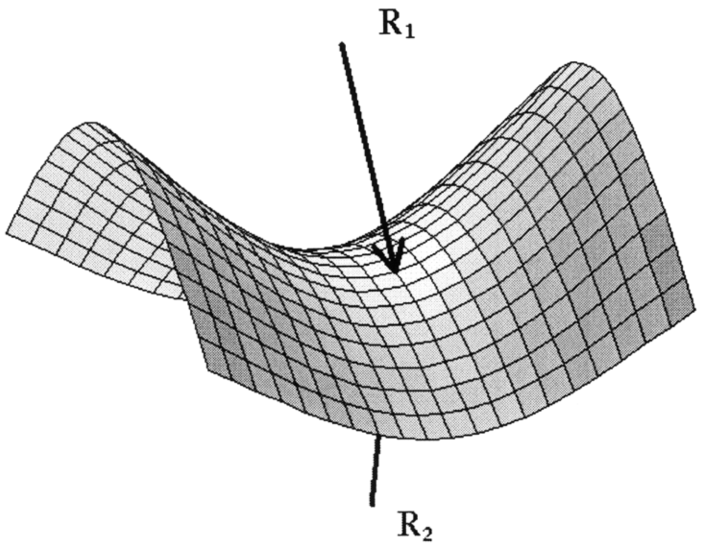

Figure 3-3: Principal radii of curvature on a saddle shaped interface

linear operator S called a shape operator[57, 58] defined on each . If $\vec{p}$ is a point of M, then for each tangent vector $\vec{v}$ to M at $\vec{p}$, the shape operator S_p of M at $\vec{p}$ is defined as the directional (along $\vec{v}$) gradient of a unit normal vector field $\hat{U}$ on a neighborhood of $\vec{p}$ in M,

$$S_p\left(\vec{v}\right) = -\nabla_v \hat{U}. \tag{3.37}$$

It can be shown that the shape operator has two eigenvalues called the principal curvatures, $1/R_1$ and $1/R_2$, which are the maximum and minimum of normal curvature at the point $\vec{p}$. The normal curvature $1/R$ is defined as

$$1/R = -\nabla_u \hat{U} \cdot \vec{u} \tag{3.38}$$

where $\vec{u}$ is a unit tangent vector at a point $\vec{p}$ and the sign of the normal curvature is determined by the choice of the normal vector field $\hat{U}$. Figure 3-3 shows the two principal radii of curvature at a point on a saddle shaped interface separating water and oil.

The two invariants, the Gaussian and mean curvatures, which are intrinsic properties of the surface are defined in terms of the shape operator. The Gaussian curvature, K, is a half of the trace of the shape operator and the mean curvature, H, is the determinant of the shape operator:

$$\begin{aligned} K &= \det S, && (3.39) \\ H &= \frac{1}{2}\mathrm{trace} S. && (3.40) \end{aligned}$$

Since the shape operator has two non-zero eigenvalues called principal curvatures, the Gaussian and mean curvatures can be also given in terms of the principal curvatures :

$$\begin{aligned} K &= \frac{1}{R_1 R_2}, && (3.41) \\ H &= \frac{1}{2}\left(\frac{1}{R_1} + \frac{1}{R_2}\right). && (3.42) \end{aligned}$$

A complete knowledge of the Gaussian and mean curvatures at every point on the surface corresponds to the complete informations about the shape of the surface. A significant fact about the Gaussian curvature is that it is independent of the choice of the unit normal vector $\hat{U}$. If $\hat{U}$ is changed to $-U$, then the sign of both $1/R_1$ and $1/R_2$ change, so K is unaffected. This is obviously not the case with mean curvature H, which has the same ambiguity of the sign as the principal curvatures themselves. Here, we choose the sign convention in such a way that a principal curvature concave towards water is considered positive. Therefore, in Figure 3-3, R_1 is positive and R_2 is negative. The signs of the Gaussian and mean curvatures are crucial information needed to determine the shape of surfaces. On a saddle shaped surface, the Gaussian curvature is always negative for every point and the sign of the mean curvature is determined by the magnitude of R_1 and R_2. On a surface concave towards water, both curvatures are positive and on a surface that is concave towards oil, the Gaussian curvature is positive and the mean curvature is negative.

The Gaussian and mean curvatures can be expressed in terms of the first and second derivative of $F(x, y, z)$. First, we insert Eq. 3.36 into Eq. 3.37 and second take a determinant and a trace of the resulting shape operator. From this we find an expression for the Gaussian curvature:

$$K = \frac{1}{\mathcal{M}^4}\left[F_{xx}F_{yy}F_z^2 - F_{xy}^2F_z^2 + 2F_{xz}F_x\left(F_yF_{yz} - F_zF_{yy}\right) + Perm\right] \tag{3.43}$$

where

$$\mathcal{M} = \sqrt{F_x^2 + F_y^2 + F_z^2} \tag{3.44}$$

and the term *Perm* indicates that one should consider two additional permutations of each term : $(x, y, z) \to (z, x, y)$ and $(x, y, z) \to (y, z, x)$. The mean curvature is given by

$$H = \frac{1}{2\mathcal{M}^3}\left[F_{xx}\left(F_y^2 + F_z^2\right) - 2F_xF_yF_{xy} + Perm\right]. \tag{3.45}$$

To understand the overall geometry of a random interface, we need to consider the statistical average of the curvatures over the whole interface. The average Gaussian and mean curvatures are defined as

$$\langle K\rangle = \left\langle\frac{1}{R_1R_2}\right\rangle \tag{3.46}$$

$$\langle H\rangle = \frac{1}{2}\left\langle\left(\frac{1}{R_1} + \frac{1}{R_2}\right)\right\rangle \tag{3.47}$$

where the statistical averages are taken over all points on the interface. According to the Gauss-Bonnet theorem[57] in differential geometry, the average Gaussian curvature is proportional to the Euler characteristics of the random interface and is a topological invariant measuring the number of particles minus the number of holes in the particles. Figure 3-4 shows the average Gaussian curvatures for three different closed interfaces.

Another important quantity is the average square mean curvature $\langle H^2\rangle$ which is defined as

$$\left\langle H^2\right\rangle = \frac{1}{4}\left\langle\left(\frac{1}{R_1} + \frac{1}{R_2}\right)^2\right\rangle. \tag{3.48}$$

The average square mean curvature is proportional to the bending energy, and together with the average Gaussian and meancurvatures, plays a prominent role in the

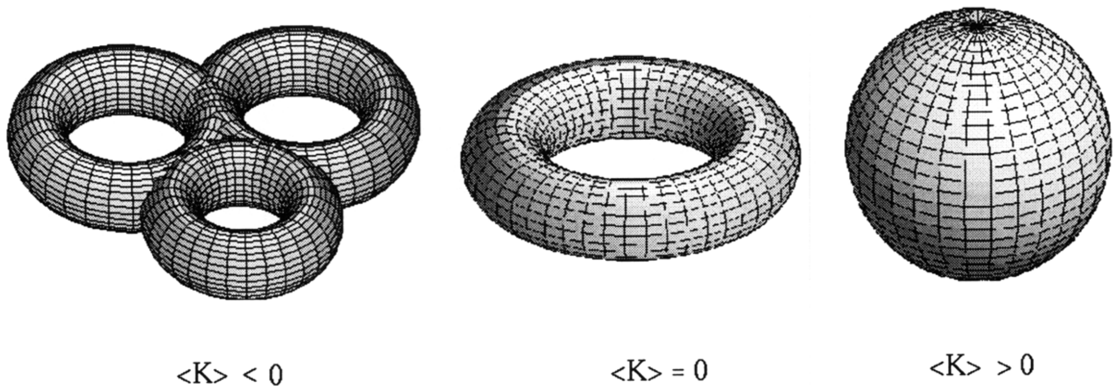

Figure 3-4: The Average Gaussian Curvature and the Gauss-Bonnet Theorem : $\langle K\rangle\, S_{total} = 4\pi\,(1-n)$ where n is the number of holes on a closed surface.

theories of microemulsions [59, 60, 61, 62, 63].

To connect the interfacial curvatures with the random surface in the CRW model, we consider a random interface $\Psi(\vec{r})$ generated by the level set α,

$$\Psi(\vec{r}) = \alpha \tag{3.49}$$

where the function $\Psi(\vec{r})$ is defined by Eq. 3.14. Here, $\Psi(\vec{r}) - \alpha$ corresponds to $F(\vec{r})$ in the implicit form of a surface. Inserting the first and second derivatives of $\Psi(\vec{r}) - \alpha$ into Eq. 3.43 and 3.45, and averaging over the whole interface, we obtain expressions of $\langle K\rangle$ and $\langle H\rangle$ in terms of the clipping level α and the moments of the spectral function $f(k)$[51]:

$$\begin{aligned}
\langle H\rangle &= \frac{\alpha}{2}\sqrt{\frac{\pi}{6}\,\langle k^2\rangle}, && (3.50)\\
\langle K\rangle &= \frac{1}{6}\left\langle k^2\right\rangle\left(\alpha^2-1\right), && (3.51)\\
\left\langle H^2\right\rangle &= \frac{1}{6}\left\langle k^2\right\rangle\left(\alpha^2+\nu^2\right), && (3.52)
\end{aligned}$$

where

$$\nu^2 = \frac{6}{5}\frac{\langle k^4 \rangle}{\langle k^2 \rangle^2} - 1. \tag{3.53}$$

Inserting $\langle k^2 \rangle$ and $\langle k^4 \rangle$ given in Eq. 3.33 and 3.34, the interfacial curvatures can be given in terms of a, b, and c ,i.e. d, ξ and δ, explicitly,

$$\langle K \rangle = \frac{(\alpha^2 - 1)}{6}\frac{c\,(a^2 + b^2 + bc)}{(b + c)} \tag{3.54}$$

$$\langle H \rangle = \frac{\alpha}{2}\sqrt{\frac{\pi}{6}\frac{c\,(a^2 + b^2 + bc)}{(b + c)}} \tag{3.55}$$

$$\begin{aligned}\langle H^2 \rangle &= \frac{\alpha^2}{6}\frac{c\,(a^2 + b^2 + bc)}{(b + c)}. \\ &+ \frac{a^4\,(6b + c) + a^2\,(12b^3 + 26b^2c + 14bc^2) + 6b^5 + 25b^4c + 38b^3c^2 + 25b^2c^3 + 6bc^4}{30\,(b + c)\,(a^2 + b^2 + bc)}\end{aligned} \tag{3.56}$$

Once the three basic length scales and the clipping level α are determined, the average interfacial curvatures can be calculated using Eq. 3.54, 3.55, and 3.56.

3.7 Simulation of Three-Dimensional Structures

The CRW model is very powerful not only because it allows us to estimate the interfacial curvatures but also because it permits us to simulate the three-dimensional structure of systems under investigation using corresponding estimated spectral functions. The procedure for the simulation of three-dimensional structures is essentially built in the CRW model[56, 53].

Once we determine the spectral function of the system from SANS intensities, the Gaussian random field $\Psi(\vec{r})$ given in Eq. 3.14 can be generated. It should be noticed that in this process, we introduce a random phase ϕ_i which is uniformly distributed over $[0, 2\pi)$. In fact, by this way we approximate the lost phase information of the structure during SANS experiments. Since the systems we are studying are known to

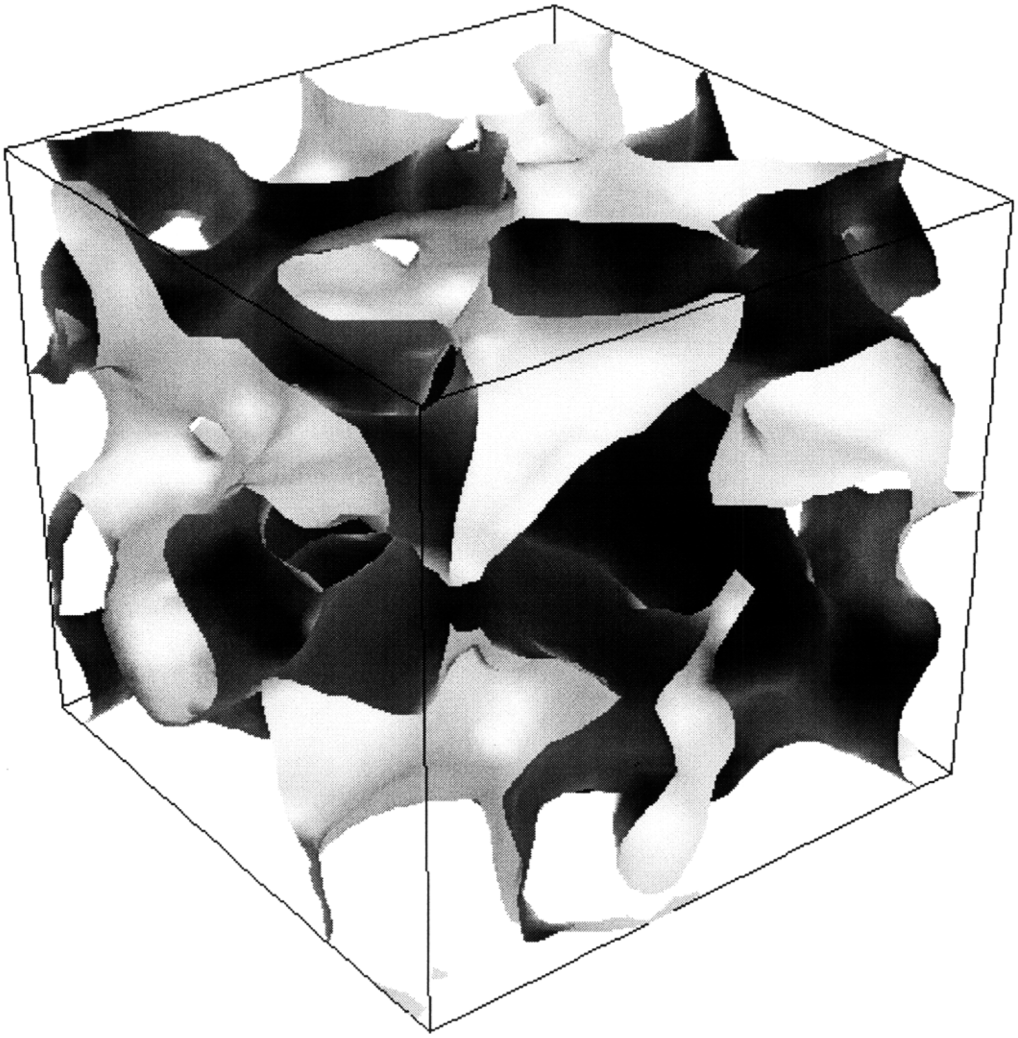

Figure 3-5: 3D simulation of a bicontinuous microemulsion. $d = 200\text{Å}$, $\xi = 100\text{Å}$, and $\delta = 20\text{Å}$. The size of box is $480 \times 480 \times 480\text{Å}^3$.

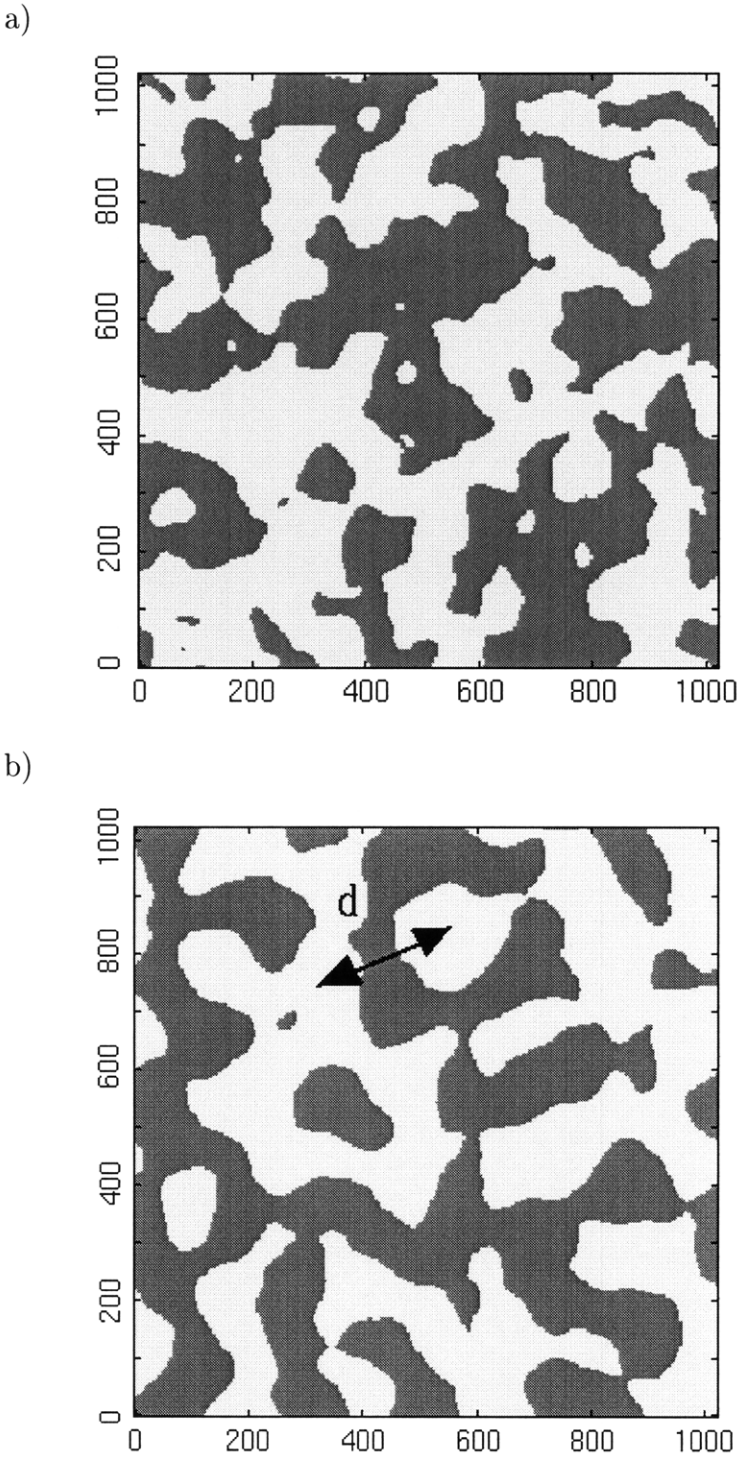

Figure 3-6: Cross sections of bicontinuous microemulsions. a) $\xi/d = 0.25$ and b) $\xi/d = 1.0$. In both cases, $d = 200$ Å and $\delta = 10$ Å. The axes are in the unit of Å.

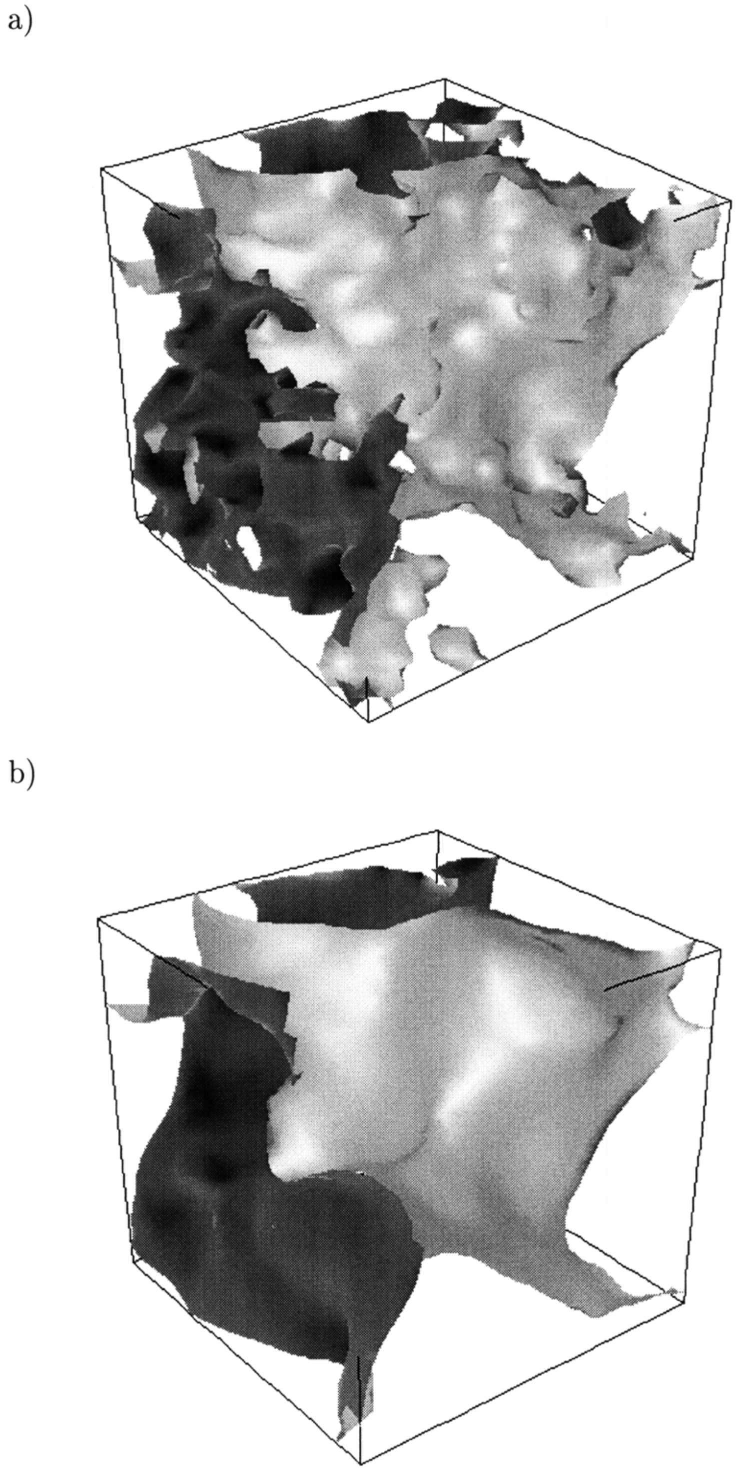

Figure 3-7: Effect of δ on the roughness of interface. a) $\delta = 2\mathring{A}$ and b) $\delta = 16\mathring{A}$. In both cases, $d = 200\text{Å}$ and $\xi = 100\text{Å}$. The size of boxes is $240 \times 240 \times 240$ Å^3.

be very disordered, the assumption of random phase is a good approximation. Using Eq. 3.18, the Gaussian random field $\Psi(\vec{r})$ is then clipped into a discrete random field $\zeta(\vec{r})$. Following the points where the discrete random field change its value, we can identify the interfaces between water and oil.

One example of a three dimensional simulation of a bicontinuous microemulsion using the CRW model is shown in Figure 3-5. In this simulation, representative values of the three length scales which are used, are the same order of magnitude as the values determined from SANS experiments : $d = 200\text{Å}$, $\xi = 100\text{Å}$, and $\delta = 20\text{Å}$. The surfaces are colored in bright and dark shades. The bright side of the surface faces oil and the dark side water. In fact, the surfaces are all connected, i.e. a single surface, resulting in a true bicontinuous structure.

To visually illustrate the physical meaning of the three basic length scales, a few test simulations were performed. Figure 3-6 describes the meaning of d and the effects of the order parameter ξ/d on the structure. The brighter part is oil and the darker part is water. First of all we can clearly see that the local order rapidly disappears as we move radially from one point. If we average the radial correlation functions in all direction it becomes the Debye correlation function. Therefore, the Debye correlations for this kind of structure decay rapidly as it was shown in Figure 3-2. As the order parameter changes from 0.25 to 1.0, the structure becomes less disordered.

Figure 3-7 shows the effects of δ on the roughness of surface. The front part of the images were removed to see the interfaces more clearly. While the large scale structures are the same in both cases, the roughness of the surface is changed dramatically by δ. This clearly verifies our definition of the surface roughness parameter δ.

Chapter 4

Isometric Microemulsions

Two component systems with symmetric volume fractions $\phi_1 = \phi_2$ are called isometric systems. As was discussed in Chapter 1, the bicontinuous structure favors isometric composition. For this reason, research on the bicontinuous structure is often made with isometric compositions. In this chapter, SANS measurements of the interfacial curvatures in isometric microemulsions made of an ionic surfactant called AOT (sodium-bis-ethylhexylsulpho-succinate), water and decane[64, 65] are presented.

4.1 Phase Behavior of Isometric AOT/water/H-decane System

The three component system of AOT/water/H-decane can easily form microemulsions in the vicinity of room temperature at a wide range of compositions[66, 67]. It has been shown, however, that the pure ternary system forms a water-in-oil droplet microemulsion only at room temperature because of the preferential curvature of the surfactant film toward water [68]. Thus the pure ternary system normally does not form a bicontinuous structure. In order to realize a bicontinuous structure in this system one needs to add small amounts of salt [69, 70], which means that one can control the hydrophilicity of the ionic surfactant with salt[67, 71]. For simplicity , the phase prism of an isometric microemulsion system is often projected onto the

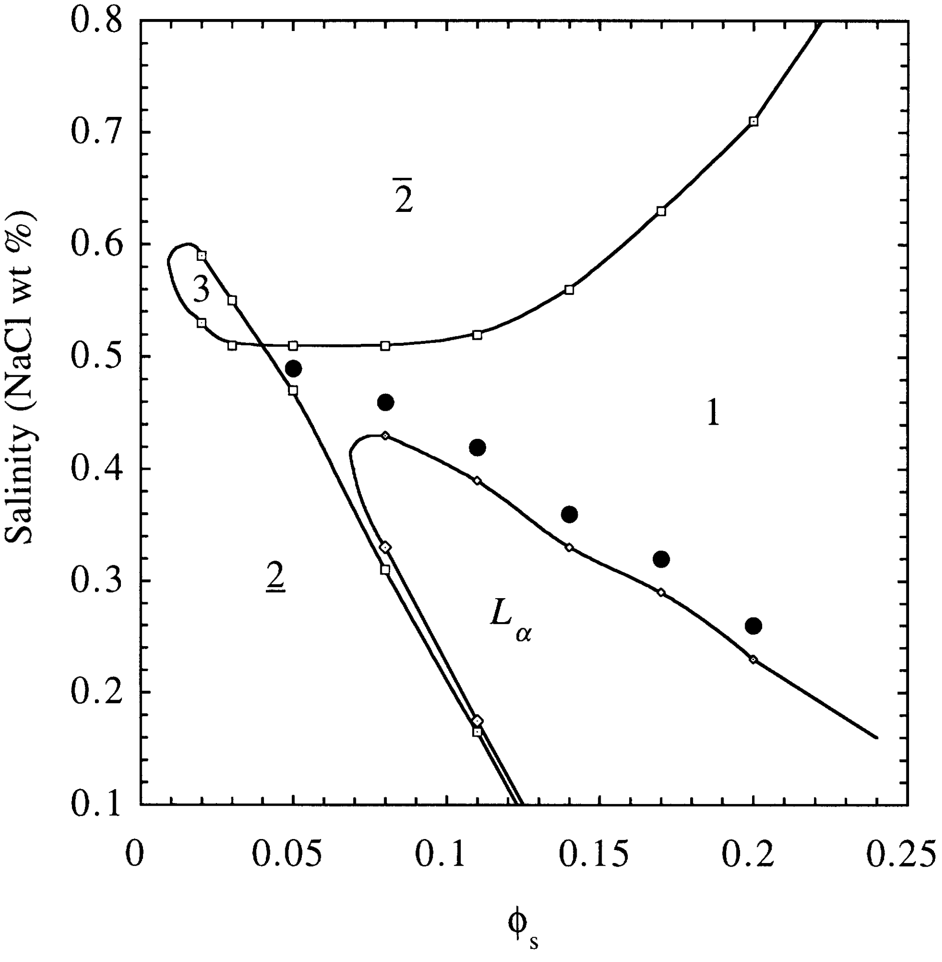

Figure 4-1: Phase diagram of isometric AOT/D_2O/decane system

temperature-surfactant volume fraction plane. In the case of the AOT based microemulsion system, however, one can also represent the phase diagram equally well in the salinity-surfactant volume fraction plane if one chooses a temperature close to but above the HLB (hydrophilic-lipophilic balanced) temperature of the system. The physical reason for this is that the spontaneous curvature of the AOT monolayer at the oil-water interface can be varied continuously by either changing temperature at fixed salinity or by changing salinity at fixed temperature. The hydrophilicity of an AOT molecule increases with increasing temperature but diminishes upon higher salinity.

Figure 4-1 shows the phase diagram of an isometric AOT/D_2O(NaCl)/H-decane system in the salinity-surfactant volume fraction plane at a temperature of 45 °C. The phase diagram was prepared for bulk contrast SANS experiments in which we match the scattering length density of decane with that of the hydrocarbon tail of AOT. From the neutron scattering point of view, we reduce the three-component system into a two- component system by contrast matching. The volume fraction of D_2O plus the head group of AOT was maintained at 0.5 for all surfactant volume fractions, i.e. $\phi_1 = \phi_{D_2O} + \beta\phi_s = 0.5$ and $\phi_2 = \phi_{decane} + (1-\beta)\,\phi_s = 0.5$. β is the volume fraction of head group in AOT and was taken to be 0.1064 [56]. In this regard, the contrast matched AOT/D_2O/decane system is a pseudo two-component isometric system.

For small surfactant volume fractions, less than 0.04, and low salinity, the system shows a $\underline{2}$ phase with an excess oil layer on top and an oil-in-water microemulsion at bottom. As salinity increases, the system goes through a three phase region, where a middle-phase microemulsion is in coexistence with an excess oil layer on top and an excess water layer on bottom, and at high salinity it transforms to a phase with an excess water layer on bottom and a water-in-oil microemulsion on top. For surfactant volume fractions larger than 0.035, as salinity increases, the system transforms from $\underline{2}$ phase to $\bar{2}$ phase through a 1 phase intermediate region. In the lower part of the 1 phase channel, one finds a region of lamellar phase, the salinity interval which it spans increases with increasing volume fraction of AOT. It should be noted from this phase diagram that the microstructure of the microemulsion inverts from an oil-in-water structure at low salinity to a water-in-oil structure at high salinity at fixed composition. It is thus expected that somewhere in the middle of the one phase region there should exist a series of disordered bicontinuous microemulsions with zero mean curvature[72]. In the phase diagram, we indicate by solid circles the locii where the zero mean curvature microemulsions may be found.

4.2 SANS Experiments

In SANS measurements, a suitable mixture of H-decane (94.99 wt%) and D-decane (5.01 wt%) was used to match the scattering length density of decane with that of the hydrocarbon tail of AOT (-0.1845×10^{10} cm^{-2}). H-decane (purity $>$ 98 %), D-decane(purity $>$ 98 %) and AOT (purity $>$ 99 %) were purchased from Fluka and D_2O (purity $>$ 99.9 %) from Cambridge Isotope and used as purchased.

The SANS measurements were performed at 45 °C for the points indicated as solid circles in the phase diagram. The points along the boundary between the one-phase and the lamellar phase are to measure the average Gaussian curvature and the average square mean curvature as a function of surfactant volume fraction. Since the average mean curvature of the lamellar phase is known to be zero, the average mean curvature at the points close to the lamellar phase are expected to be very close to zero. The points at with different salinity are to measure the average Gaussian curvature and the average square mean curvature.

The small-angle neutron diffractometer(SAND) at IPNS in Argonne National Laboratory was used in the measurements. The SAND uses a spallation neutron source generated by a 500 MeV H-accelerator. After moderation we have a pulse of white neutron beam with an effective wave length range from 1 to 14 Å. In SAND, all these neutrons are utilized by encoding their individual time-of-flight and their scattering angles are determined by their detected position on a 2D area detector. The 2D area detector has an active area of 40×40 cm^2 and the sample to detector distance is 2 m. This configuration allows a maximum scattering angle of about 9°. The reliable Q-range covered in the measurements were from 0.004 to 0.4 Å^{-1}. The liquid samples were contained in a flat quartz cell with a 1 mm path length. The temperature of the sample was set by a circulating water bath to an accuracy of 0.1 °C. Measured intensities were corrected for background and empty cell contributions and normalized by a reference scattering intensity of 1 mm water at room temperature.

4.3 Data Analysis and Discussion

The scattering intensity in absolute scale obtained after the standard data normalization procedure contains about 10 % of uncertainty in calibration using 1 mm water. This may cause an unnecessary uncertainty in the determination of parameters d, ξ, and δ. This uncertainty factor, however, can be eliminated by normalizing the scattering intensity by the invariant calculated according to Eq. 2.27. In the calculation of the invariant, the interval of integration was divided into three parts, $0 < Q < Q_{min}$, $Q_{min} < Q < Q_{max}$, and $Q_{max} < Q$ where Q_{min} and Q_{max} are the minimum and maximum values of Q in the measurements. In the range, $Q_{min} < Q < Q_{max}$, the measured intensity was used for $I(Q)$. In the range,$0 < Q < Q_{min}$, it was assumed that $I(Q)$ is constant at $I\left(Q_{min}\right)$. Porod's law was assumed for the Q-range,$Q_{max} < Q$.

Figure 4-2 shows a representative SANS intensity of an isometric bicontinuous microemulsion. The flat tail at large Q in Figure 4-2 a) is background due to incoherent scattering. Since the structural information of the sample is contained only in coherent scattering, the background scattering has to be removed from the scattering intensity. To determine the background scattering correctly, the SANS measurement has to cover the Q-region large enough to see the flat background scattering. Figure 4-2 b) shows the intensities after background correction. This intensity is characterized by a broad peak at $Q = 0.03$ Å^{-1}, a Q^{-4} power law decay at large Q and the transition of decay power from $-n$ $(n > 4)$ to -4 around Q_{trans}. In fact all these features are related to the three basics length scales. The position of the peak is related to the inter-domain distance d as $2\pi/Q_{max}$ and the width ΔQ is inversely proportional to the coherence length ξ. The transition to Porod's region is controlled by the surface roughness parameter δ.

Figure 4-3 a) shows the scattering intensities measured at a series of points close to the 1 phase and lamellar phase boundary. We can clearly see that, as the surfactant volume fraction increases, the peak position shifts to higher Q and the peak becomes sharper. The physical meaning of this systematic change as a function of surfactant volume becomes clear after analyzing them with the CRW model.

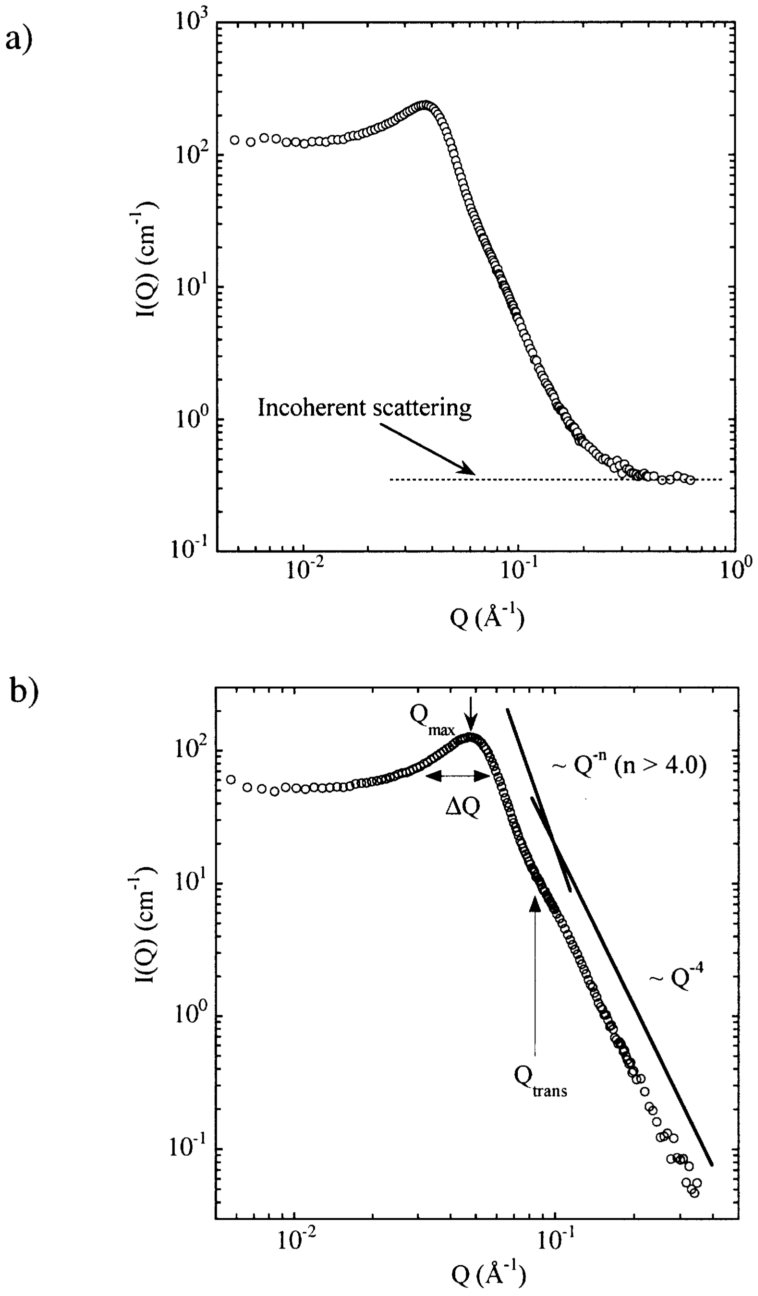

Figure 4-2: A representative SANS intensity from an isometric bicontinuous microemulsion, a) before background correction and b) after background correction.

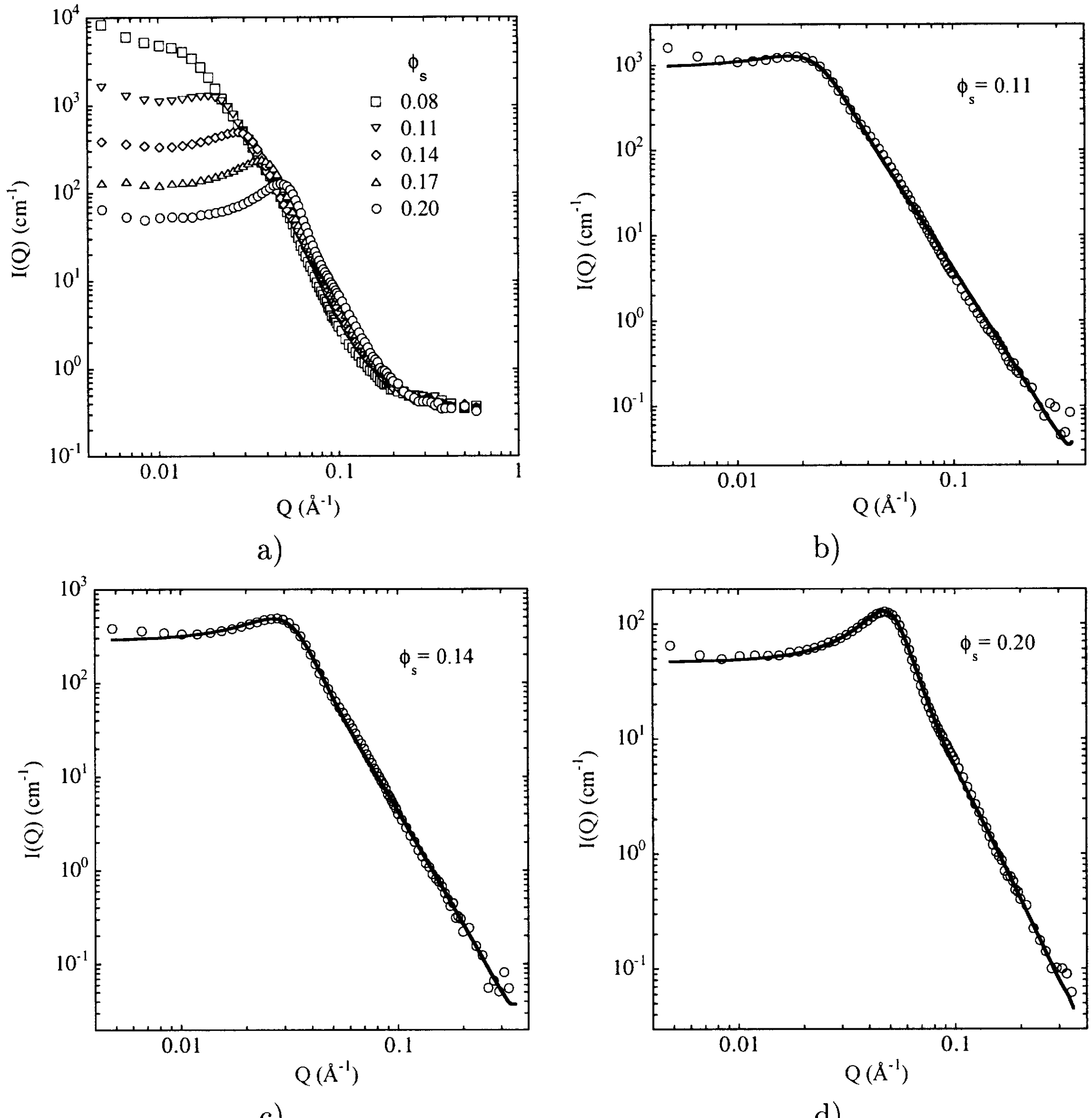

a) b) c) d)

Figure 4-3: The SANS intensities of isometric AOT/D_2O/decane and the CRW model as a function surfactant volume fraction. a) Raw data b)-d) three representative curves comparing the CRW model with the experimental data. Solid lines are the CRW model

ϕ_s	d (Å)	ξ (Å)	δ (Å)	ξ/d	$\langle K\rangle$ (10^{-4}Å^{-2})	$\langle H^2\rangle$ (10^{-4}Å^{-2})	$(S/V)_{RWM}$ (10^{-2}Å^{-1})	$(S/V)_{Porod}$ (10^{-2}Å^{-1})	bgd (cm^{-1})	$\langle \eta^2\rangle$ $(10^{21}cm^{-4})$
0.05	1025.0	90.6	58.5	0.088	-0.353	1.62	0.535	0.399	0.385	2.59
0.08	477.1	83.5	21.4	0.175	-1.165	6.35	0.972	0.913	0.384	1.31
0.11	293.7	89.3	11.0	0.304	-2.382	16.78	1.39	1.25	0.393	1.09
0.14	209.1	80.9	9.12	0.387	-3.610	21.65	1.71	1.70	0.382	0.93
0.17	159.5	74.3	6.54	0.466	-5.809	37.67	2.17	2.19	0.352	0.93
0.20	126.5	68.5	4.78	0.542	-8.943	64.85	2.69	2.56	0.321	0.90

Table 4.1: The fitted parameters of isometric AOT/D_2O/decane system

In Figure 4-3 b), c) and d), three representative SANS intensities at $\phi_s = 0.11$, 0.14 and 0.20 are compared with the theoretical fits using Eq. 3.35 and 3.25 in Eq. 3.1. The circles are experimental data and the solid lines are theoretical fits. These show a good agreement of the CRW model with the experimental data. The fitted parameters d, ξ, and δ are listed in Table 4.1. Using Eq. 3.30, 3.31, and 3.32, a, b, and c were converted into the inter-domain distance d, the coherence length ξ, and the surface persistence length δ. The variation of d, ξ, and δ as a function of surfactant volume fraction are shown in Figure 4-4. As the surfactant volume fraction increases d and δ decrease rapidly while ξ decreases slowly. This is because as the number of surfactant molecules increase, more surfaces are created per unit volume and therefore the inter-domain size d should decrease. The ratio ξ/d is a measure of the local order. Considering that the ratio ξ/d increases with the surfactant volume fraction, the bicontinuous microemulsion is most disordered at the fish tail, which is the point of the smallest surfactant volume fraction in the 1 phase region, and becomes more ordered as the surfactant volume fraction increases.

The average Gaussian and square mean curvatures are calculated by using Eq. 3.54 and Eq. 3.56 respectively with $\alpha = 0$. In this case, the average mean curvature in this isometric case is zero. Figure 4-5 shows the average Gaussian curvature as a function of ϕ_s. Here we should notice that $\langle K \rangle$ is negative in every point measured in this experiment. From this we can infer that the interfacial structure of the microemulsion under study is dominated by the saddle shape interface where the Gaussian curvature is negative. From the distribution of $\langle K \rangle$ as a function of ϕ_s we can clearly see the parabolic dependence. This parabolic dependence can be explained by the following arguments. For an isometric case, $\alpha = 0$, thus the specific interface given in Eq. 3.28 reduces to

$$\left(\frac{S}{V}\right) = \frac{2}{\sqrt{3}\pi}\sqrt{\langle k^2 \rangle}. \tag{4.1}$$

If all the surfactant molecules reside at the interfaces, it can be shown that (add one more line to derive this)

$$\left(\frac{S}{V}\right) = \frac{\phi_s}{\Delta} \tag{4.2}$$

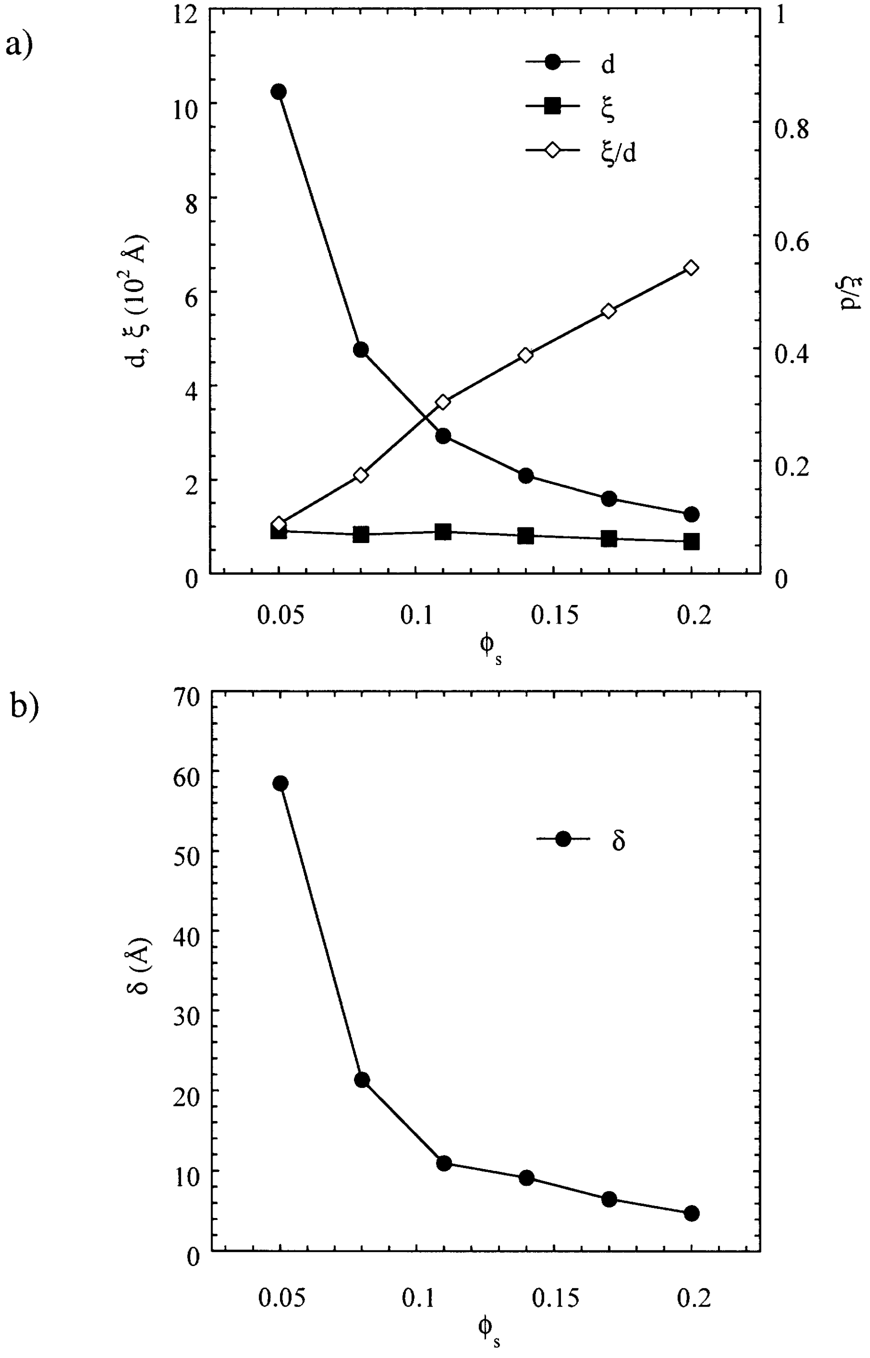

Figure 4-4: The three basics length scales in isometric AOT/D_2O(NaCl)/decane system as a function of ϕ_s. a)d, ξ, and ξ/d, and b)δ.

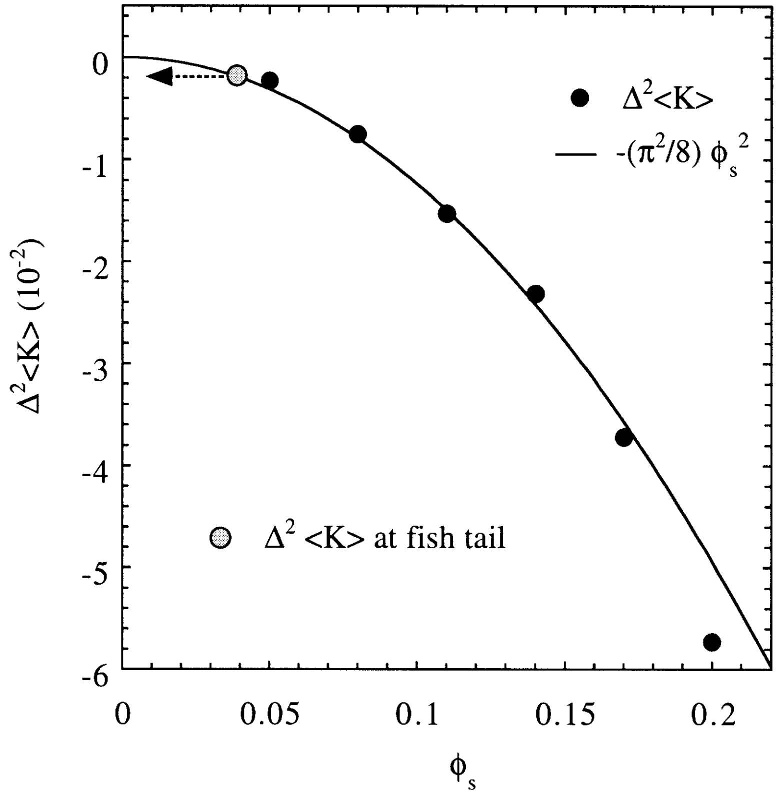

Figure 4-5: The average Gaussian curvature of isometric AOT/D_2O/decane system. The Gaussian curvature is multiplied by Δ^2.

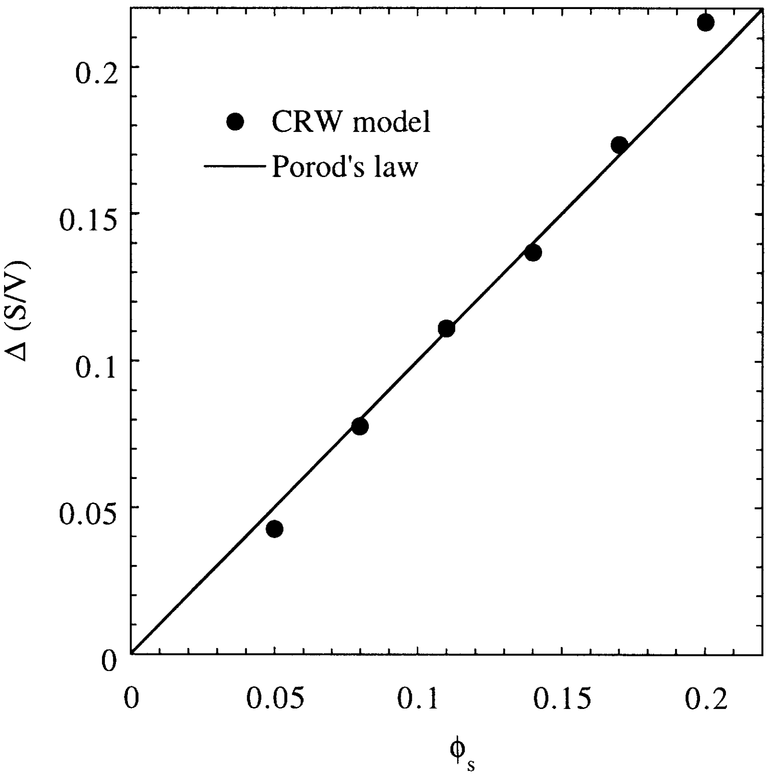

Figure 4-6: The specific interface of isometric AOT/D_2O/decane system. The specific interface is multiplied by Δ.

where Δ is the effective chain length of the surfactant. Since the average Gaussian curvature in an isometric system is proportional to $\langle k^2 \rangle$ by Eq. 3.52, using Eq. 4.1 and 4.2 with Eq. 3.52, we obtain a scaling relation

$$\Delta^2 \langle K \rangle = -\left(\frac{\pi^2}{8}\right) \phi_s^2. \tag{4.3}$$

After determining Δ independently from Porod's law, the scaled Gaussian curvature, $\Delta^2 \langle K \rangle$, is displayed against the scaling relationship given above. The Δ of AOT used in this graph is 8 Å which is an average value obtained from the six data points. It is remarkable that the experimental results and the theoretical expectation show a good agreement. This tells us that the interfacial curvature measurements from SANS intensity using the CRW model is a consistent and reliable procedure.

Using Eq. 4.1, the specific interfaces were calculated and, after multiplication by

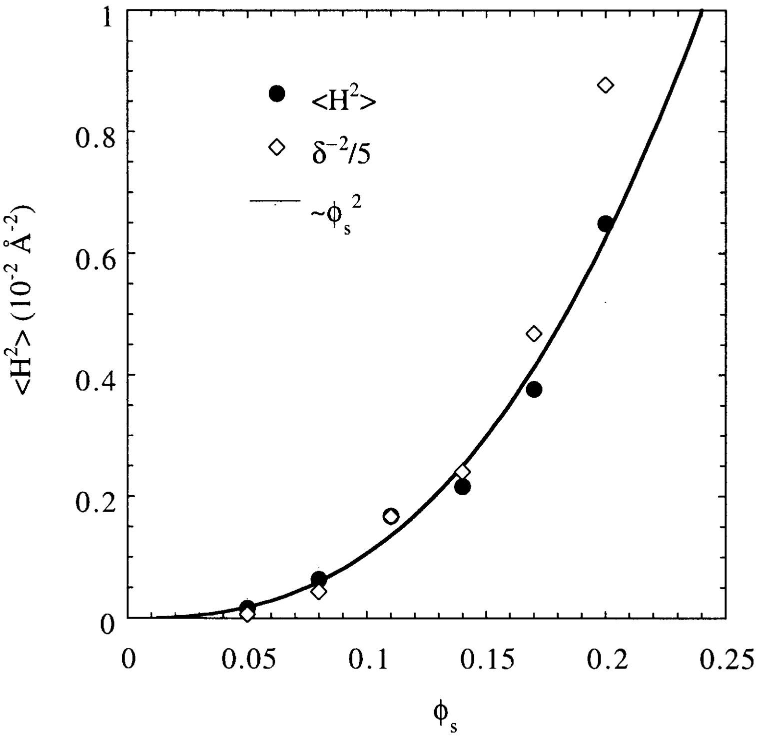

Figure 4-7: The average square mean curvature of isometric AOT/D_2O/decane system. Solid line is a parabolic guide line.

Δ, compared with those estimated by Porod's law. As we can see in Figure 4-6, both agree each other very well. This can be considered as another evidence of the validity of our method for extracting the interfacial curvatures. Since the Porod's law uses only large Q data, when the large Q data is poor in statistics or insufficient, the specific interface estimated by the Porod's law often contains large uncertainties. In this sense, the specific interface measurement using the CRW model which uses the SANS intensity over the whole Q range is suggested as an alternative to the Porod's law.

Figure 4-7 shows the average square mean curvature $\langle H^2 \rangle$ calculated by Eq. 3.56 and plotted as a function of ϕ_s. While, according to Gauss-Bonnet theorem, $\langle K \rangle$ is a topological invariant only related to the number of holes per unit interfacial area, $\langle H^2 \rangle$ is the fluctuation of the mean curvature and thus related to the persistence length of the interface. In the limiting case where the parameter c is much larger than a and

b, which is often the case of disordered bicontinuous microemulsions, it can be shown that $\langle H^2 \rangle$ is reduced to $(\delta^{-2}/5)$. Points are also shown for $(\delta^{-2}/5)$. Both agree fairly well and this confirms the physical meaning of the third length scale, δ, as a surface roughness parameter.

4.4 Two- and Three-Dimensional Simulations

Using the parameters determined from SANS experiments, we generated a series of three dimensional structures. For visual simplicity, cross sections of those images are presented in Figure 4-8. As we can see clearly, as the surfactant volume fraction increases, the inter-domain distance increases correspondingly. Also, the system becomes less disordered. One full three-dimensional simulation of an isometric AOT/D^2O/decane system at $\phi_s = 0.08$ is shown in Figure 4-9. As we can see here the surfaces are all connected and therefore the structure is bicontinuous. We should also notice that there are many holes within the structure and the interfaces are dominated by saddle points. This consistent with the negative average Gaussian curvature measured.

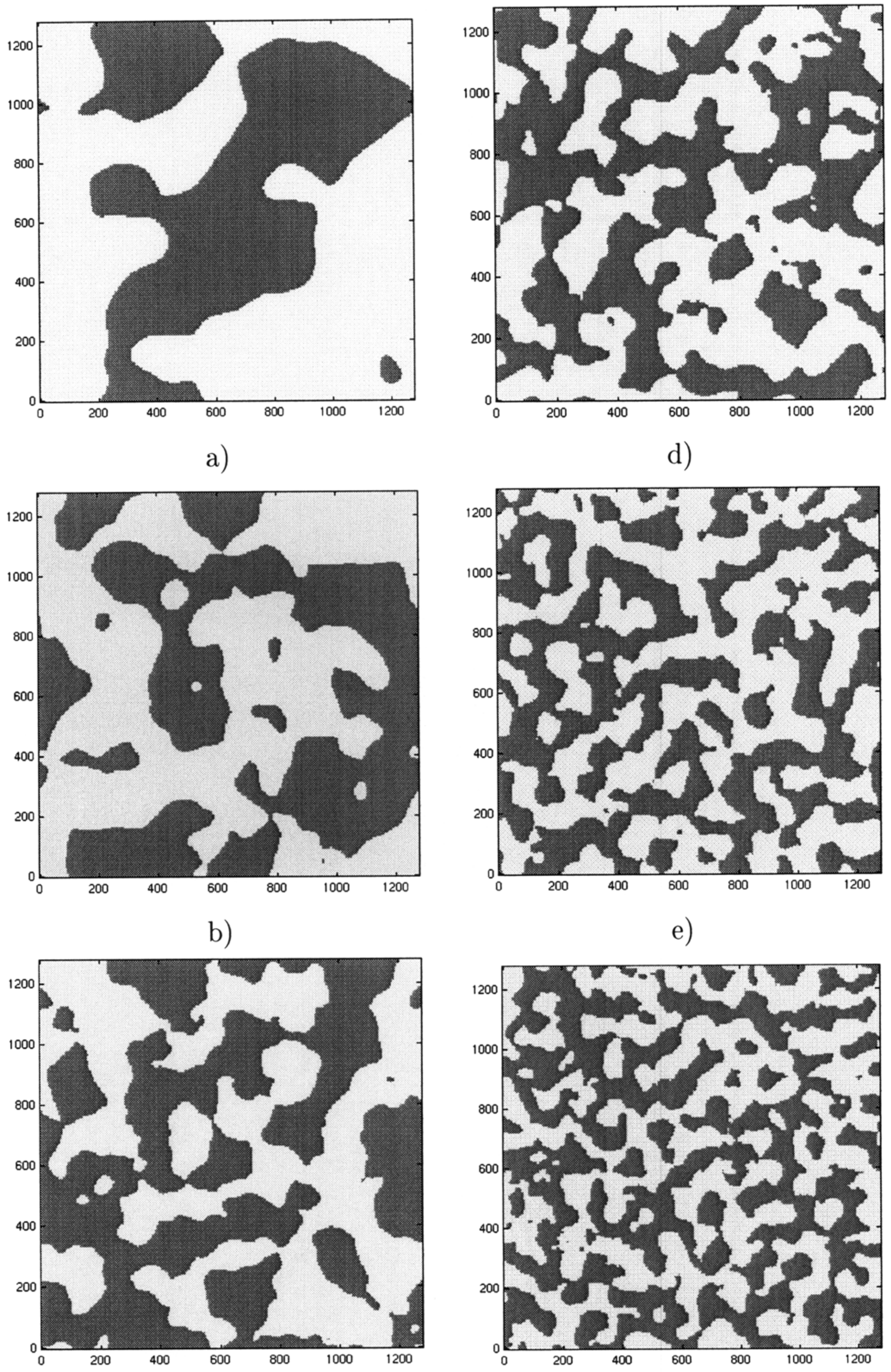

a) d) b) e) c) f)

Figure 4-8: 2D simulations of isometric AOT/D_2O/decane system. a) $\phi_s = 0.05$, b) 0.08, c) 0.11, d) 0.14, e) 0.17, and f) 0.20. The axes are in the unit of Å

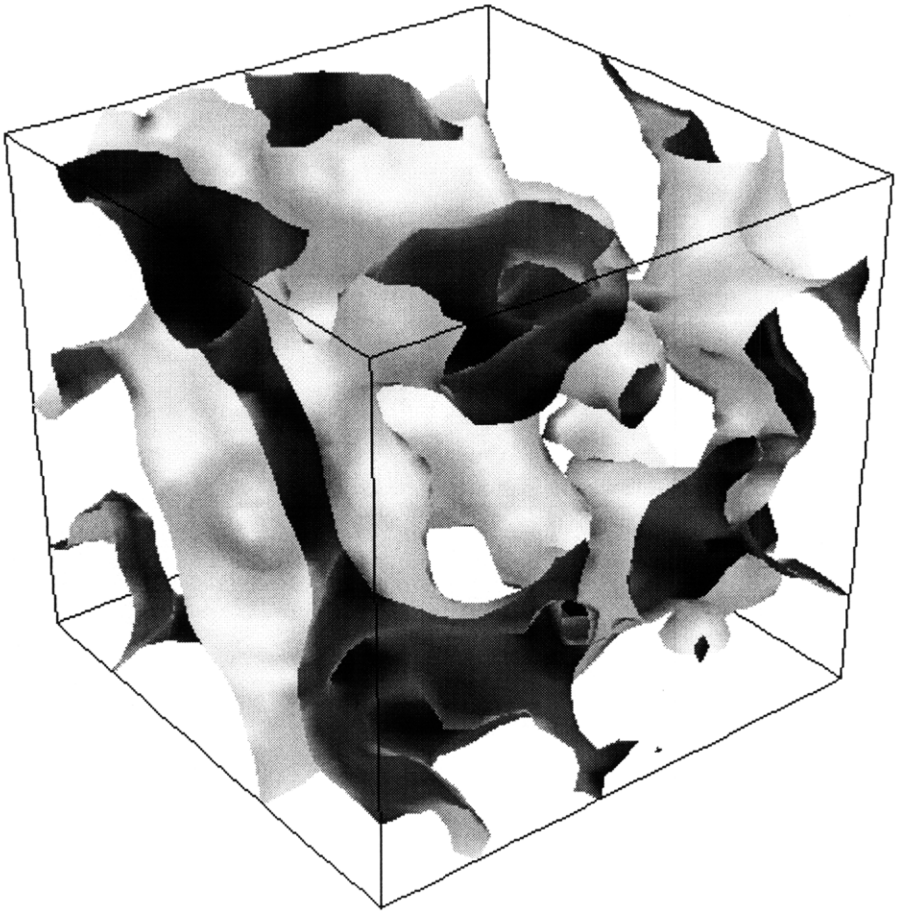

Figure 4-9: 3D simulation of an isometric AOT/D_2O/decane system. The surfactant volume fraction is $\phi_s = 0.08$ and the three length scales are $d = 477.1$ Å, $\xi = 83.5$ Å and $\delta = 21.4$ Å. The size of box is 600 x 600 x 600 $Å^3$.

Chapter 5

Non-Isometric Microemulsions

The two component porous materials of asymmetric compositions, $\phi_1 \neq \phi_2$, are called non-isometric systems. Since many of the porous materials in widespread use are non-isometric, it is important to be able to characterize their interfacial structures. Microemulsions can be prepared in such a way that the volume fractions of the watery and oily regions are not equal[73], which are called non-isometric microemulsions. Depending on the asymmetry of the composition, temperature and so on, the systems show various phase behavior with corresponding characteristic internal structures. In this chapter, SANS studies of two non-isometric microemulsions are presented. The first one is a non-ionic microemulsion made of $C_{10}E_4/D_2O$/H-octane and the second one is an ionic microemulsion made of AOT/D_2O(NaCl)/H-decane. Using the CRW model with a non-zero clipping level α, the SANS intensities at various points in the 1 phase channel were analyzed to extract the average interfacial curvatures and identify the interfacial structures[74]. The 3D simulations were generated to confirm the structures inferred from the curvature information and provide further insights.

5.1 Phase Behavior of Non-Isometric Microemulsions

Figure 5-1 shows the phase diagram of non-isometric $C_{10}E_4/D_2O$/H-octane system on a $T - \Delta\phi_1$ plane. $C_{10}E_4$ (Fluka, > 97 %), D_2O (Cambridge Isotope Laboratory, > 99.9 %), and H-octane (Fluka, > 99.5 %) were used. In this phase diagram, the surfactant volume fraction was kept constant at 0.13. The volume fraction of the watery region which includes water and the head group of the surfactant is denoted by ϕ_1 and that of the oily region which includes oil and the tail of the surfactant by ϕ_2,

$$\phi_1 = \phi_w + \beta\phi_s \tag{5.1}$$

$$\phi_2 = \phi_o + (1-\beta)\,\phi_s \tag{5.2}$$

where β is the volume fraction of the head group in a surfactant molecule. The degree of non-isometry, $\Delta\phi_1$, which measures how far away the system is from isometry ($\phi_1 = \phi_2 = 0.5$), is defined as

$$\Delta\phi_1 = \phi_1 - 0.5 \tag{5.3}$$

where a positive $\Delta\phi_1$ means a water-rich composition and a negative $\Delta\phi_1$ an oil-rich composition. In the non-isometric $C_{10}E_4/D_2O$/H-octane system, the phase behavior is rather symmetric about $\Delta\phi_1 = 0$. This is caused by the well balanced sizes of the head and tail groups of the surfactant $C_{10}E_4$ as well as their balanced soulibility in water and oil. This effect becomes clear if we consider the asymmetric phase diagram of an ionic microemulsion made of AOT/D_2O(NaCl)/H-decane where AOT is a surfactant molecule with a much smaller head than its tail. When it is isometric or close to isometric, the non-ionic microemulsion goes through a rather simple phase transitions with temperature as following,

$$\underline{2} \text{ phase} \rightarrow 1 \text{ phase} \rightarrow \bar{2} \text{ phase}.$$

When it is very oil-rich or very water-rich, however, the phase transitions take more steps including a lamellar phase between the two 1 phases,

$$\underline{2} \text{ phase} \rightarrow 1 \text{ phase} \rightarrow L_\alpha \text{ phase} \rightarrow 1 \text{ phase} \rightarrow \bar{2} \text{ phase.}$$

Figure 5-2 shows phase diagram of non-isometric AOT/D_2O(NaCl=0.4 wt%)/H-decane system on a $T - \Delta\phi_1$ plane. AOT(Fluka, > 99 %), D_2O (Cambridge Isotope Laboratory, > 99.9 %), and H-decane (Fluka, > 98 %) were used. While the volume fraction of AOT was maintained at 0.112, the volume fractions of water and oil were varied. The salinity in water was 0.4 wt %. When $\Delta\phi_1$ is very negative, as the temperature increases, the microemulsion goes through a series of phase transition as shown,

$$\bar{2} \text{ phase} \rightarrow 1 \text{ phase} \rightarrow \underline{2} \text{ phase.}$$

However, when $\Delta\phi_1$ is positive, the phase transitions as temperature increases goes through a Lamellar phase,

$$\bar{2} \text{ phase} \rightarrow 1 \text{ phase} \rightarrow L_\alpha \text{ phase} \rightarrow 1 \text{ phase} \rightarrow \underline{2} \text{ phase.}$$

While the non-ionic microemulsion exhibits a phase behavior symmetric about $\Delta\phi_1$, the ionic microemulsion shows a asymmetric phase behavior. This difference in the phase behavior may be caused by the difference in the symmetry of the head and tail group of surfactant molecules. While the non-ionic surfactant has a symetric head and tail in size as well as the amphiphilicity, the ionic surfactant has a non-symetric head and tail (a very small head compared to its tail). In the non-ionic microemulsion the $\underline{2}$ phase is located at the lower temperature region with the $\bar{2}$ phase at the higher temperature region but in the ionic microemulsion, their locations are reversed. This is due to the opposite temperature dependence of the hydrophilicity (or hydrophobicity) of non-ionic and ionic surfactants. As the temperature increases, the non-ionic surfactant becomes less hydrophilic while the ionic surfactant becomes more hydrophilic.

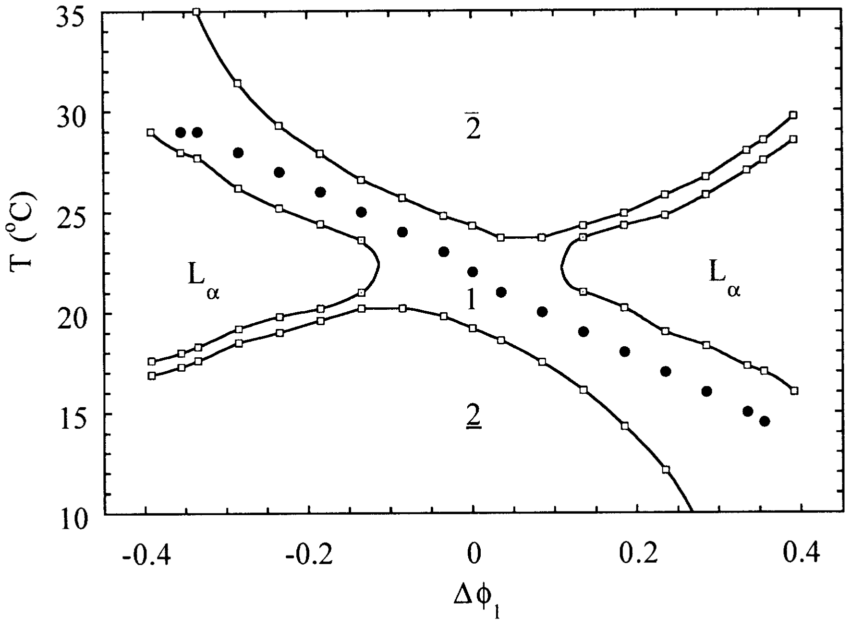

Figure 5-1: Phase diagram of non-isometric $C_{10}E_4/D_2O$/decane system. The surfactant volume fraction was kept constant at 0.13.

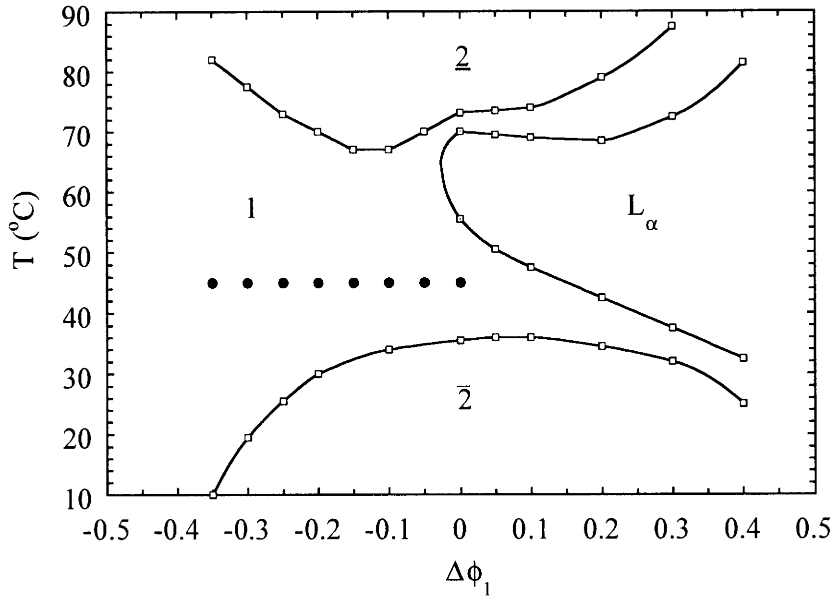

Figure 5-2: Phase diagram of non-isometric AOT/D_2O/decane system. The surfactant volume fraction was kept at 0.112.

5.2 SANS Experiments

We are interested in the structural transformation within the 1 phase region as the microemulsions move away from isometry. For this purpose, a series of SANS experiments were performed to measure the average Gaussian, mean, and square mean curvatures. The points where the SANS intensities were measured are denoted by solid circles in Figure 5-1 and 5-2. In the ionic microemulsion, only the oil rich region where the 1 phase region has a wide temperature gap was investigated. In the non-ionic microemulsion, however, both the water-rich and oil-rich regions were explored. The samples for this set of experiments were prepared in such a way that we realize the pseudo two component systems in a similar way as the isometric systems discussed in Chapter 4. In the ionic system, the temperature was maintained at 45 °C for all the samples and in the non-ionic case, the temperature was changed for each sample as indicated in the phase diagram. For both systems, the SANS experiments were performed at the small-angle neutron diffractometer(SAND) at IPNS in Argonne National Laboratory. The configuration of SAND was the same as described in Chapter 4.

5.3 Three Length Scales and Interfacial Curvatures

5.3.1 Non-Isometric Non-Ionic Microemulsions

The SANS intensities of non-isometric $C_{10}E_4/D_2O$/octane system without background correction are shown in Figure 5-3 a) and b) where a) shows $\Delta\phi_1 \leq 0$ (oil-rich side) and b) $\Delta\phi_1 \geq 0$ (water-rich side). It is interesting to note that as $\Delta\phi_1$ moves away from zero, the scattering intensities vary in a symmetric way about $\Delta\phi_1 = 0$. As the system moves away from $\Delta\phi_1 = 0$ in both positive and negative directions, the peak positions of the intensities shift toward large Q. The intensities at large Q where the Porod's law is applied, however, overlap each other. Since the specific interfacial area is proportional to the coefficient of Porod's law decay, the specific interfacial areas in all the samples studied here are about the same. This is natural because we kept the volume faction of surfactants (which constitute the interfacial monolayer) same in all the samples. The effect of the surfactant volume fraction on the specific interfacial area becomes more clear if we compare the scattering intensities in Fig 5-3 with those in Fig. 4-3 where the scattering intensities at Porod's regime increase with ϕ_s.

Now the question is how the non-isometric microemulsions with similar specific interfacial areas evolve in structure with the degree of non-isometry. For this purpose we analyzed the SANS intensities of the non-isometric microemulsions by the CRW model with a non-zero clipping level α. Using Eq. 3.20 and $\langle \zeta \rangle = \phi_1$, the volume fraction of watery region ϕ_1 can be expressed in terms of α as following,

$$\phi_1 = \frac{1}{2}\left(1 - \text{erf}\left(\frac{\alpha}{\sqrt{2}}\right)\right). \tag{5.4}$$

The clipping level α of each sample is determined by this relation. In this analysis, we use the spectral density function $f(k)$ given in Eq. 3.29. For the Debye correlation function, we used the full integral form given in Eq. 3.22 rather than the simple expression given in Eq. 3.25 which was used for the isometric system.

The SANS intensities were analyzed using the CRW model and the representative plots comparing the SANS experiments (symbols) and the CRW model (solid lines) are presented in Figure 5-4. It is clearly seen that the model agrees with the experiments very well as it does in the isometric case. Using the parameters a, b, and c acquired in this analysis, the average Gaussian, mean, and square mean curvatures are calculated by Eq. 3.54, 3.55, and 3.56. All the fitted and calculated values are listed in Table 5.1.

Figure 5-5 a) shows d, ξ, and ξ/d as a function of $\Delta\phi_1$. As $\Delta\phi_1$ moves away from zero, d decreases from 260 Å to about 150 Å in a symmetric fashion. Similarly ξ also decreases from 125 Å to 40 (at $\Delta\phi_1$ = -0.35) and to 65 Å (at $\Delta\phi_1$ = 0.35), more rapidly in the oil-rich direction than in the water-rich direction. The local orderness ξ/d is determined by these two parameters. While ξ/d decreases from 0.45 to 0.25

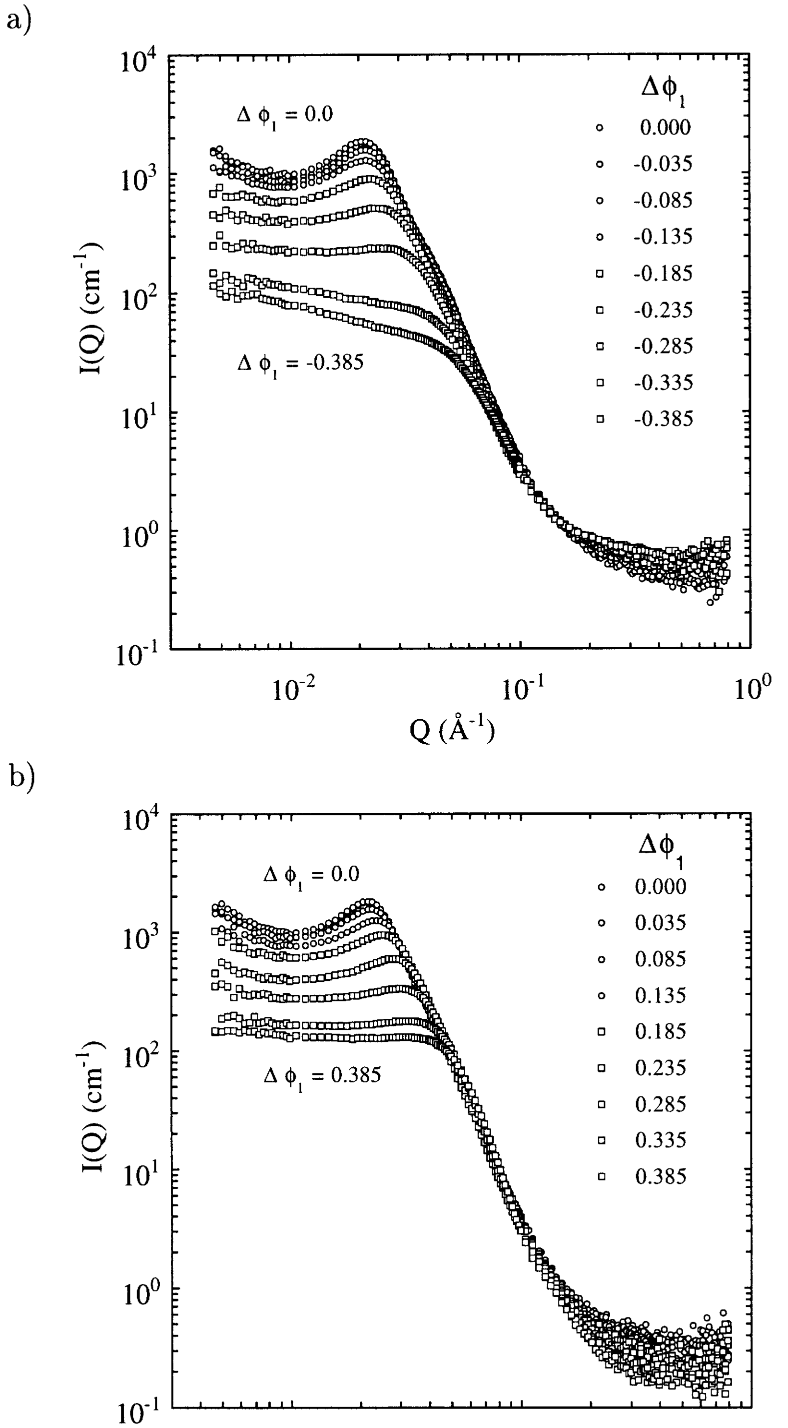

Figure 5-3: SANS intensities of non-isometric $C_{10}E_4/D_2O$/octane system. a) $\Delta\phi_1 \leq 0$ and b) $\Delta\phi_1 \geq 0$

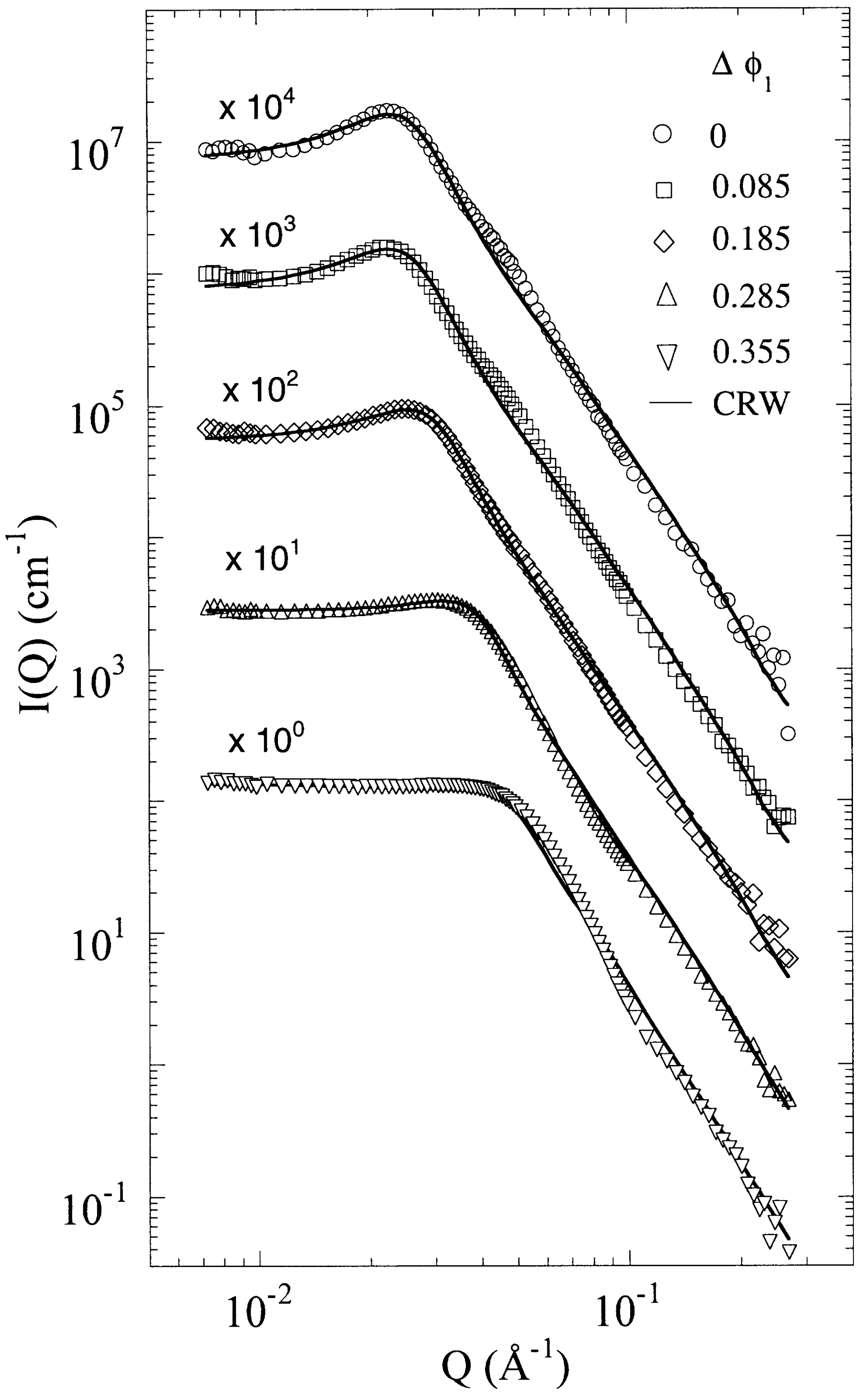

Figure 5-4: Data analysis of non-isometric $C_{10}E_4/D_2O$/octane system

$\Delta\phi_1$	T_{exp} (^oC)	α	d (Å)	ξ (Å)	δ (Å)	ξ/d	$\langle K\rangle$ (10^{-4}Å^{-2})	$\langle H\rangle$ (10^{-4}Å^{-1})	$\langle H^2\rangle$ (10^{-4}Å^{-2})	(S/V) (10^{-2}Å^{-1})	bgd (cm^{-1})	$\langle\eta^2\rangle$ ($10^{21}cm^{-4}$)
-0.355	29	1.058	135.3	26.2	11.8	0.194	0.939	263.0	37.4	1.300	0.650	0.388
-0.335	29	0.9741	149.6	37.1	12.6	0.248	-0.294	206.9	25.2	1.343	0.700	0.450
-0.285	28	0.7892	184.0	64.2	15.4	0.349	-1.227	126.2	12.0	1.189	0.670	0.611
-0.235	27	0.6280	218.8	84.4	14.9	0.386	-1.511	87.91	10.0	1.168	0.650	0.802
-0.185	26	0.4817	241.5	101.4	13.9	0.420	-1.673	63.00	9.8	1.183	0.610	1.016
-0.135	25	0.3451	260.6	111.1	13.4	0.426	-1.744	43.04	9.8	1.194	0.520	1.146
-0.085	24	0.2147	256.7	119.7	11.7	0.466	-2.006	27.59	12.0	1.276	0.520	1.280
-0.035	23	0.08784	275.3	124.7	11.3	0.453	-1.959	10.94	12.7	1.260	0.476	1.393
0.00	22	0.0000	257.6	124.1	10.4	0.482	-2.203	0.00	14.5	1.336	0.440	1.498
0.035	21	-0.0878	270.0	125.2	10.6	0.464	-2.076	-11.26	14.5	1.297	0.437	1.445
0.085	20	-0.2147	259.5	120.8	11.9	0.465	-1.952	-27.22	11.5	1.258	0.384	1.363
0.135	19	-0.3451	241.4	111.3	14.5	0.461	-1.793	-43.63	8.3	1.210	0.330	1.294
0.185	18	-0.4817	221.1	104.6	15.9	0.473	-1.665	-62.87	7.4	1.181	0.302	1.213
0.235	17	-0.6280	192.3	95.2	18.9	0.495	-1.460	-86.40	6.4	1.148	0.254	1.069
0.285	16	-0.7892	165.7	89.5	20.9	0.540	-1.078	-118.2	6.9	1.115	0.223	0.893
0.335	15	-0.9741	139.6	78.6	21.8	0.563	-0.185	-164.1	8.8	1.065	0.202	0.759
0.355	14	-1.058	131.5	65.2	20.7	0.495	0.493	-190.5	11.4	1.045	0.184	0.661

Table 5.1: The fitted parameters of non-isometric $C_{10}E_4/D_2O$/octane system

in the oil-rich direction, it increases to 0.56 in the water-rich direction. Considering that ξ/d is far less than 1 in all cases, the systems have very disordered interfacial structures. The surface roughness parameter δ is shown in Figure 5-5 b). The δ increases in both the oil-rich and water-rich directions, from 10 Å to 15 Å in the oil-rich direction and from 10 Å to 22 Å in the water-rich direction. Considering that δ is proportional to the surface persistence length, we can infer that the interface in the water-rich region is more smooth and rigid. This is consistent with the fact that ξ/d in the water-rich region is larger than that in the oil-rich region.

The average Gaussian curvature as a function of $\Delta\phi_1$ is shown in Figure 5-6 a). The solid circles are the measured values and the solid line is a theory predicted by the CRW model which is given as

$$\langle K \rangle = \frac{\pi^2}{8} e^{\alpha^2} \left(\alpha^2 - 1\right) \left(\frac{\phi_s}{\Delta}\right)^2 \tag{5.5}$$

where Δ is an effective chain length of a surfactant molecule. This relation is obtained from Eq. 3.28, Eq. 3.52, and Eq. 4.2. In this plot we used an average value of Δ measured by an independent analysis of the SANS intensities by the Porod's law at large Q region. As $\Delta\phi_1$ moves away from zero, meaning that the system becomes more non-isometric, the average Gaussian curvature $\langle K \rangle$ becomes less negative and eventually change its sign to positive. As discussed in Chapter 3, the Gaussian curvature is negative at saddle shaped interfaces and positive at concave or convex interfaces. According to Gauss-Bonnet theorem, when averaged over a whole closed surface, $\langle K \rangle$ is proportional to the number of holes per unit surface area. The $\langle K \rangle$ is positive when there is no hole on the surface, zero when there is only one hole, negative when more than one hole. For smooth surfaces, it requires more saddle shaped interfaces to have more holes per unit area. The negative average Gaussian curvature around isometric composition, therefore, means that the interfacial structure is dominated by saddle points with many interpenetrating holes. $\langle K \rangle$ change its sign from negative to positive at around $\Delta\phi_1 = 0.34$. Since positive average Gaussian curvature means isolated interfaces with no holes such as spheres, we can infer that as the system be-

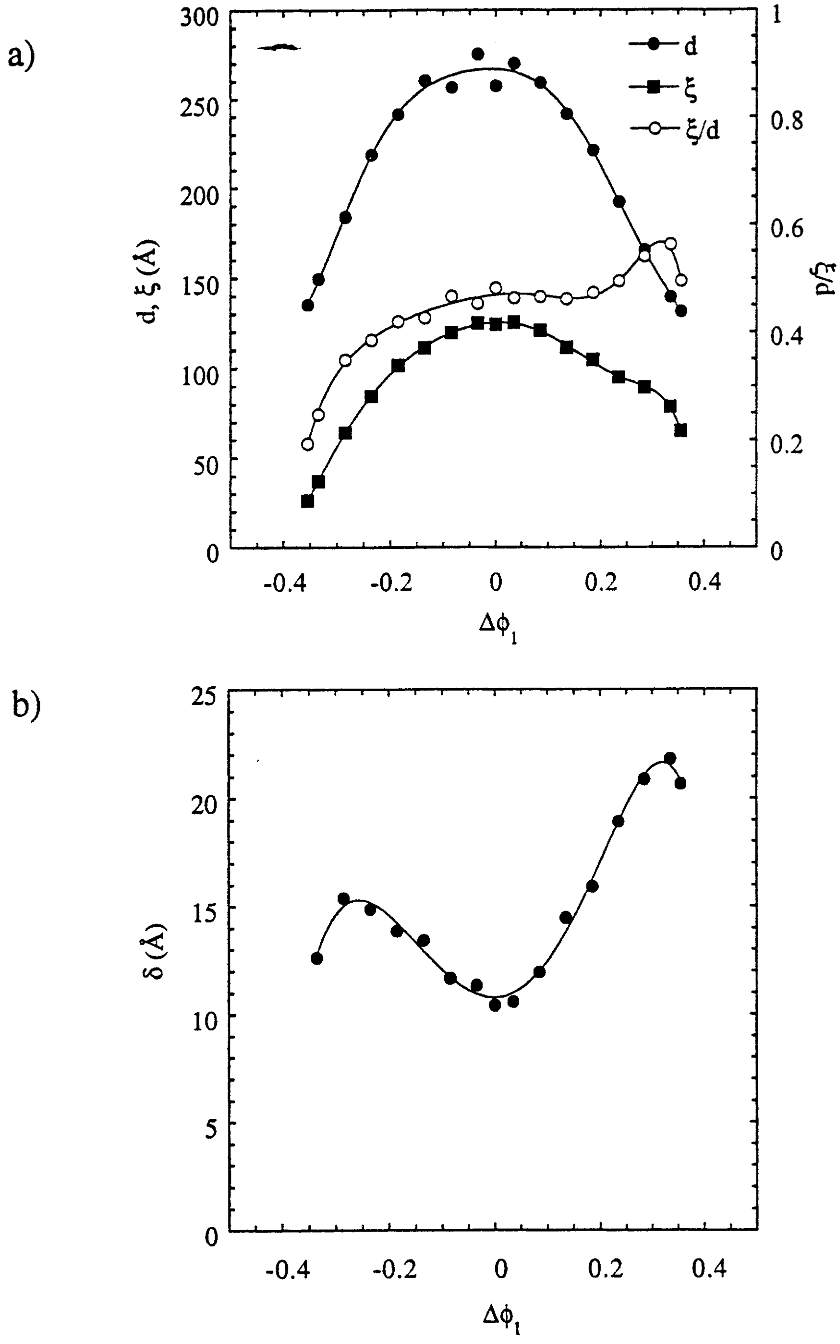

Figure 5-5: Three length scales and local order parameter in non-isometric $C_{10}E_4$/ D_2O/octane system. a) d, ξ and ξ/d, and b) δ.

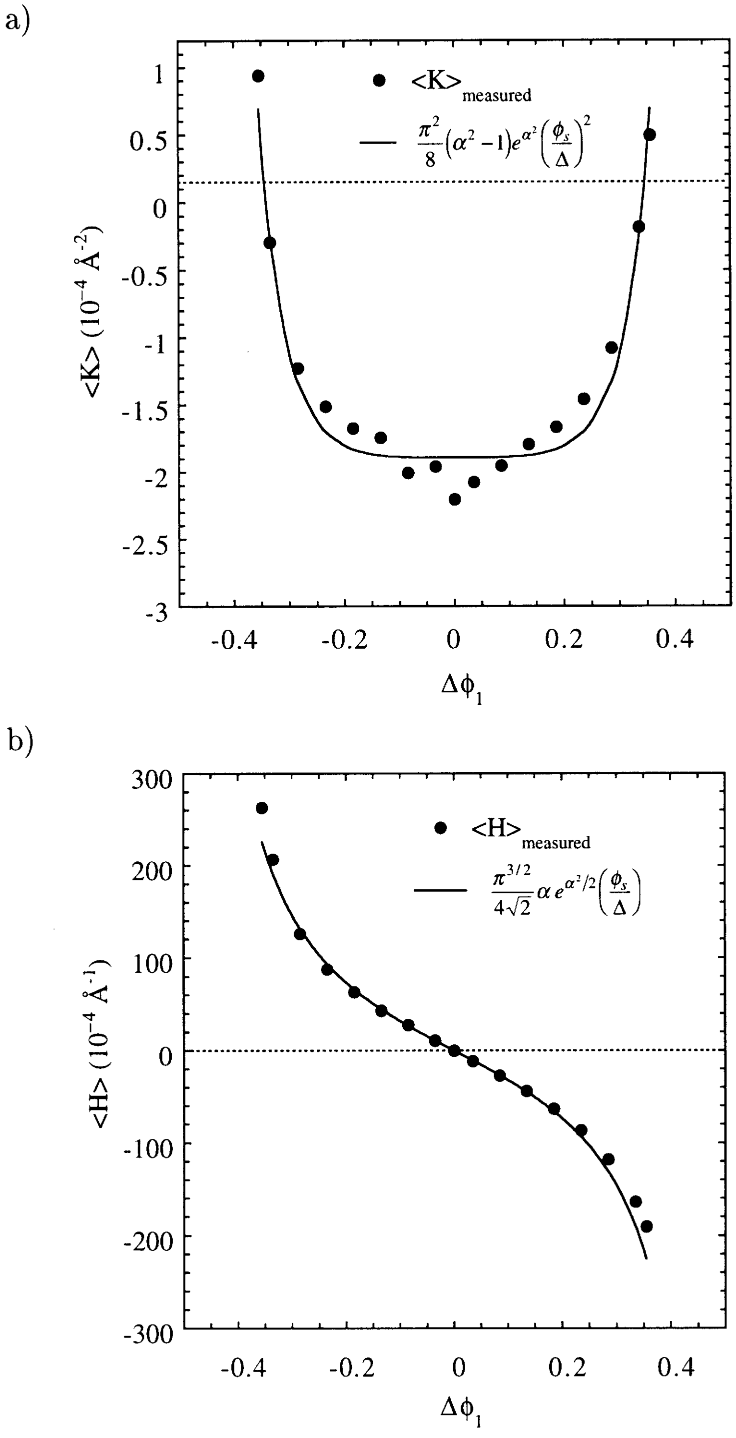

Figure 5-6: Average Gaussian and mean curvatures of non-isometric $C_{10}E_4$/ D_2O/ octane system. a) $\langle K \rangle$ and b) $\langle H \rangle$.

comes more non-isometric, there is *a structural transformation* from a bicontinuous disordered structure to an isolated structure presumably in spherical shape.

Figure 5-6 b) shows the average mean curvature $\langle H \rangle$ as a function of $\Delta\phi_1$. The solid circles are the measured values and the solid line is a theory predicted by the CRW model given as

$$\langle H \rangle = \frac{\alpha \pi^{\frac{3}{2}}}{4\sqrt{2}} e^{\alpha^2/2} \left(\frac{\phi_s}{\Delta} \right) \tag{5.6}$$

where an average Δ was used in the plot. When $\Delta\phi_1$ is zero $\langle H \rangle$ is also zero which means that there is no preferred direction to which the interfaces tend to bend. When $\Delta\phi_1$ is negative, $\langle H \rangle$ is positive and when $\Delta\phi_1$ is positive, $\langle H \rangle$ is negative. The negative $\langle H \rangle$ corresponds to the interfaces bending toward water and the positive $\langle H \rangle$ toward oil. Therefore, there is *a structural inversion across the isometric point* .

Figure 5-7 a) shows the average square mean curvature $\langle H^2 \rangle$ as a function of $\Delta\phi_1$. As $\Delta\phi_1$ becomes more negative, the average square mean curvature decrease until about $\Delta\phi_1 = -0.25$ and then increase. This minimum of the square mean curvature tells us that there is a certain structural transformation occurring around the minimum. In Chapter 4, when $\langle H \rangle = 0$, $\sqrt{\langle H^2 \rangle}$ was interpreted as the root mean square fluctuation of $\langle H \rangle$ about zero and related to the persistence length of interface. Here, the non-zero $\langle H \rangle$ makes it difficult to directly relate $\sqrt{\langle H^2 \rangle}$ to the persistence length. However, the root mean square fluctuation of $\langle H \rangle$ defined as $\sqrt{\langle H^2 \rangle - \langle H \rangle^2}$ can be interpreted similarly. Here, however, the fluctuation is about the residual $\langle H \rangle$ rather than zero. In this interpretation, we can relate $\sqrt{\langle H^2 \rangle - \langle H \rangle^2}$ to the surface roughness parameter δ as following,

$$\sqrt{\langle H^2 \rangle - \langle H \rangle^2} \approx \frac{\delta^{-1}}{\sqrt{5}}. \tag{5.7}$$

As shown in Figure 5-7 b), $\sqrt{\langle H^2 \rangle - \langle H \rangle^2}$ agrees with $\delta^{-1}/\sqrt{5}$ reasonably well. This confirms the physical meaning of δ again.

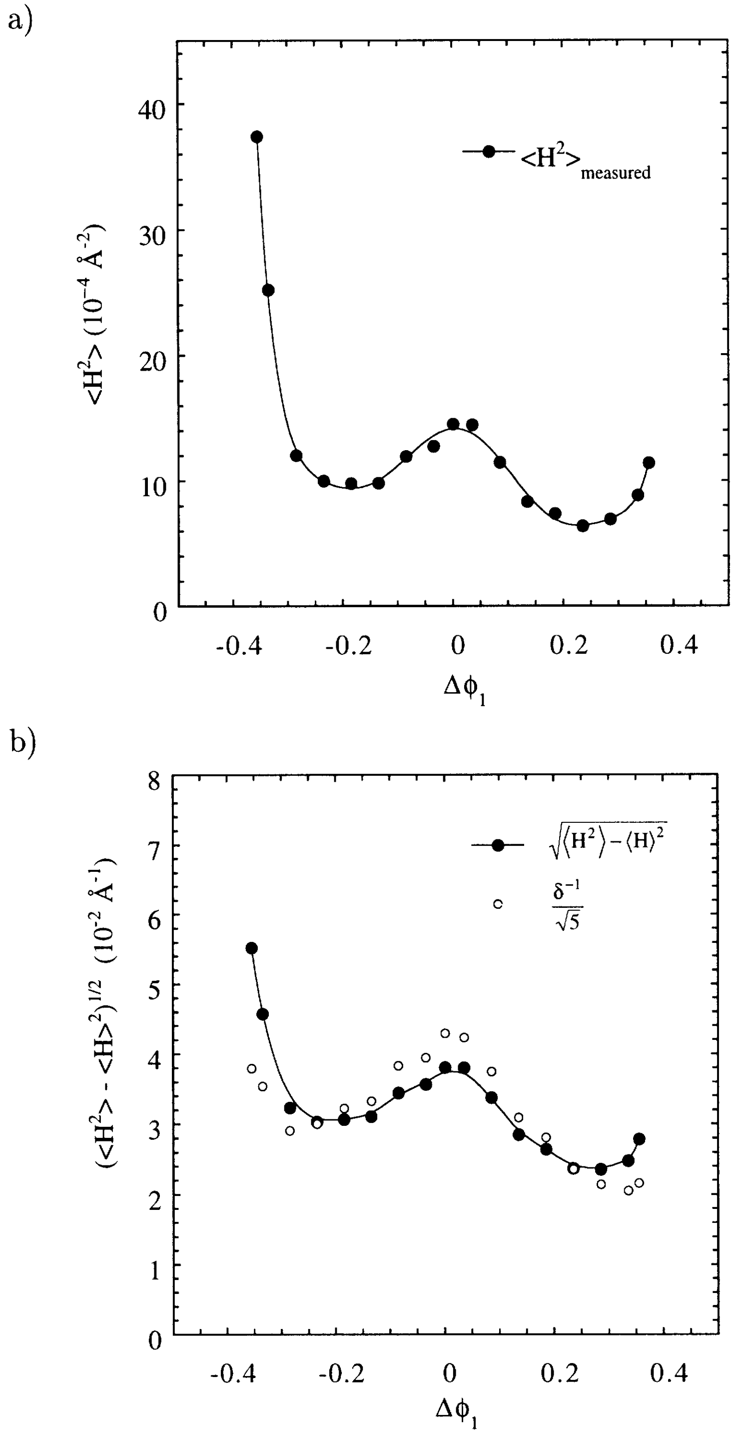

Figure 5-7: Average square mean curvature and its root mean square fluctuation in non-isometric $C_{10}E_4$/ D_2O/ octane system. a) $\langle H^2 \rangle$ and b) $\left(\langle H^2 \rangle - \langle H \rangle^2\right)^{1/2}$.

5.3.2 Non-Isometric Ionic Microemulsions

The SANS intensities of non-isometric AOT/D_2O(NaCl = 0.4 wt %)/decane system are given in Figure 5-8. As shown in Figure 5-2, this system shows an asymmetric phase behavior about $\Delta\phi_1 = 0$. We therefore performed SANS measurements only for the region where $\Delta\phi_1$ is negative and there is enough gap for the existence of a 1 phase. The scattering intensities show a similar trend as the non-isometric $C_{10}E_4/D_2O$/octane system with negative $\Delta\phi_1$.

Figure 5-9 shows the data analysis using the CRW model. The solid lines are the CRW model and the various symbols the SANS intensities. The average Gaussian, mean, and square mean curvatures are calculated using the parameters obtained in this analysis. All the fitted parameters and average interfacial curvatures are listed in Table 5.2.

The inter-domain distance d, the coherence length ξ, and the order parameters ξ/d are given in Figure 5-10 a). As $\Delta\phi_1$ becomes more negative, i.e. more non-isometric with oil-rich composition, d decreases from 239.0 Å (at $\Delta\phi_1 = 0$) to 78 Å (at $\Delta\phi_1 = -0.4$) and ξ also decreases from 83.0 Å (at $\Delta\phi_1 = 0$) to 33 Å (at $\Delta\phi_1 = -0.4$). The behavior of d and ξ in this system is very similar to those in the $C_{10}E_4/D_2O$/octane system. The parameter ξ/d ,however, increases, from 0.35 to 0.44 as $\Delta\phi_1$ becomes more negative while ξ/d in the $C_{10}E_4/D_2O$/octane system decreases. The small bump at $\Delta\phi_1 = 0.35$ is rather puzzling. In fact this corresponds to the point where the transition to an isolated structure occurs and may be understood in that context. Figure 5-10 b) shows the surface roughness parameter δ. As the system becomes more non-isometric, δ increases (from 9.6 Å to 18.5 Å) as it does in the $C_{10}E_4/D_2O$/octane system.

$\langle K \rangle$, $\langle H \rangle$ and $\langle H^2 \rangle$ are shown in Figure 5-11. The overall behavior of the average interfacial curvatures is very similar to those in the $C_{10}E_4/D_2O$/octane system. This tells us that the structural evolution in the 1 phase region (oil-rich side) with $\Delta\phi_1$ is about same in both the ionic and non-ionic microemulsions.

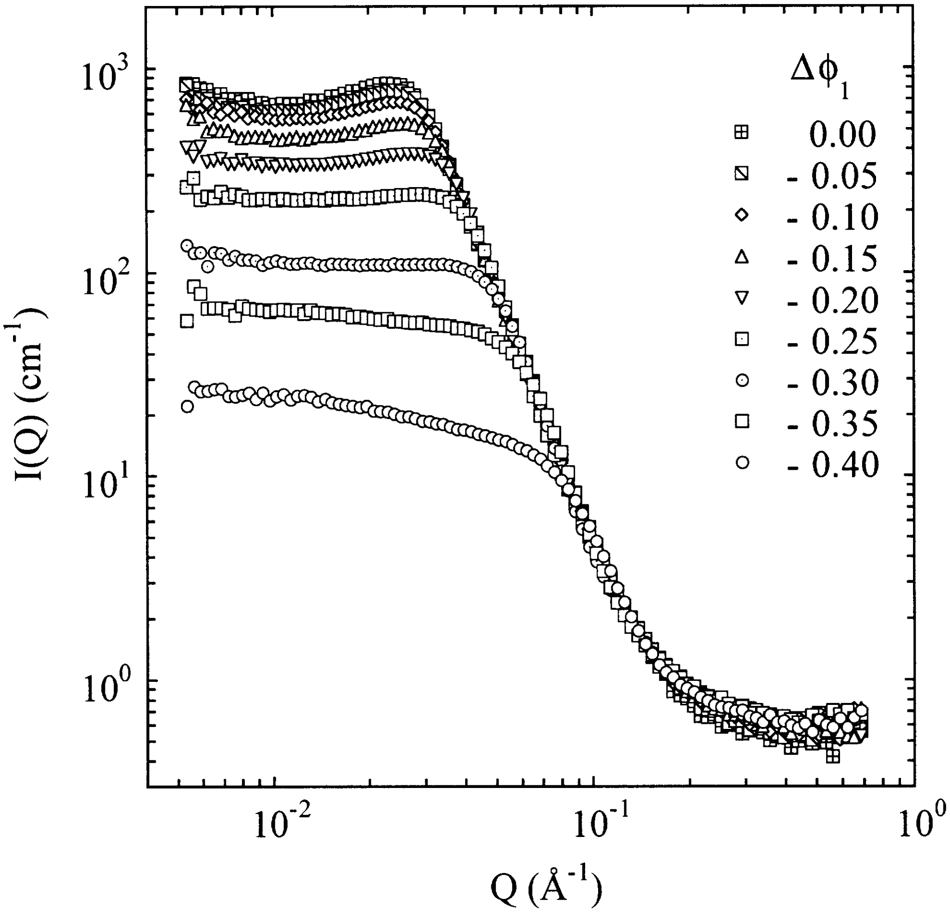

Figure 5-8: SANS intensities of non-isometric AOT/ D_2O/decane system.

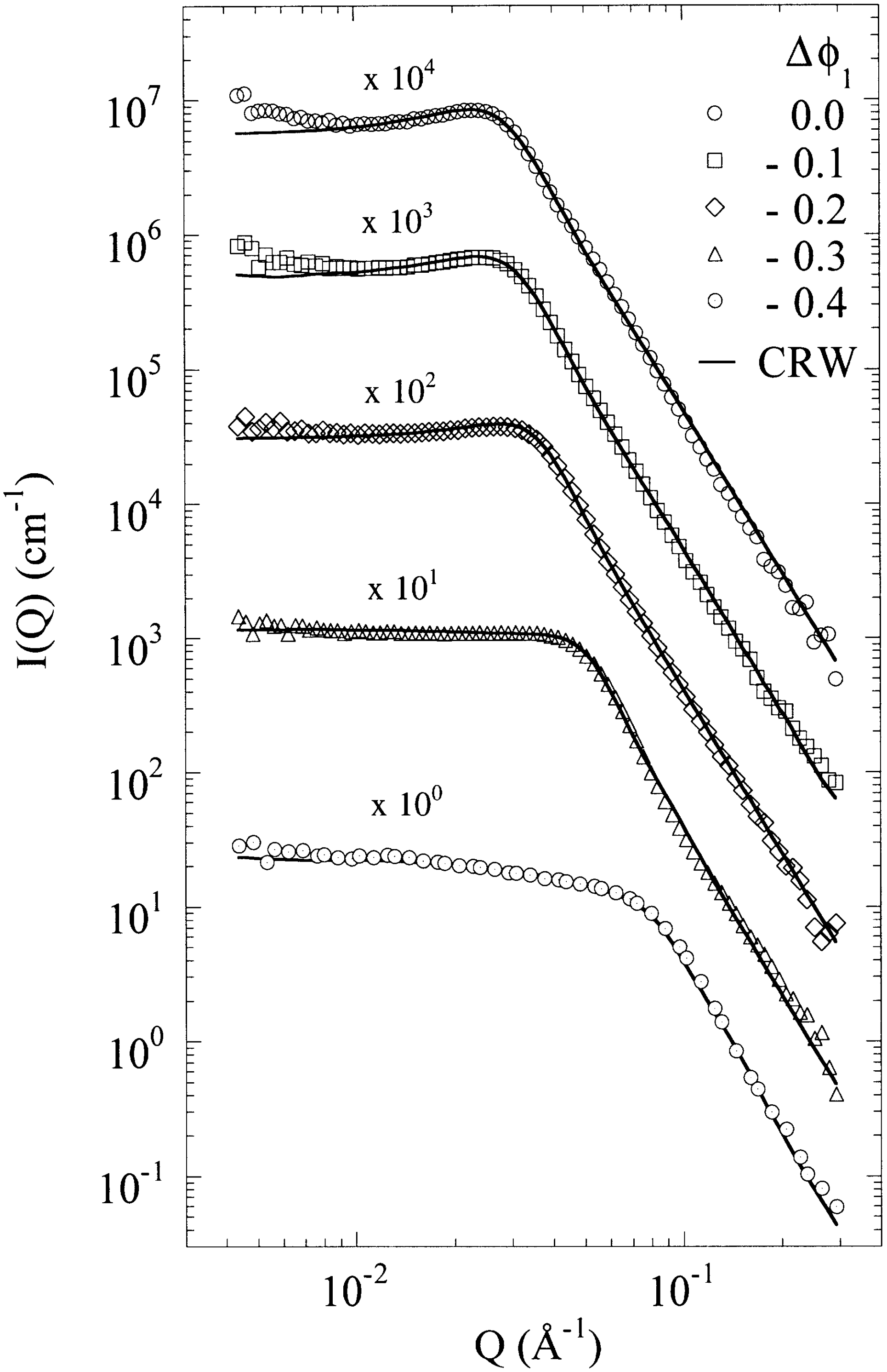

Figure 5-9: Data analysis of non-isometric AOT/D_2O/decane system.

$\Delta\phi_1$	α	d (Å)	ξ (Å)	δ (Å)	ξ/d	$\langle K\rangle$ (10^{-4}Å^{-2})	$\langle H\rangle$ (10^{-4}Å^{-1})	$\langle H^2\rangle$ (10^{-4}Å^{-2})	$(S/V)_1$ (10^{-2}Å^{-1})	$(S/V)_2$ (10^{-2}Å^{-1})	bgd (cm^{-1})	$\langle\eta^2\rangle$ ($10^{21}cm^{-4}$)
0.00	0.0000	238.9	82.9	9.6	0.347	-3.123	0.00	20.58	1.591	1.574	0.494	1.196
-0.05	0.1257	231.5	81.4	10.2	0.351	-3.028	19.54	18.08	1.567	1.574	0.520	1.174
-0.10	0.2533	221.4	77.5	11.8	0.350	-2.791	38.77	14.43	1.506	1.519	0.565	1.108
-0.15	0.3853	206.4	75.8	12.5	0.367	-2.617	59.86	13.09	1.465	1.490	0.575	1.032
-0.20	0.5245	183.2	70.2	15.2	0.383	-2.299	82.78	10.34	1.397	1.461	0.620	0.937
-0.25	0.6745	153.8	62.6	18.3	0.407	-1.965	113.5	9.52	1.362	1.416	0.635	0.841
-0.30	0.8416	125.3	55.7	18.4	0.444	-1.390	162.7	12.08	1.379	1.441	0.637	0.633
-0.35	1.0363	106.3	42.1	15.4	0.396	0.500	239.8	21.01	1.375	1.399	0.640	0.551
-0.40	1.2815	76.6	33.2	16.5	0.433	6.762	368.3	35.03	1.283	1.576	0.650	0.333

Table 5.2: The fitted parameters of non-isometric AOT/D_2O/decane system

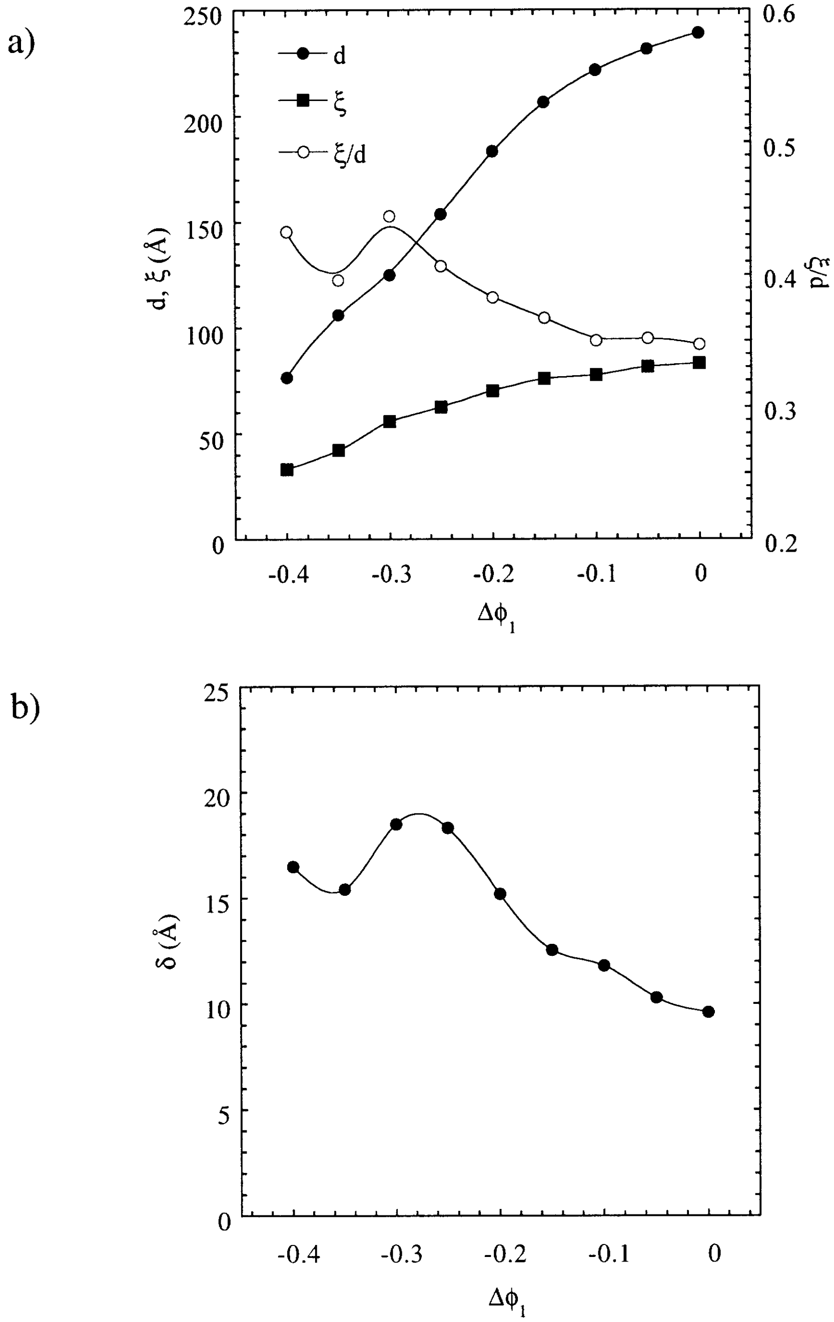

Figure 5-10: Three length scales and local order parameter in non-isometric AOT/ D_2O/ decane system. a) d, ξ and ξ/d, and b) δ.

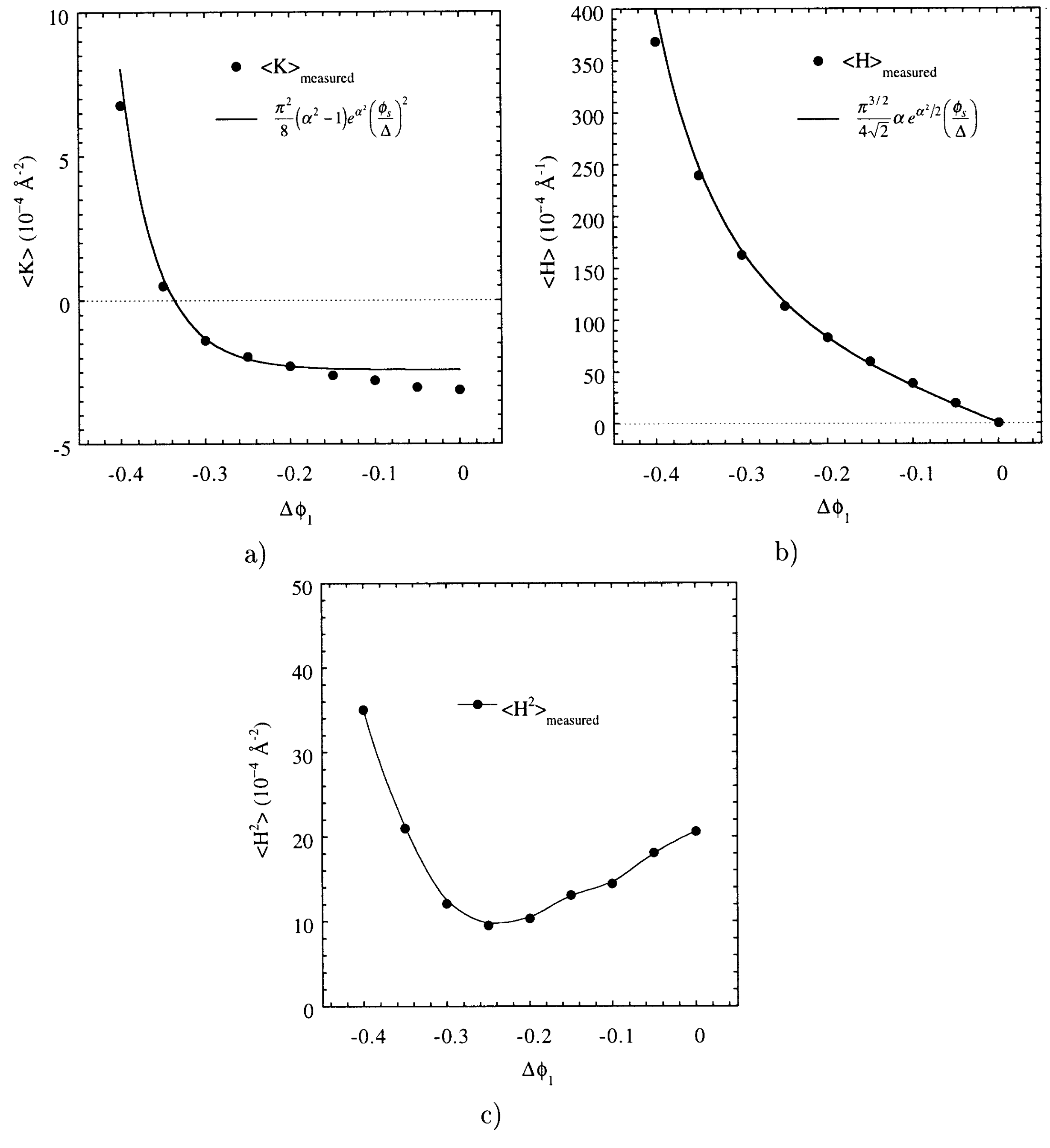

Figure 5-11: The interfacial curavtures of non-isometric AOT/D_2O/decane system. a) average Gaussian, b) average mean, and c) average square mean curvatures.

5.4 Structural Transformations in Non-Isometric Microemulsions

The average interfacial curvatures in non-isometric microemulsions presented in section 5.3 provided us insights on the structural transformations in a quantitative way. In this section, a series of 3-dimensional simulations of the non-isometric microemulsions are presented and discussed. In these simulations, the experimentally measured parameters d, ξ, and δ in Table 5.1 were used. These simulations will confirm our quantitative understanding of the structures and provide further insights in a qualitative way. It was shown that the non-isometric AOT/D_2O/decane system with negative $\Delta\phi_1$ shows similar behavior in terms of the average interfacial curvatures to those of the non-isometric $C_{10}E_4$/D_2O/octane system. In this section, therefore, only the 3 dimensional simulations of the non-isometric $C_{10}E_4$/D_2O/octane system are discussed.

In Figure 5-6 b), it was shown that $\langle H \rangle$ changes its sign at $\Delta\phi_1 = 0$. This was interpreted as *a structural inversion* from the interfaces bending toward water (when $\Delta\phi_1 < 0$) to the interfaces bending toward oil (when $\Delta\phi_1 > 0$). Figure 5-12 shows the 3D simulations made for $\Delta\phi_1$ = -0.185, 0, and 0.185 (solid squares in the phase diagram). The corresponding $\langle H \rangle$'s are -63.00×10^{-4}Å^{-1}, 0 Å^{-1} and 62.87×10^{-4}Å^{-1} and $\langle K \rangle$'s -1.673×10^{-2}Å^{-2}, -2.203×10^{-4}Å^{-2}, and -1.665×10^{-2}Å^{-2} respectively. While $\langle H \rangle$ changes its sign at $\Delta\phi_1 = 0$, $\langle K \rangle$ is negative in all three cases. In the 3D simulations, the dark side corresponds to the surface facing the water region and the bright side the surface facing the oil region. The simulation at $\Delta\phi_1 = 0$ shows a bicontinuous structure which consists of a interface with no preferred direction to bend. However, at $\Delta\phi_1$ = -0.185, the simulation shows an interfacial structure which bends toward water and, at $\Delta\phi_1$ = 0.185, toward oil. These clearly confirms our interpretation of $\langle H \rangle$. Another thing to notice in these simulations is that all the structures are bicontinuous and dominated by saddle shaped interfaces, which is consistent with negative $\langle K \rangle$.

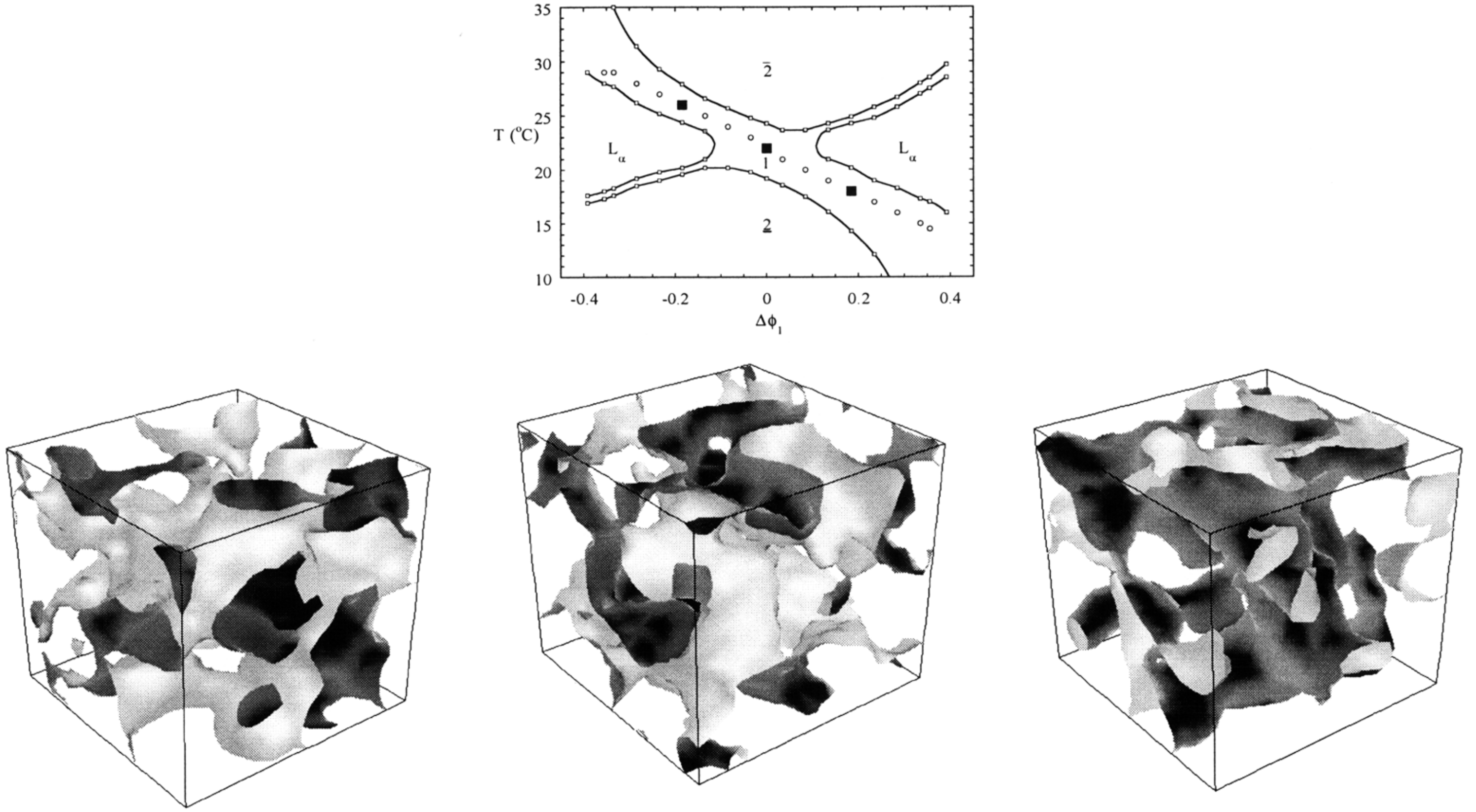

$\Delta\phi_1 = -0.185$ $\Delta\phi_1 = 0.0$ $\Delta\phi_1 = 0.185$

Figure 5-12: Structural Inversion in non-isometric $C_{10}E_4/D_2O$/octane system. Box = $480 \times 480 \times 480 \text{Å}^3$.

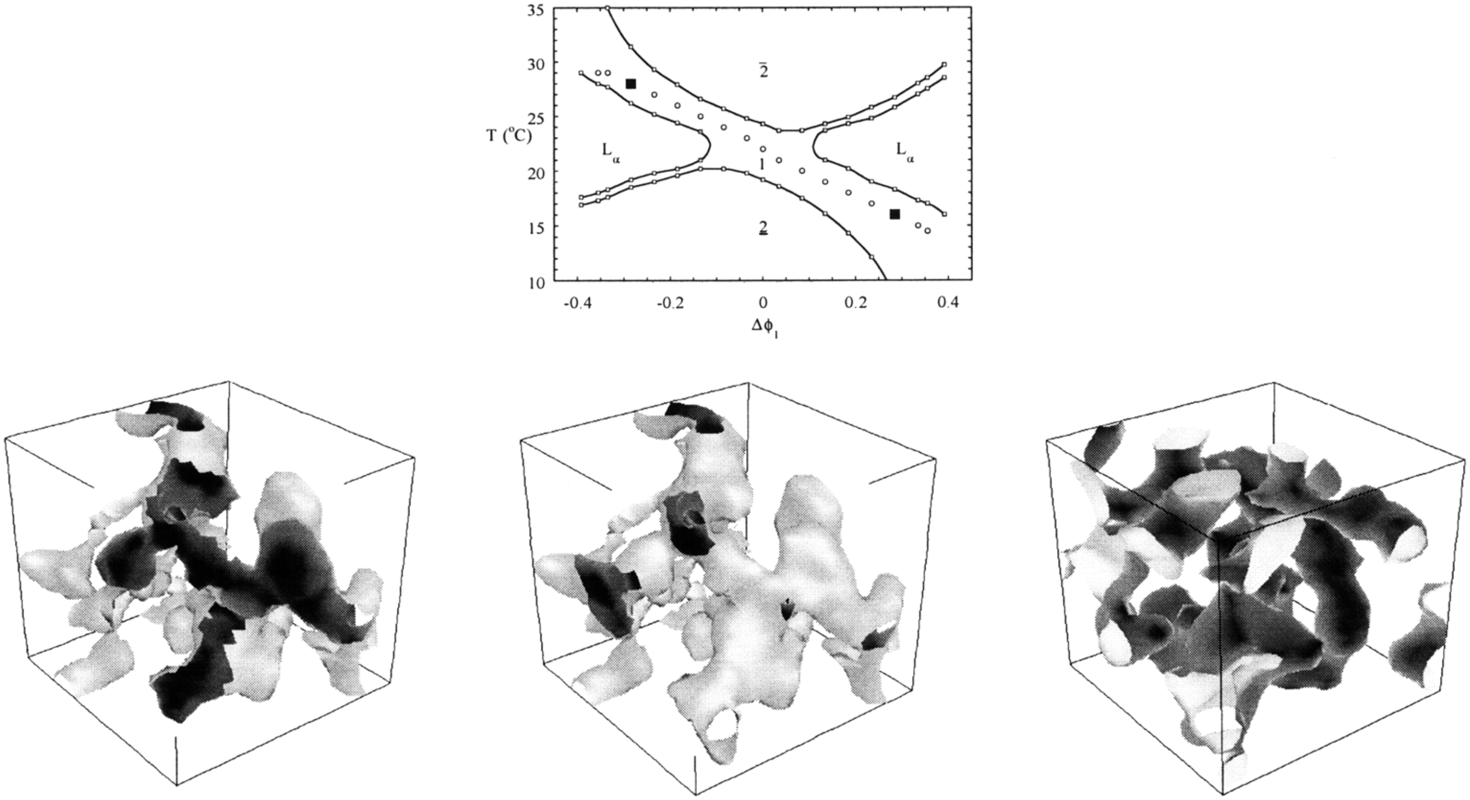

$\Delta\phi_1 = -0.285$ $\Delta\phi_1 = -0.285$ $\Delta\phi_1 = 0.285$

Figure 5-13: Cylindrical structure in non-isometric $C_{10}E_4/D_2O$/decane system. Box = $480 \times 480 \times 480 \text{Å}^3$.

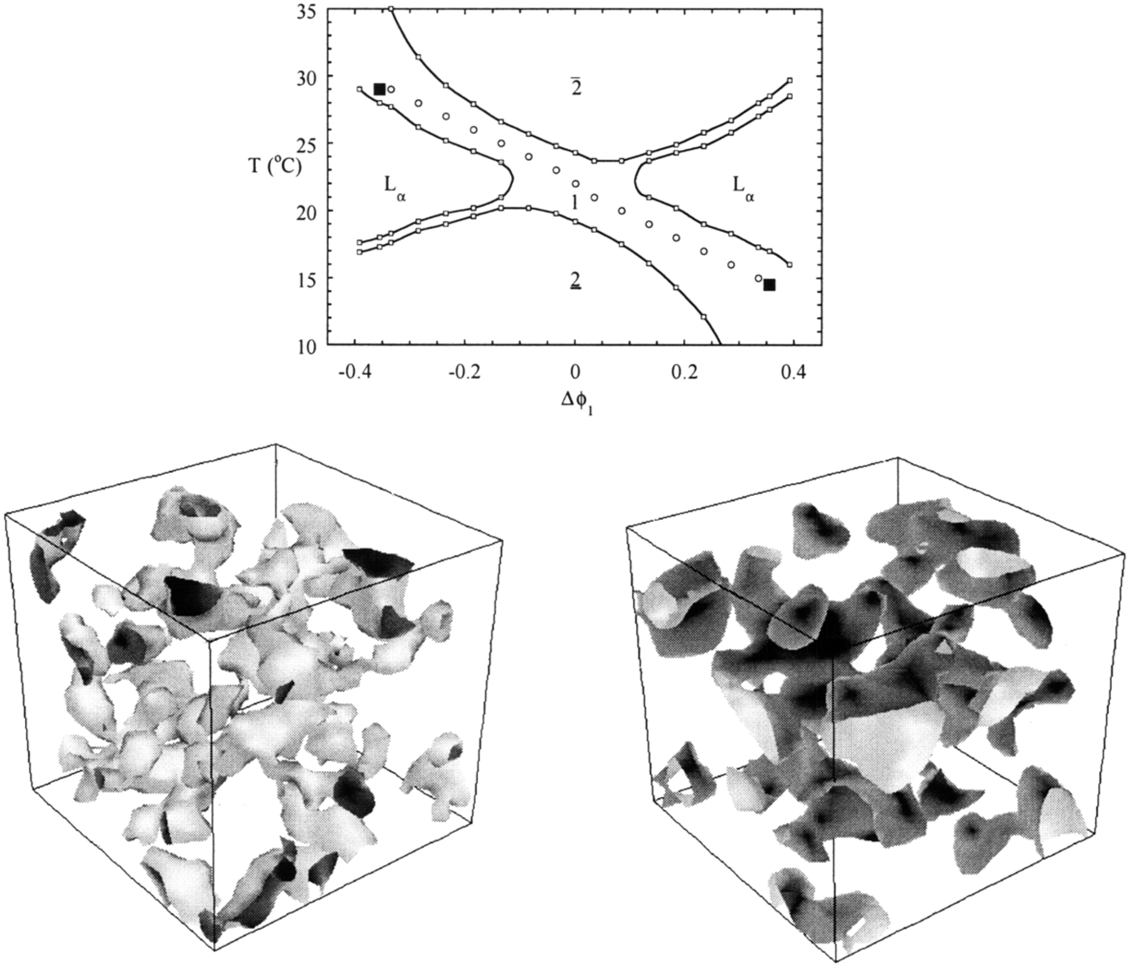

$\Delta\phi_1 = -0.355$

$\Delta\phi_1 = 0.355$

Figure 5-14: Globular structure in non-isometric $C_{10}E_4/D_2O$/decane system. Box = $480 \times 480 \times 480 Å^3$.

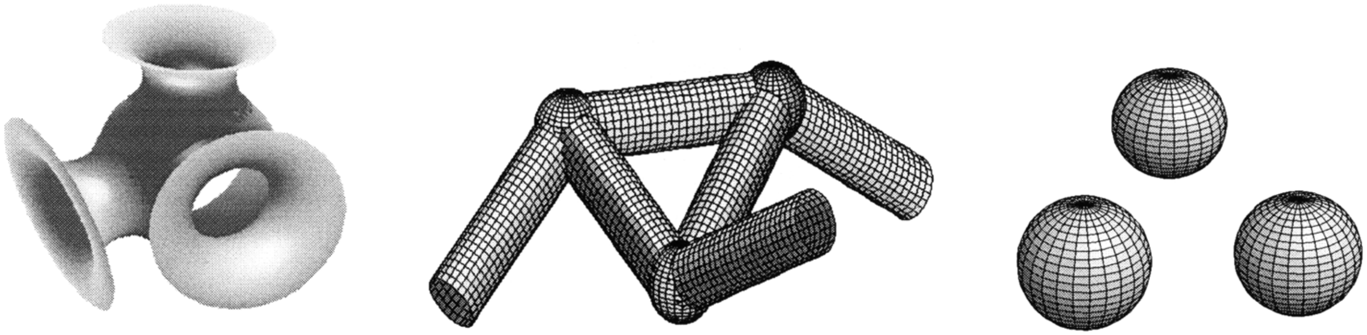

$|\Delta\phi_1| \sim 0.0$ $|\Delta\phi_1| \sim 0.25$ $|\Delta\phi_1| > 0.35$

Figure 5-15: Schematic diagram of the structural transformation in non-isometric microemulsions.

In the previous section it was shown that as the system becomes more non-isometric, $\langle H \rangle$ becomes more positive or more negative and $\langle K \rangle$ less negative. The behavior of $\langle H \rangle$ is interpreted as the stronger tendency to bend toward oil or water respectively and that of $\langle K \rangle$ as the lesser dominance of the saddle shaped interfaces in the interfacial structures. Figure 5-13 shows the simulations at $\Delta\phi_1 = -0.285$ and 0.285. To show the path of the water region more clearly, the simulation at $\Delta\phi_1 = 0$ is shown in two different boxes, one with part of the interface removed and another without. It is interesting to notice that the water region at $\Delta\phi_1 = -0.285$ and the oil region at $\Delta\phi_1 = 0.285$ are connected through rather cylindrical shape passages in each case. In a diagrammatic description, the interfacial structures in these systems are *a network of cylindrical pipes* , which is consistent with the measured average interfacial curvatures.

When $\Delta\phi_1$ is -0.335 or 0.335, $\langle K \rangle$ is positive, which means that the corresponding interfacial structures are dominated by isolated surfaces without holes. The 3D simulations at these points are shown in Figure 5-14, which confirms our interpretations.

Summarizing the results of the average interfacial curvatures and the corresponding 3D simulations, the structural transformations in non-isometric microemulsions are described in a pictorial diagram shown in Figure 5-15. The isometric microemulsion in 1 phase region takes a balanced disordered bicontinuous structure in which the saddle shaped interfaces are dominant. Once the system becomes non-isometric, the interfaces bend toward either oil or water depending on the compositions. When $|\Delta\phi_1|$ is around 2.5, the interfacial structure takes the form of a network connected through cylindrical pipes. With further increase of $|\Delta\phi_1|$ above 0.35, it becomes isolated globular surfaces.

Chapter 6

Conclusions

Microemulsions exhibit a wide variety of phases with corresponding mesoscopic scale interfacial structures. While the relation between the interfacial structure and the phase behavior are very important for industrial as well as scientific purposes, the complexity of the interfacial structures has been a huddle in identifying the relation in a quantitative way. For a quantitative description complex random interfaces, the natural parameters to be measured are the interfacial curvatures : the Gaussian, mean, and square mean curvatures. Here we studied the relation in both isometric and non-isometric microemulsion systems by measuring the interfacial curvatures with the SANS techniques.

To extract the interfacial curvatures from SANS intensities, we developed a new SANS data analysis method. The method involves the use of a clipped random wave model, in which all crucial informations of the interfacial structures are contained in a spectral function. We introduced an inverse 8th order polynomial spectral function which contains three basic length scales : the inter-domain distance, the coherence length, and the surface roughness parameter. These three length scales are essential to describe mesoscopic scale random interfaces and have definite correlations with characteristic features of SANS intensities from bicontinuous microemulsions. The inter-domain distance and the coherence length explain the position and the width of a peak in the SANS intensity. The surface roughness parameter, a newly introduced length scale, corresponds to the large Q behavior of the SANS intensity, relating it to the local fluctuation of interfaces. This appropriate description of the local wrinkling of the interfaces permits correct estimation of the surface to volume ratio which is one of the most crucial informations in porous materials.

A series of SANS experiments were performed at various phase points of isometric and non-isometric microemulsions. Using the developed model, the three interfacial curvatures at each phase points were determined for the first time in a practical way.

In isometric bicontinuous microemulsions, the Gaussian curvature is negative and has a parabolic dependence on the surfactant volume fraction. The negative Gaussian curvature means that the structures are dominated by saddle shaped interfaces and have many holes. Using the measured three length scales, a series of three-dimensional simulations were generated and used to support our interpretation of the measured curvatures. The curvatures and the simulations are consistent with each other.

In non-isometric systems, as the water and oil composition becomes more asymmetric, the interfacial curvatures show very systematic behaviors : the Gaussian curvature becomes less negative and eventually changes its sign to positive, the mean curvature changes its sign at the isometric composition, and the square mean curvature has a minimum around $\Delta\phi_1 = 0.25$. Based on these results, a characteristic structural transformation was identified. As water and oil volume ratio moves away from unity, a bicontinuous structure transforms to a spherical structure through a cylindrical structure.

The discovery of the structural transformations as a function of phase behavior is an important step for the full understanding of the physics of microemulsions and their industrial applications. The further study to find the correlations between the measured interfacial curvatures and the physical properties of the surfactant monolayers will be very useful in this context. The developed SANS data analysis for curvature measurements, which can also be applied for the small-angle x-ray scattering data, will provide a quantitative tool in revealing complex interfacial structures of various porous materials which are often puzzling to describe in simple terms.

Bibliography

[1] *Micelles, Membranes, Microemulsions, and Monolayers.* Spinger-Verlag, New York, 1993. edited by W. M. Gelbart, A. Ben-Shaul, and D. Roux.

[2] *Surfactants in Solution.* Plenum Press, New York and London, 1984. edited by M. Bothorel.

[3] *Microemulsion Systems.* Marcel Dekker, Inc., New York and London, 1987. edited by H. L. Rosano and M. Clausse.

[4] *Structue and Dynamics of Strongly Interacting Colloids and Superamolecular Aggregates in Solution.* Kluwer,Dordrecht, 1992. edited by S. H. Chen and J. S. Huang, and P. Tartaglia.

[5] *The Structure and Conformation of Amphiphilic Membranes.* Springer-Verlag, Berlin, 1992. edited by R. Lipowsky, D. Richter, and K. Kremer.

[6] *The Structure and Conformation of Amphiphilic Membranes.* Springer-Verlag, Berlin, 1992. edited by R. Lipowsky, D. Richter, and K. Kremer.

[7] G. Gompper and M. Schick. *Self-Assembling Amphiphilic Systems.* Academic, New York, 1994.

[8] *Physics of Amphiphilic Layers.* Springer-Verlag, New York, 1987. edited by J. Meunier and D. Langevin and N. Boccara.

[9] A. M. Cazabat, C. Langevin, J. Meunier, and A. Pouchelon. *Adv. Colloid Interface Sci.*, 16:175, 1982.

[10] P. A. Winsor. *Solvent Properties of Amphiphilic Compounds.* Butterworth Scientific Publications, London, 1954.

[11] L. E. Scriven. *Nature*, 123:263, 1976.

[12] L. E. Scriven. *in Micellization, Solubilization, and Microemulsions*, volume 2. Plenum Press, New York, 1977. edited K. L. Mittal.

[13] M. Kahlweit and R. Strey. *Angew. Chem. Int. Ed. Engl.*, 24:654, 1985.

[14] M. Kahlweit and R. Strey. *Microemulsion Systems*, page 1, 1987. edited by H. L. Rosano and M. Clausse.

[15] C. U. Herrmann, G. Klar, and M. Kahlweit. *Microemulsions*, page 1, 1981. edited by I. D. Robb.

[16] R. E. Goldstein and J. S. Walker. *J. Chem. Phys.*, 78:1492, 1983.

[17] D. Andelman, M. Cates, D. Roux, and S. A. Safran. *J. Chem. Phys.*, 87:7229, 1987.

[18] L. Golubovic and T. C. Lubensky. *Phys. Rev. A*, 41:43, 1990.

[19] M. E. Cates, D. Roux, D. Andelman, S. T. Miller, and S. A. Safran. *Europhys. Lett.*, 5:733, 1988.

[20] S. H. Chen, S. L. Chang, R. Strey, and P. Thiyagarajan. *J. Phys.:Condens. Matter*, 3:F91, 1991.

[21] H. Wennerstrom and U. Olsson. *Langmuir*, 9:365, 1993.

[22] M. Lagues, R. Ober, and C. Taupin. *J. Phys. Lett.*, 39:487, 1978.

[23] D. J. Cebula, R. M. Ottewill, J. Ralston, and P. N. Pusey. *J. Chem. Soc. Faraday Trans. 1*, 77:2585, 1981.

[24] D. Guest, L. Auvary, and D. Langevin. *J. Phys. Lett.*, 46:1055, 1985.

[25] M. Kotlarchyk, S. H. Chen, J. S. Huang, and M. W. Kim. *Phys. Rev. Lett.*, 53:941, 1984.

[26] A. De Geyer and J. Tabony. *J. Chem. Phys. Lett.*, 113:83, 1985.

[27] E. W. Kaler, H. T. Davis, and L. E. Scriven. *J. Phys. Chem.*, 79:5685, 1983.

[28] S. W. Loversey. *Theory of Neutron Scattering from Condensed Matter : Vol. I and II.* Clarendon Press, Oxford, 1984.

[29] A. Forderaro. *The Elements of Neutron Interaction Theory.* MIT press, Cambridge, 1971.

[30] A. Guinier and G. Fournet. *Small-Angle Scattering of X-Rays.* Wiley, New York, 1955.

[31] O. Glatter and O. Kratky. *Small-Angle Scattering of X-Rays.* Academic, New York, 1982.

[32] P. Debye, H. R. Anderson, and H. Brumberger. *J. Appl. Phys.*, 28:679, 1957.

[33] G. E. Bacon. *Neurton Difrraction.* Clarendon Press, Oxford, 1975.

[34] B. Jacrot. *Rep. Prog. Phys.*, 39:911, 1976.

[35] V. F. Sears. *Neutron News*, 3:26, 1992.

[36] N. J. Chang and E.W. Kaler. *J. Chem. Phys.*, 89:2996, 1985.

[37] R. Strey, J. Winkler, and L. Magid. *J. Chem. Phys.*, 95:7502, 1991.

[38] V. Degiorgio, R. Piazza, M. Corti, and C. Minero. *J. Chem. Phys.*, 82:1025, 1985.

[39] Von R. Kirste and G. Porod. *Kolloid-Z Z f. Polym.*, 184:1, 1962.

[40] G. Porod. *in Small Angle X-ray Scattering.* Academic, New York, 1982. edited by O. Glatter and O. Kratky.

[41] P. Debye and A. M. Bueche. *J. Appl. Phys.*, 20:518, 1949.

[42] G. Porod. *Kooloid Z.*, 124:83, 1951.

[43] L. Auvary, J. P. Cotten, R. Ober, and C. Taupin. *J. Phys. Chem.*, 88:4586, 1984.

[44] L. D. Landau and E. M. Lifschitz. *Statistical Physics.* 3rd Edition, Pergamon, New York, 1980.

[45] G. Gompper and M. Schick. *Phys. Rev. Lett.*, 62:1647, 1989.

[46] M. Teubner and R. Strey. *J. Chem. Phys.*, 87:3195, 1987.

[47] J. W. Cahn. *J. Chem. Phys.*, 42:93, 1965.

[48] N. F. Berk. *Phys. Rev. Lett.*, 14(5):1, 1987.

[49] N. F. Berk. *Phys. Rev. A*, 44(8):5069, 1991.

[50] R. J. Adler. *The Geometry of Random Fields.* Chichester, 1981.

[51] M. Teubner. *Europhys. Lett*, 14(5):403, 1991.

[52] P. Pieruschka and S. A. Safran. *Europhys. Lett.*, 22:625, 1993.

[53] S. H. Chen and S. M. Choi. *J. Appl. Crystallogr.*, 30:755, 1997.

[54] S. H. Chen and S. M. Choi. *Physica A*, 236:38, 1997.

[55] P. Pieruschka and S. Marcelija. *J. de Phys II*, 2:235, 1992.

[56] S. H. Chen, D. D. Lee, and S. L. Chang. *J. Mol. Structure*, 296:259, 1993.

[57] O. Barrett. *Elementary Differential Geometry.* Academic Press, 1966.

[58] M. Spivak. *A Comprehensive Introduction to Differential Geometry.* Perish, Berkeley, 1979.

[59] W. Helfrich. *Z. Naturforsch A*, 33:305, 1978.

[60] P. G. De Gennes and C. Taupin. *J. Phys. Chem.*, 86:2294, 1982.

[61] J. Jouffroy, P. Levinson, and P.G. De Gennes. *J. Phys. (Paris)*, 43:1241, 1982.

[62] B. Widom. *J. Chem. Phys.*, 81:1030, 1984.

[63] S. A. Safran, D. Roux, M. E. Cates, and D. Andelman. *Phys. Rev. Lett.*, 57:491, 1986.

[64] S. M. Choi and S. H. Chen. *Prog. Colloid Poly. Sci.*, 106:14, 1997.

[65] S. M. Choi, S. H. Chen, T. Sottmann, and R. Strey. *Physica B.* in print.

[66] H. Kuniedat and K. Shinoda. *J. Colloid. Interface Sci.*, 75:601, 1980.

[67] M. Kahlweit, R. Strey, R. Schomacker, and D. Haase. *Langmuir*, 5:305, 1989.

[68] S. H. Chen, T. L. Lin, and Huang Lin. *Physics of Complex and Supermolecular Fluids*, page 285, 1987. Edited by S. A. Safran and N. A. Clark.

[69] S. H. Chen, S. L. Chang, and R. Strey. *J. Appl. Crystallogr.*, 24:721, 1991.

[70] S. H. Chen, S. L. Chang, and R. Strey. *J. Chem. Phys.*, 92:2294, 1988.

[71] M. Kahlweit, R. Strey, P. Firman, D. Haase, J. Jen, and R. Schomacker. *Langmuir*, 4:409, 1988.

[72] D. D. Lee and S. H. Chen. *Phys. Rev. Lett.*, 73:106, 1994.

[73] S. H. Chen, S. L. Chang, and R. Strey. *J. Chem. Phys.*, 93:1907, 1990.

[74] S. M. Choi and S. H. Chen. *Phys. Rev. E.* in preparation.

Appendix A

Least Square Data Fitting Program

```
cccccccccccccccccccccccccccccccccccccccccccccccccccccccccccccccccccccccc
c
c    SANSCURV.f
c
c    A Small-Angle Neutron Scattering Data Analysis Program
c    to extract the interfacial curvatures :
c      the average Gaussian curvature
c      the average Mean curvature
c      the average Square mean curvature
c    in Microemulsion Systems
c
c    Sung-Min Choi
c
c    Department of Nucelar Engineering
c    Massachusetts Institute of Technology
c    1996 - 1998
c
cccccccccccccccccccccccccccccccccccccccccccccccccccccccccccccccccccccccc

cccccccccccccccccccccccccccccccccccccccccccccccccccccccccccccccccccccccc
c    Main Program
```

```
cccccccccccccccccccccccccccccccccccccccccccccccccccccccccccccccccccccccc

      implicit none
      character*20 file_input(3), LAB, file_output, state, xsec_model
      character*50 junk
      real*8  ave, fave
      real*8 reso, ftemp
      integer pnumber, i,estart(3), enumber, imax, imequ
      integer iprint, resyn, nfold, sets, ii
      real*8 prm, step, bound, oldchi, sig
      real*8 edat(3,4,200),r1,r2,rl1,rl2,rlam,dlam,rdet
      common/general/estart, enumber(3), prm(200), bound(2,200), imax
      common/resof1/reso(3,200,200),r1,r2,rl1,rl2,rlam,dlam,rdet,resyn
      common/resof2/sig(3,200),nfold
      common/QQQ/ave(200), fave(200), imequ, iprint, sets
c
c
      open(unit=5,file='parameter_input',status='old')
      rewind(unit=5)
cccccccccccccccccccccccccccccccccccccccccccccccccccccccccccccccccccccccc
c     Laboratory where the data was taken
cccccccccccccccccccccccccccccccccccccccccccccccccccccccccccccccccccccccc
      read(5,1201) LAB
      print *,'LAB : ',LAB
cccccccccccccccccccccccccccccccccccccccccccccccccccccccccccccccccccccccc
 3333 read(5,1201) state
      if(state.eq.'stop') go to 4444
cccccccccccccccccccccccccccccccccccccccccccccccccccccccccccccccccccccccc
c     Number of data sets to be analyzed
cccccccccccccccccccccccccccccccccccccccccccccccccccccccccccccccccccccccc
      read(5,*) sets
      do 170 i=1,sets
        read(5,1201) file_input(i)
        read(5,*) estart(i)
        read(5,*) enumber(i)
  170 continue
```

```
1201 format(a20)
      read(5,1201) file_output
c
c
      open(unit=10,file='test', status='unknown')
      rewind(unit=10)
      do 190 ii=1,sets
        open(unit=7,file=file_input(ii), status='old')
        rewind(unit=7)
        if(estart(ii).eq.1) go to 117
        do 2 i=1,estart(ii)-1
          read(7,1202) junk
 2      continue
 1202   format(a50)
 117    do 3 i=1, enumber(ii)
          read(7,*) edat(ii,1,i), edat(ii,2,i), edat(ii,3,i)
          if(LAB.eq.'ORNL') then
            edat(ii,1,i) = edat(ii,1,i)/10.
          endif
          write(10,1023) edat(ii,1,i),edat(ii,2,i),edat(ii,3,i)
 3      continue
        close(unit=7)
 190  continue
      close(unit=10)
c
c
      read(5,1201) xsec_model
      print *,xsec_model
      read(5,*) pnumber
      do 1 i=1,pnumber
        read(5,*) prm(i), bound(1,i), bound(2,i)
 1    continue

      read(5,*) step
      read(5,*) ftemp
      read(5,*) imequ
```

```
      read(5,*) imax
      read(5,*) iprint
      read(5,*) resyn
c
c
c
ccccccccccccccccccccccccccccccccccccccccccccccccccccccccccccccccccc
 19   call anneal(edat,ftemp,pnumber,step,oldchi,state,xsec_model)
ccccccccccccccccccccccccccccccccccccccccccccccccccccccccccccccccccc
c
      open(unit=7,file=file_output,status='unknown')
      rewind(unit=7)
      write(7,*) LAB
      write(7,*) xsec_model
      write(7,1023) oldchi
      write(7,*) ' '
      do 20 i=1,pnumber
         write(7,1023) prm(i),ave(i),fave(i)
 20   continue
 1023 format(3e15.6)
      close(unit=7)
c
      go to 3333
 4444 close(unit=5)
      stop
      end
ccccccccccccccccccccccccccccccccccccccccccccccccccccccccccccccccccccc
c     END OF MAIN PROGRAM
ccccccccccccccccccccccccccccccccccccccccccccccccccccccccccccccccccccc




ccccccccccccccccccccccccccccccccccccccccccccccccccccccccccccccccccccc
c      Functions and Subroutines
```

```
cccccccccccccccccccccccccccccccccccccccccccccccccccccccccccccccccccc


cccccccccccccccccccccccccccccccccccccccccccccccccccccccccccccccccccc
      real*8 function xsec(Q, prm, xsec_model)
cccccccccccccccccccccccccccccccccccccccccccccccccccccccccccccccccccc
c     The cross-section for each model.
c
c
      implicit none
      character*20 xsec_model
      real*8 prm(200), Q, dsld, pi
      real*8 thy, d, AA, BB, Z
      real*8 a,b,c,alpha,sigma,V1,xl,xu,xxl,xxu,dx,xn,msld,bgd
      real*8 cs,cw,co,ds,dw,do,bgds,dsld2
      real*8 t,px,Vw,ps,xsecm,eta2
      real*8 funcg,ss,sssum
      external funcg, ftnGauss, ftnDint
      integer n,i
c
c
        pi = 3.141592653

cccccccccccccccccccccccccccccccccccccccccccccccccccccccccccccccccccc
c     Choi and Chen Model for microemulsion
c
c     S. M. Choi and S. H. Chen, Progr. Colloid Poly. 106:14 (1997)
c     S. H. Chen and S. M. Choi, J. Appl. Crystallogr. 30:755 (1997)
cccccccccccccccccccccccccccccccccccccccccccccccccccccccccccccccccccc
c
c Fitting function
c
c I(Q) = <n^2> Int(0,oo) F(r) sin(Qr)/Qr 4 Pi r^2 dr + background
c
c where <n^2> = V1*V2(rho1-rho2)^2
c       When alpha=0
```

```
c     F(r) = 2/Pi arcsin(g(r)) : Debye correlation function
c     When alpha =/ 0  (small alpha expansion)
c     F(r) = 1-1/(2 pi V1(1-V1) {acos(g(r))-alpha^2 tan(acos(g(r))/2)}
c
c     g(r) = from f(k) ~1/k^8
c
c     g(0) = 1 : asymptotic
c     g(oo)= 0
c
c     msld = <n^2>
c     bgd = background
c     xl = lower limit of integration = 0
c     xu = upper limit of integration = oo,
c         in practice xu is determined by the shape of the integrand
c     xn = number of intervals for integration
c
      if(xsec_model .eq. 'gauscur') then
        a = prm(1)
        b = prm(2)
        c = prm(3)
        alpha = prm(4)
        V1 = prm(5)
        sigma = prm(6)
        msld = prm(7)
        bgd = prm(8)
        xl = prm(9)
        xu = prm(10)
        xn = prm(11)
        if (Q .le. 0.01) then
          xn =  1 * xn
        elseif (Q .le. 0.05) then
          xn =  1 * xn
        elseif (Q .le. 0.1) then
          xn = 1 * xn
        else
          xn = 5 * xn
```

```
      endif

      dx = (xu-xl)/xn
      n = int(xn)
      xxl=0
      xxu=dx
      sssum=0

      call qgaus(funcg,Q,a,b,c,alpha,V1,xxl,xxu,ss)

      sssum=sssum+ss

      do 1212 i = 1,n
         xxl=xxl+dx
         xxu=xxu+dx
         call qgaus(funcg,Q,a,b,c,alpha,V1,xxl,xxu,ss)
         sssum=sssum+ss
1212  continue

      xsec = msld * sssum *exp(-sigma**2.*Q**2.) + bgd

      return


cccccccccccccccccccccccccccccccccccccccccccccccccccccccccccccccccccccc
c     Film Contrast
cccccccccccccccccccccccccccccccccccccccccccccccccccccccccccccccccccccc

     elseif(xsec_model .eq. 'gausFs') then
      a = prm(1)
      b = prm(2)
      c = prm(3)
      msld = prm(4)
      bgd = prm(5)
      xl = prm(6)
      xu = prm(7)
```

```
      xn = prm(8)
      if (Q .le. 0.01) then
        xn =  0.05 * xn
      elseif (Q .le. 0.05) then
        xn =  0.1 * xn
      elseif (Q .le. 0.1) then
        xn = 0.5 * xn
      else
        xn = xn
      endif

      dx = (xu-xl)/xn
      n = int(xn)
      xxl=0
      xxu=dx
      sssum=0

      call qgaus(funcg,Q,a,b,c,alpha,xxl,xxu,ss)

      sssum=sssum+ss

      do 1215 i = 1,n
            xxl=xxl+dx
            xxu=xxu+dx
            call qgaus(funcg,Q,a,b,c,alpha,xxl,xxu,ss)
            sssum=sssum+ss
 1215   continue

      xsec = msld * sssum + bgd
c       print *, 'OK'
      return


cccccccccccccccccccccccccccccccccccccccccccccccccccccccccccccccccccccccc
c     Partial Structure of Microemulstion System
cccccccccccccccccccccccccccccccccccccccccccccccccccccccccccccccccccccccc
```

```
      elseif(xsec_model.eq.'parstrXww') then
c        cw=S/V at Water-Surfactant interface
         cw=prm(1)
c        dw= water penetration depth
         dw=prm(2)
         bgd=prm(3)
         eta2=prm(4)
c        Vw=water volume fraction
         Vw=prm(5)

         xsec = eta2/Vw/(1-Vw)*2.*pi*cw*exp(-dw**2.*Q**2.)/Q**4.+bgd

         return
      elseif(xsec_model.eq.'parstrXoo') then
         co=prm(1)
         do=prm(2)

         xsec = 1e-4*2.*pi*co*exp(-do**2.*Q**2.)/Q**4.

         return

      elseif(xsec_model.eq.'parstrXss') then
         cs=prm(1)
         ds=prm(2)
         bgds=prm(3)
         dsld2=prm(4)
         ps=prm(5)

         xsec = dsld2*2.*pi*ps**2./cs*exp(-ds**2.*Q**2./2./pi)/Q**2. + bgds

         return
      elseif(xsec_model .eq. 'parstrIss') then
         t = prm(1)
         Z = prm(2)
         bgd = prm(3)
```

```
          eta2 = prm(4)
          ps = prm(5)
          px = atan(Q*t/(Z+1))
          xsecm= (1-(cos(px))**(Z-1)*cos(Z*px))
          xsec = 4.*pi/(1-ps)*eta2*Z/(Z+1)/t*xsecm/Q**4+bgd

          return

ccccccccccccccccccccccccccccccccccccccccccccccccccccccccccccccccc
c     Teubner & Strey Model
ccccccccccccccccccccccccccccccccccccccccccccccccccccccccccccccccc
c

      elseif(xsec_model.eq.'teubnerstrey') then
        d = 2 * pi / prm(1)
        thy = 1/prm(2)
        dsld = prm(3)
        bgd = prm(4)

        AA = (1./thy**2.+(2.*pi/d)**2.)**2.
        BB = 2.*(1./thy**2.-(2.*pi/d)**2.)

        xsec = 8.*pi*dsld/(AA+BB*Q**2.+Q**4.)/thy+bgd

        return
      endif

      print *,'Wrong Xsec Type!'
      xsec = 1.d30
      return
      end


ccccccccccccccccccccccccccccccccccccccccccccccccccccccccccccccccc
      subroutine qgaus(funcg,Q,a,b,c,alpha,V1,xl,xu,ss)
ccccccccccccccccccccccccccccccccccccccccccccccccccccccccccccccccc
```

```
c
c Numerical Integration using Gaussian quadrature method
c

      real*8 Q,a,b,c,alpha,V1,xl,xu,ss
      real*8 x,w,xm, xr, ddx,s
      real*8 funcg
      external funcg
      dimension X(48),W(48)

       data X /0.0162767448496029D0, 0.0488129851360497D0,
     &0.0812974954644255D0,0.1136958501106659D0,0.145973714654896D0,
     &0.1780968823676186D0,0.2100313104605672D0,0.241743156163840D0,
     &0.2731988125910491D0,0.3043649443544963D0,0.3352085228926254D0,
     &0.3656968614723136D0,0.3957976498289086D0,0.4254789884073005D0,
     &0.4547094221677430D0,0.4843579739205963D0,0.5116941771546676D0,
     &0.5393881083243574D0,0.5665104185613971D0,0.5930323647775720D0,
     &0.6189258401254685D0,0.6441634037849671D0,0.6687183100439161D0,
     &0.6925645366421715D0,0.7156768123489676D0,0.7380306437444001D0,
     &0.7596023411766474D0,0.7803690438674332D0,0.8003087441391408D0,
     &0.8194003107379316D0,0.8376235112281871D0,0.8549590334346014D0,
     &0.8713885059092965D0,0.8868945174024204D0,0.9014606353158523D0,
     &0.9150714231208980D0,0.9277124567223086D0,0.9393703397527552D0,
     &0.9500327177844376D0,0.9596882914487425D0,0.9683268284632642D0,
     &0.9759391745851364D0,0.9825172635630146D0,0.9880541263296237D0,
     &0.9925439003237626D0,0.9959818429872092D0,0.9983643758631816D0,
     &0.9996895038832307D0/

      data W /0.0325506144923631D0,0.0325161187138688D0,
     &0.0324471637140642D0,0.0323438225685759D0,0.0322062047940302D0,
     &0.0320344562319926D0,0.0318287588944110D0,0.0315893307707271D0,
     &0.0313164255968613D0,0.0310103325863138D0,0.0306713761236691D0,
     &0.0302999154208275D0,0.0298963441363283D0,0.0294610899581679D0,
     &0.0289946141505552D0,0.0284974110650853D0,0.0279700076168483D0,
     &0.0274129627260292D0,0.0268268667255917D0,0.0262123407356724D0,
     &0.0255700360053493D0,0.0249006332224836D0,0.0242048417923646D0,
```

```
     &0.0234833990859262D0,0.0227370696583293D0,0.0219666444387443D0,
     &0.0211729398921912D0,0.0203567971543333D0,0.0195190811401450D0,
     &0.0186606796274114D0,0.0177825023160452D0,0.0168854798642451D0,
     &0.0159705629025622D0,0.0150387210269949D0,0.0140909417723148D0,
     &0.0131282295669615D0,0.0121516046710883D0,0.0111621020998384D0,
     &0.0101607705350084D0,0.0091486712307833D0,0.0081268769256987D0,
     &0.0070964707911538D0,0.0060585455042359D0,0.0050142027429275D0,
     &0.0039645543384446D0,0.0029107318179349D0,0.0018539607889469D0,
     &0.0007967920655520D0/


      xm = 0.5*(xu+xl)
      xr = 0.5*(xu-xl)
      ss = 0.0

      do 11 j = 1,48
        ddx = xr*x(j)
        s=funcg(Q,a,b,c,alpha,V1,xm+ddx)+funcg(Q,a,b,c,alpha,V1,xm-ddx)
        ss=ss+w(j)*s

 11   continue
      ss = xr*ss

      return
      end

cccccccccccccccccccccccccccccccccccccccccccccccccccccccccccccccccc
      subroutine qgaus0(ftnDint,alpha,yl,yu,sss)
cccccccccccccccccccccccccccccccccccccccccccccccccccccccccccccccccc
c
c Numerical integration using Gaussian quadrature method
c

      real*8 alpha,yl,yu,sss
      real*8 y,w,ym, yr, ddy,s
      real*8 ftnDint
```

```
external ftnDint
dimension y(48),W(48)

 data y /0.0162767448496029D0, 0.0488129851360497D0,
&0.0812974954644255D0,0.1136958501106659D0,0.145973714654896D0,
&0.1780968823676186D0,0.2100313104605672D0,0.241743156163840D0,
&0.2731988125910491D0,0.3043649443544963D0,0.3352085228926254D0,
&0.3656968614723136D0,0.3957976498289086D0,0.4254789884073005D0,
&0.4547094221677430D0,0.4843579739205963D0,0.5116941771546676D0,
&0.5393881083243574D0,0.5665104185613971D0,0.5930323647775720D0,
&0.6189258401254685D0,0.6441634037849671D0,0.6687183100439161D0,
&0.6925645366421715D0,0.7156768123489676D0,0.7380306437444001D0,
&0.7596023411766474D0,0.7803690438674332D0,0.8003087441391408D0,
&0.8194003107379316D0,0.8376235112281871D0,0.8549590334346014D0,
&0.8713885059092965D0,0.8868945174024204D0,0.9014606353158523D0,
&0.9150714231208980D0,0.9277124567223086D0,0.9393703397527552D0,
&0.9500327177844376D0,0.9596882914487425D0,0.9683268284632642D0,
&0.9759391745851364D0,0.9825172635630146D0,0.9880541263296237D0,
&0.9925439003237626D0,0.9959818429872092D0,0.9983643758631816D0,
&0.9996895038832307D0/

 data W /0.0325506144923631D0,0.0325161187138688D0,
&0.0324471637140642D0,0.0323438225685759D0,0.0322062047940302D0,
&0.0320344562319926D0,0.0318287588944110D0,0.0315893307707271D0,
&0.0313164255968613D0,0.0310103325863138D0,0.0306713761236691D0,
&0.0302999154208275D0,0.0298963441363283D0,0.0294610899581679D0,
&0.0289946141505552D0,0.0284974110650853D0,0.0279700076168483D0,
&0.0274129627260292D0,0.0268268667255917D0,0.0262123407356724D0,
&0.0255700360053493D0,0.0249006332224836D0,0.0242048417923646D0,
&0.0234833990859262D0,0.0227370696583293D0,0.0219666444387443D0,
&0.0211729398921912D0,0.0203567971543333D0,0.0195190811401450D0,
&0.0186606796274114D0,0.0177825023160452D0,0.0168854798642451D0,
&0.0159705629025622D0,0.0150387210269949D0,0.0140909417723148D0,
&0.0131282295669615D0,0.0121516046710883D0,0.0111621020998384D0,
&0.0101607705350084D0,0.0091486712307833D0,0.0081268769256987D0,
&0.0070964707911538D0,0.0060585455042359D0,0.0050142027429275D0,
```

```
     &0.0039645543384446D0,0.0029107318179349D0,0.0018539607889469D0,
     &0.0007967920655520D0/


      ym = 0.5*(yu+yl)
      yr = 0.5*(yu-yl)
      sss = 0.0

      do 17 j = 1,48
        ddy = yr*y(j)
        s=ftnDint(alpha,ym+ddy)+ftnDint(alpha,ym-ddy)
        sss=sss+w(j)*s

 17     continue
      sss = yr*sss

      return
      end

cccccccccccccccccccccccccccccccccccccccccccccccccccccccccccccccccccccccc
      real*8 function funcg(Q,a,b,c,alpha,V1,r)
cccccccccccccccccccccccccccccccccccccccccccccccccccccccccccccccccccccccc
c
c
c I(Q) = <n^2> Int(0,oo) F(r) sin(Qr)/Qr 4 Pi r^2 dr + background
c
c where <n^2>
c       F(r)  : Debye correlation function
c       g(r)  : two-point correlation function
c       g(0) = 1 : asymptotic
c       g(oo)= 0
c
c       xl = lower limit of integration = 0
c       xu = upper limit of integration = oo,
c            in practice xu is determined by the shape of the integrand
c
```

```
      implicit none
      real*8 Q,a,b,c,alpha,V1,r
      real*8 g1,g2,g3,g4,g5,g6,g7,g,F
      real*8 pi
      real*8 yl,yu,sss
      real*8 ftnGauss,ftnDint,erf
      external ftnGauss,ftnDint,erf

      pi = 3.141592653

cccccccccccccccccccccccccccccccccccccccccccccccccccccccccccccccccc
c     g(r) by Choi & Chen, from f(k) ~ 1/k^8
cccccccccccccccccccccccccccccccccccccccccccccccccccccccccccccccccc
      g1=4*b*c*(a**2+(b+c)**2)**2/(b+c)/r
      g2=(a**2-b**2+c**2)/(4*a**2*b**2+(a**2-b**2+c**2)**2)**2
      g3=r/(4*c*((a**2+b**2)**2+2*(a**2-b**2)*c**2+c**4))
      g4=(-8*a**2*b**2+(a**2+b**2)**2+2*(a**2-b**2)*c**2+c**4)*sin(a*r)
      g5=4*(4*a**2*b**2+(a**2-b**2+c**2)**2)**2
      g6=-a*b*(a**2-b**2+c**2)*cos(a*r)
      g7=(4*a**2*b**2+(a**2-b**2+c**2)**2)**2

      g=g1*(exp(-c*r)*(g2+g3)+exp(-b*r)/a/b*(g4/g5+g6/g7))
cccccccccccccccccccccccccccccccccccccccccccccccccccccccccccccccccc




cccccccccccccccccccccccccccccccccccccccccccccccccccccccccccccccccc
c     Debye Correlation Functions
cccccccccccccccccccccccccccccccccccccccccccccccccccccccccccccccccc



cccccccccccccccccccccccccccccccccccccccccccccccccccccccccccccccccc
c     Film contrast
cccccccccccccccccccccccccccccccccccccccccccccccccccccccccccccccccc
c      F1 = 1./sqrt(1-(1-Vs**2.)**2.*g**2.)
```

```
c     F2 = 1./sqrt(1-(1-Vs**2.)**2.)
c     F = (F1-1.)/(F2-1.)
c


cccccccccccccccccccccccccccccccccccccccccccccccccccccccccccccccccc
c    Bulk Contrast:Alpha =/ 0 , Small Alpha Expansion
cccccccccccccccccccccccccccccccccccccccccccccccccccccccccccccccccc
c     V1=1./2.-(alpha-(alpha**3.)/6)/sqrt(2.*pi)
c     V1=1./2.-(alpha)/sqrt(2.*pi)
c     F1=1./(2.*pi*V1*(1.-V1))
c     F2=acos(g)
c     F3=alpha**2.*tan(acos(g)/2.)
c     F4=alpha**4./4.*(tan(acos(g)/2.)+1./3.*(tan(acos(g)/2.))**3.)
c     F=1-F1*(F2-F3+F4)
c
c     F=1-F1*(F2-F3)

cccccccccccccccccccccccccccccccccccccccccccccccccccccccccccccccccccc
c    Bulk Contrast: General, No approximation
cccccccccccccccccccccccccccccccccccccccccccccccccccccccccccccccccccc
c
c   NOTE : alpha could be negative value
c


      yl=0.0
      yu=acos(g)
      call qgaus0(ftnDint,alpha,yl,yu,sss)

      F=1-1/(2*pi*V1*(1-V1))*sss


c
c    bulk contrast:alpha=0
ccccccccccccccccccccccccccccccccccccccccccccccccccccccccccccccccccccc
c     F = 2/pi*asin(g)
```

```
cccccccccccccccccccccccccccccccccccccccccccccccccccccccccccccccccccccc

      funcg = F*sin(Q*r)/(Q*r)*4*pi*r**2
      return
      end




cccccccccccccccccccccccccccccccccccccccccccccccccccccccccccccccccccccc
      real*8 function ftnGauss(alpha,x)
cccccccccccccccccccccccccccccccccccccccccccccccccccccccccccccccccccccc
c
c     Gaussian distribution exp(-x^2)
c
      implicit none
      real*8 alpha,x

      ftnGauss=exp(-x**2.)
      return
      end

cccccccccccccccccccccccccccccccccccccccccccccccccccccccccccccccccccccc
      real*8 function  ftnDint(alpha,x)
cccccccccccccccccccccccccccccccccccccccccccccccccccccccccccccccccccccc
c
c     Integrand for the integration for a Debye correlation function
c     in non-isometric microemulsions
c

      implicit none
      real*8 alpha,x

      ftnDint=exp(-alpha**2/(1+cos(x)))
      return
```

```
      end

cccccccccccccccccccccccccccccccccccccccccccccccccccccccccccccccccccccc
      real*8 function func(prm, Q, j, xsec_model, ii)
cccccccccccccccccccccccccccccccccccccccccccccccccccccccccccccccccccccc

      implicit none
      character*20 xsec_model
      integer j,resyn,nfold, ii
      real*8 prm(200), sum, reso, Q, xsec
      real*8 r1,r2,rl1,rl2,rlam,dlam,rdet, sig
      common/resof1/reso(3,200,200),r1,r2,rl1,rl2,rlam,dlam,rdet,resyn
      common/resof2/sig(3,200),nfold

 1    sum = xsec(Q, prm, xsec_model)
 2    func = sum
      return
      end



c
c     The Anneal Method to get the optimal fit of some functional data
c     to experimental data.
cccccccccccccccccccccccccccccccccccccccccccccccccccccccccccccccccccccc
      subroutine anneal(edat,ftemp,pnumber,step,oldchi,state,xsec_model)
cccccccccccccccccccccccccccccccccccccccccccccccccccccccccccccccccccccc
c
c
      implicit none
      external func, ran3
      character*20 state,xsec_model
      integer i, ii, accept, reject, estart(3), enumber, pnumber
      integer j, iloop, idum, imax, imequ, equ, iprint, sets
      integer etotal
      real*8 edat(3,4,200), prm, fdat(200),temp, step, oldchi, ran3
      real*8 chisqu, edge, func, chiave, outchi, IQ
```

```
      real*8 limit, sumchi, delchi, sumchi2, chidvi
      real*8 bound,thy,thyplum,dbound,p,ftemp
      real*8 ave, fave, outsum, avesum(200), favesum(200),chimin
      real*8 xsec
      common/general/estart, enumber(3), prm(200), bound(2,200), imax
      common/QQQ/ave(200), fave(200), imequ, iprint, sets

c
c assign initial values
cccccccccccccccccccccccc

      print *,state
      do 10 i=1, 200
        fdat(i) = 0.
        avesum(i) = 0.
        favesum(i) = 0.
        ave(i) = 0.d0
        fave(i) = 0.d0
 10   continue

      open(unit=20,file='FIRST.fit',status='unknown')
      rewind(unit=20)
c
c  First chisqu
c
      etotal = 0
      do 260 ii=1,sets
        etotal = etotal+enumber(ii)
 260  continue
      oldchi = 0.d0
      chimin = 1.d10
      do 250 ii=1,sets
        do 231 i=1, enumber(ii)
          fdat(i) = xsec(edat(ii,1,i), prm, xsec_model)
          write(20,1023) edat(ii,1,i), fdat(i)
          oldchi = oldchi+
```

```
  +               ((fdat(i)-edat(ii,2,i))/edat(ii,3,i))**2.
231     continue

250  continue
      close(unit=20)
      oldchi = oldchi/float(etotal)

      print *, 'First Chiqu = ', oldchi

              open(unit=8,file='SANS.fit',status='old')
                    rewind(unit=8)
                    write(8,*) iloop
                    write(8,1023) oldchi
                    write(8,1023) outsum
                    write(8,1023) sumchi
                    write(8,1023) sumchi2
                    write(8,*) accept
                    write(8,*) reject
                    write(8,1023) temp
                    write(8,1023) step
                    write(8,*) equ
                    write(8,*) iprint
                    write(8,*) pnumber
                    write(8,*) sets
                    write(8,1023) prm(pnumber+1)
                    write(8,*) ' '
                    do 219 i=1,pnumber
                       write(8,2023) prm(i),
  +                                 avesum(i),favesum(i)
219                 continue
2023                format(3e15.4)
                    write(8,*) ' '
                    do 289 ii=1,sets
                       do 229 i=1,enumber(ii)
                          IQ = xsec(edat(ii,1,i), prm, xsec_model)
                          write(8,1023) edat(ii,1,i),IQ
```

```
229                 continue
289                 continue
              close(unit=8)

              print *,'done'



      limit = 1.e-6
      iloop = 0
      edge = 0.
      accept = 0
      reject = 0
      idum = -100
      chiave = 1.e30
      outchi = 1.e30
      sumchi = 0.
      sumchi2 = 0.
      equ = 0
      outsum = 0.
      if(state.eq.'continue') then
        open(unit=8,file='SANS.fit',status='unknown')
        rewind(unit=8)
        read(8,*) iloop
        read(8,*) oldchi
        read(8,*) outsum
        read(8,*) sumchi
        read(8,*) sumchi2
        read(8,*) accept
        read(8,*) reject
        read(8,*) temp
        read(8,*) step
        read(8,*) equ
        read(8,*) iprint
        read(8,*) pnumber
        read(8,*) sets
        read(8,*) prm(pnumber+1)
```

```
         do 12 i=1, pnumber
           read(8,*) prm(i), avesum(i),
     +               favesum(i)
 12      continue
         close(unit=8)
       endif
       open(unit=7, file='intave.fit',status='unknown')
       rewind(unit=7)
       open(unit=9, file='intprm.fit',status='unknown')
       rewind(unit=9)

cccccc
c
c outer loop of all parameters
c
 1000 iloop = iloop+1
       temp = oldchi*ftemp
       print * , iloop
c
c inner loop of individual parameter
c
       do 100 j=1, pnumber


c
c update prm(j)
c
           p = prm(j)
           dbound = bound(2,j)-bound(1,j)
           if(dbound.eq.0.) go to 100
           thy = ran3(idum)
           thyplum = 2.*thy-1.
           prm(j) = prm(j)+thyplum*step*prm(j)
             if(prm(j).lt.bound(1,j)) then
               prm(j) = prm(j)+
     *           dbound*float(int((bound(1,j)-prm(j))/dbound)+1)
             endif
```

```
          if(prm(j).gt.bound(2,j)) then
            prm(j) = prm(j)-
     *        dbound*float(int((prm(j)-bound(2,j))/dbound)+1)
          endif
c
cccccccccccccccccccccccccccccccccccccccccccccccccccccccccccccccc
c Calculate Chi-Square of the Current Parameter Set
cccccccccccccccccccccccccccccccccccccccccccccccccccccccccccccccc
      chisqu = 0.
      do 270 ii=1,sets
        do 20 i=1, enumber(ii)
          fdat(i) = func(prm, edat(ii,1,i), i, xsec_model, ii)
          chisqu = chisqu+
     +            ((fdat(i)-edat(ii,2,i))/edat(ii,3,i))**2.
 20       continue
 270  continue
      chisqu = chisqu/float(etotal)
      print *, 'chisqu = ', chisqu
      print *, ' '
      print *, '      a = ', prm(1)
      print *, '      b = ', prm(2)
      print *, '      c = ', prm(3)
      print *, '  alpha = ', prm(4)
      print *, '     V1 = ', prm(5)
      print *, '  sigma = ', prm(6)
      print *, '   eta2 = ', prm(7)
      print *, '    bgd = ', prm(8)
      print *, ' '

      edge = ran3(idum)
      delchi = chisqu-oldchi
c
c
      if(delchi.le.0.) then
        accept = accept+1
        oldchi = chisqu
```

```
      else
        if(exp(-delchi/temp).gt.edge) then
          accept = accept+1
          oldchi = chisqu
        else
          reject = reject+1
          prm(j) = p
        endif
      endif
        avesum(j) = avesum(j)+prm(j)
        favesum(j) = favesum(j)+prm(j)
        outsum = outsum+oldchi
        sumchi = sumchi+oldchi
        sumchi2 = sumchi2+oldchi**2.
 100  continue
cccccc

        if(((float(iloop)/float(iprint))
     +        -int(float(iloop)/float(iprint))).eq.0.) then
          print *, 'OK'
          if(oldchi.le.chimin) then
            print*,'OK'
            chimin = oldchi
            do 200 i=1,pnumber
              ave(i) = avesum(i)/float(iprint)
              fave(i) = favesum(i)/float(iloop)
 200         continue
              outchi = outsum/float(iloop*pnumber)
              chiave = sumchi/float(iprint*pnumber)
              chidvi = sumchi2/float(iprint*pnumber)-chiave**2.

 2000          open(unit=8,file='SANS.fit',status='old')
              rewind(unit=8)
              write(8,*) iloop
              write(8,1023) oldchi
              write(8,1023) outsum
```

```
            write(8,1023) sumchi
            write(8,1023) sumchi2
            write(8,*) accept
            write(8,*) reject
            write(8,1023) temp
            write(8,1023) step
            write(8,*) equ
            write(8,*) iprint
            write(8,*) pnumber
            write(8,*) sets
            write(8,1023) prm(pnumber+1)
            write(8,*) ' '
            do 21 i=1,pnumber
              write(8,1023) prm(i),
     +                      avesum(i),favesum(i)
21            continue
1023           format(3e15.4)
            write(8,*) ' '
            do 280 ii=1,sets
              do 22 i=1,enumber(ii)
                IQ = func(prm, edat(ii,1,i), i, xsec_model, ii)
                write(8,1023) edat(ii,1,i),IQ
22              continue
280           continue
            close(unit=8)
          endif
          sumchi = 0.d0
          sumchi2 = 0.d0
          do 30 i=1,pnumber
            avesum(i) = 0.d0
30         continue
          write(7,1024) iloop, chiave,chidvi,outchi
          write(9,1025) (prm(i),i=1,7)
1024        format(I11,3e11.3)
1025        format(7e11.3)
      endif
```

```
cccccccccccccccccccccccccccccccccccccccccccccccccccccccccccccccccccccccc
c Check Convergence
cccccccccccccccccccccccccccccccccccccccccccccccccccccccccccccccccccccccc
      if(equ.ge.1) then
        if(iloop.ge.(10.*iprint).and.
     +         abs(outchi-chiave)/outchi.le.limit) then
          print *,'Out by Deviation'
          go to 9999
        endif
        if(oldchi.le.0.5) then
          print *,'Out by Chi Square'
          go to 9999
        endif
        if(iloop.eq.imax) then
          print *,'Out by Steps'
          go to 9999
        endif
      else
        if(iloop.eq.imequ) then
          iloop = 0
          equ = 1
          accept = 0
          reject = 0
          sumchi = 0.d0
          sumchi2 = 0.d0
          outsum = 0.d0
          do 25 i=1,pnumber
            avesum(i) = 0.d0
            favesum(i) = 0.d0
 25       continue
          close(unit=7)
          close(unit=9)
          open(unit=7,file='intave.fit',status='unknown')
          rewind(unit=7)
          open(unit=9, file='intprm.fit',status='unknown')
          rewind(unit=9)
```

```
           endif
        endif
cccccc
      go to 1000
cccccc
c
 9999 close(unit=7)
      close(unit=9)
      return
      end

ccccccccccccccccccccccccccccccccccccccccccccccccccccccccccccccc
      function ran3(idum)
ccccccccccccccccccccccccccccccccccccccccccccccccccccccccccccccc
c
c     Generate random numbers
c
      integer idum
      integer mbig,mseed,mz
      real*8 ran3
      real  fac
      parameter (mbig=1000000000,mseed=161803398,mz=0,fac=1./mbig)
      integer i,iff,ii,inext,inextp,k
      integer mj,mk,ma(55)
      save iff,inext,inextp,ma
      data iff /0/
      if(idum.lt.0.or.iff.eq.0)then
        iff=1
        mj=mseed-iabs(idum)
        mj=mod(mj,mbig)
        ma(55)=mj
        mk=1
        do 11 i=1,54
          ii=mod(21*i,55)
          ma(ii)=mk
          mk=mj-mk
```

```
          if(mk.lt.MZ)mk=mk+mbig
          mj=ma(ii)
11        continue
        do 13 k=1,4
          do 12 i=1,55
            ma(i)=ma(i)-ma(1+mod(i+30,55))
            if(ma(i).lt.MZ)ma(i)=ma(i)+mbig
12          continue
13        continue
        inext=0
        inextp=31
        idum=1
      endif
      inext=inext+1
      if(inext.eq.56)inext=1
      inextp=inextp+1
      if(inextp.eq.56)inextp=1
      mj=ma(inext)-ma(inextp)
      if(mj.lt.MZ)mj=mj+mbig
      ma(inext)=mj
      ran3=mj*fac
      return
      end
```